Fall 2021

Reduced calibration uncertainties for the global network of gravitational-wave observatories and the impact on sky localization of burst-like sources

Dripta Bhattacharjee

Department: Physics

REDUCED CALIBRATION UNCERTAINTIES FOR THE GLOBAL NETWORK OF GRAVITATIONAL-WAVE OBSERVATORIES AND THE IMPACT ON SKY LOCALIZATION OF BURST-LIKE SOURCES.

by

DRIPTA BHATTACHARJEE

A DISSERTATION

Presented to the Graduate Faculty of the

MISSOURI UNIVERSITY OF SCIENCE AND TECHNOLOGY

In Partial Fulfillment of the Requirements for the Degree

DOCTOR OF PHILOSOPHY

in

PHYSICS

2021

Approved by:

Marco Cavaglia, Advisor
Daniel Fischer
Julia Medvedeva
Shun Saito
Richard Savage

ABSTRACT

The Advanced Laser Interferometer Gravitational-wave Observatory (LIGO) is a science facility in the United States devoted to the observation of gravitational waves (GWs). It comprises two kilometer-scale laser interferometers. It is a part of a global ground-based GW detector network that also includes Virgo in Italy and KAGRA in Japan. Calibration of the LIGO detectors is achieved using displacement fiducials generated by radiation pressure based systems called Photon Calibrators (Pcals). The first part of this research described here details the developments implemented during the third LIGO-Virgo-KAGRA (LVK) observation run, O3, in the propagation of laser power calibration via transfer standards to on-line power sensors. These developments have enabled generation of length fiducials with improved accuracy of 0.41 %. This estimated uncertainty is almost a factor of two smaller than the lowest values previously reported. This result enabled reducing the uncertainty in overall calibration of the LIGO interferometers during the O3 observing run to the 2 % level.

GW source parameter estimation and localization rely on accurately calibrated strain data. The second part of the research reported here investigates the impact of overall, systematic detector calibration errors on the sky localization of burst-like GW sources, specifically core collapse supernovae (CCSN). This analysis is performed using simulated waveforms from different CCSN models and one of the standard LVK pipelines used to search for burst-like GW signals. Overall calibration errors as large as ± 10 % are imposed on a single detector in the LIGO-Virgo network. Preliminary results indicate that this causes average changes in the area of 90 % sky localization confidence regions as large as 18 %. Associated average errors in estimated probabilities for these regions are as large as 5 %. Furthermore, for sources located in some regions of the sky, source localization errors are as large as 90 %, indicating that counterparts to GW signals would not be found within the 90 % confidence regions in follow-up observations by electromagnetic observatories.

ACKNOWLEDGMENTS

I arrived at United States in 2016 with a dream to get a Doctorate degree in Physics. In the past five years, I was fortunate to come across people who directly or indirectly helped me in my journey. I would like to thank my Ph.D advisor Dr. Marco Cavaglia. I am very grateful to him for his constant support. He was honest with me when he needed to be and was extremely kind to me when I needed him to be.

I would also like to thank Dr. Richard Savage for not only guiding me on my research project while I was in Hanford, but also for ensuring my mental and emotional well being, specially during the height of the pandemic. I am also very grateful to his wife, Kiyomi for her kindness, my stay at Hanford was very comfortable and welcoming despite the pandemic because of her.

I would also like to thank Dr. Gregory Mendell. We had many a long and useful discussions that deepened my understanding about the subject.

I am extremely grateful to the LIGO Fellows program that provided the opportunity for me to work on site at LIGO, Hanford. I would also like to thank Dr. Michael Landry for supporting me as a LIGO fellow for almost two years, specially during the pandemic.

I am thankful to my friends and colleagues Yanyan Zheng and Kentaro Mogushi for helping me develop my understanding on the various aspects of the subject as well as for their support.

A huge part of my support system is my friend Meghna Bhattacharya. She made my graduate student life a lot more fun and provided constant support and encouragement.

My biggest strength are my parents. Without their support, I would never have the courage to pursue a Ph. D. program in a foreign land. I am very grateful that they tolerated my ranting and venting online for the past five years.

Finally, I would like to thank the U.S. National Science Foundation (NSF). The work in this dissertation is supported by NSF grants PHY-1921006 and PHY-2011334.

TABLE OF CONTENTS

Page

LIST OF ILLUSTRATIONS

LIST OF TABLES

LIST OF ABBREVIATIONS

ADC Analog-to-digital converter. 53

AOM Acousto-optic modulator. 65

BBH Binary black hole. 7

BNS Binary neutron star. 8

BS Beamsplitter. 32

CBC Compact binary coalescence. 23

CCSN Core collapse supernova. 27

CE Calibration error. 110

COM Center-of-mass frame. 23

CW Continuous gravitational waves. 25

cWB coherent WaveBurst. 28

DAQ Data aquisition system. 53

DARM Differential arm. 7

DoE Degree of equivalence. 96

EM Electromagnetic. 2

ETM End test mass. 32

FFT Fast Fourier transform. 78

FSM Free swinging Michelson. 59

Gpc Gigaparsec. 24

GR General theory of relativity. 1, 10, 11, 13

GRB Gamma ray bursts. 27

GS Gold standard. 70

GWs Gravitational waves. 1

IMC Input mode cleaner. 32

ITM Input test mass. 33

LH Livingston-Hanford detector network. ix, 45

LHO LIGO Hanford site. 58

LHV Livingston-Hanford-Virgo detectors. ix, 45

LIGO Laser Interferometer Gravitational-wave Observatory. 2

LVK LIGO-Virgo-KAGRA network of GW detectors. 22

MAP Maximum a posteriori. 54

MCMC Markov Chain Monte Carlo fitting algorithm. 54

MMA multi-messenger astronomy. 25

Ncal Newtonian calibrator. 61

NIST National Institute of Standards and Technology. 70

NMI National metrology institute. 95

NSBH Neutron star-Black hole pair. 8

OFS Optical follower servo. 67

OMC Output mode cleaner. 32

Pcal Photon calibrator. 60

PRM Power recycling mirror. 34

PSD Power spectral density. 27

PTB Physikalisch-Technische Bundesanstalt. 95

PUM Penultimate mass. 36

sGRB Short gamma ray burst. 99

SGWB Stochastic gravitational waves background. 26

SN Supernova. 1

SNR Signal-to-noise ratio. 9

SPD Searched probability deficit. 112

SR Special theory of relativity. 2, 10

SRM Signal recycling mirror. 34

TDCF Time-dependent correction factors. 54

TEM Transverse electromagnetic mode. 32

TF Time-Frequency. 28

TST Test mass stage. 36

TT Transverse-traceless. 16

UIM Upper intermediate mass. 36

WS Working standard. 70

WSH Working standard for Hanford. 82

WSS Spare working standard. 95

1. INTRODUCTION

Gravitational waves (GWs) are 'ripples' in space-time caused by some of the most cataclysmic events in the Universe such as colliding black holes and neutron stars, supernovae (SN), rotating neutron stars that do not have axisymmetry (Riles (2013)). Any system that has a non zero quadrupole mass moment is a source of GWs (Einstein (1918)). Albert Einstein predicted the existence of GWs in 1916 as a consequence of his general theory of relativity (GR) (Einstein (1915)). Einstein showed that massive accelerating objects (such as neutron stars or black holes orbiting each other) disrupt the space-time in such a way that GWs propagate in all directions away from the source at the speed of light, carrying information about their origins as well as the nature of gravity itself (Einstein (1918)).

Although the processes that generate GWs can be extremely violent and destructive, by the time the waves reach Earth the wave amplitudes are typically about $10,000$ times smaller than the nucleus of an atom. Since GWs are so faint and their interaction with matter so weak, Einstein himself suspected that they could ever be detected (Einstein (1914-1918)).

The first observational proof of existence of these GWs came in 1974, when two astronomers, Russell Hulse and Joseph Taylor, using the Arecibo Radio Observatory in Puerto Rico, discovered a binary pulsar $21,000$ light years from Earth, the type of system that GR predicted should radiate GWs (Hulse and Taylor (1975)). To test Einstein's prediction, Hulse and Taylor started measuring how the stars's orbits changed over time. After years of observations, they determined that the stars were getting closer to each other at precisely the rate predicted by GR if they were emitting GWs (Taylor *et al.* (1979)). Since then, many astronomers have studied pulsar radio-emissions and found similar effects, further confirming the existence of these waves (Abbott *et al.* (2008); Backer *et al.* (1982); Jones (2010)). However, all these observations were indirect detections of GWs.

That changed when about 100 years after Einstein proposed his theory, on 14 September 2015, GWs were directly observed for the first time by the twin Laser Interferometer Gravitational wave Observatory (LIGO) detectors (Abbott *et al.* (2016b)). The following section is a brief history of the search for GWs, including their conceptualization in the early twentieth century and thereafter the efforts towards detection.

1.1. DISCOVERING GWS

Sir Isaac Newton introduced his law of gravity in 1686 (Newton (1686)). His theory implied that the gravitational force is transmitted instantaneously.

In years to follow, scientists proposed the notion of a field, a continuously varying entity which propagates (Forbes (2014)). In 1865, James Clerk Maxwell, by treating electricity and magnetism as fields concluded that light itself was an electromagnetic (EM) wave (Maxwell (1865)). In his 'The dynamical theory of EM fields' he put forth the question if one can think of gravity as being propagated by a field (Maxwell (1865)).

Almost forty years after Maxwell published his work on electricity and magnetism, Einstein completed Maxwell's unification of electricity and magnetism by showing that the two fields were really one with his publication of the special theory of relativity (SR) in 1905 (Einstein (1905)). He based his theory of SR on two postulates: the laws of physics are invariant in any inertial frame of reference and the speed of light is the same for all inertial observers. As a consequence of SR no information can travel faster than the speed of light in vacuum, and that demanded a thorough modification of Newtonian physics.

During the same months that Einstein was working on special relativity, Henri Poincaré was independently writing up his own research along similar lines, where he assumed that the gravitational force propagates at the speed of light (Poincare (1905)). If that is the case, there should be a time lag between any change in gravity and its effect. These changes, Poincaré explicitly stated, are propagated by GWs.

Finally in 1915, Einstein postulated in the theory of GR that gravity is a manifestation of the curvature of space–time. Einstein's equations relate the Einstein tensor which express the curvature of local space–time to the local stress energy and momentum tensor. The GWs are a consequence of his theory of GR. Although Einstein initially suspected that these waves are mathematical constructs and not physical, he was later convinced about their existence (Einstein (1914-1918)).

Later, in 1956 Felix A. E. Pirani published a work that became a classic article in the further development of the GR (Pirani (1956)). He showed that a set of freely-falling particles would experience motions with respect to one another in the presence of GWs, see Figure 1.1. This proved that GWs were real and not could not be made vanishing with a gauge transformation. However Pirani's work remained mostly unknown in the mid-50s, since scientists were focused on finding the answer to the question whether GWs carry energy or not. In classical mechanics, energy is conserved if the system is invariant under time. However, in GR, energy is not conserved globally. But any curved space-time can be considered locally flat, and hence energy is conserved locally. The question whether GWs carry energy or not, was answered because of Pirani's aforementioned work and to the 'sticky bead argument' that Richard Feynmann proposed in 1957 Chapel Hill meeting (De-Witt and Rickles (2011)).

Among the audience in the Chapel Hill meeting was Joseph Weber. Fascinated by the discussions on GWs, he decided to build a device to detect them (Weber (1960)). In 1960 he published a paper in which he proposed to measure vibrations induced in a mechanical system to detect GWs (Weber (1960)). Weber designed and built a large metal cylinder 'antenna' to observe resonant vibrations induced by a transit of a GW pulse, analogous to someone hitting a bell with a hammer to hear its ring. Weber built two detectors, the first one was located at the University of Maryland and the other was situated 950 km away, in Argonne National Laboratory (Weber (1966)). If a detected signal was not recorded simultaneously in both laboratories, it was discarded as spurious signal produced

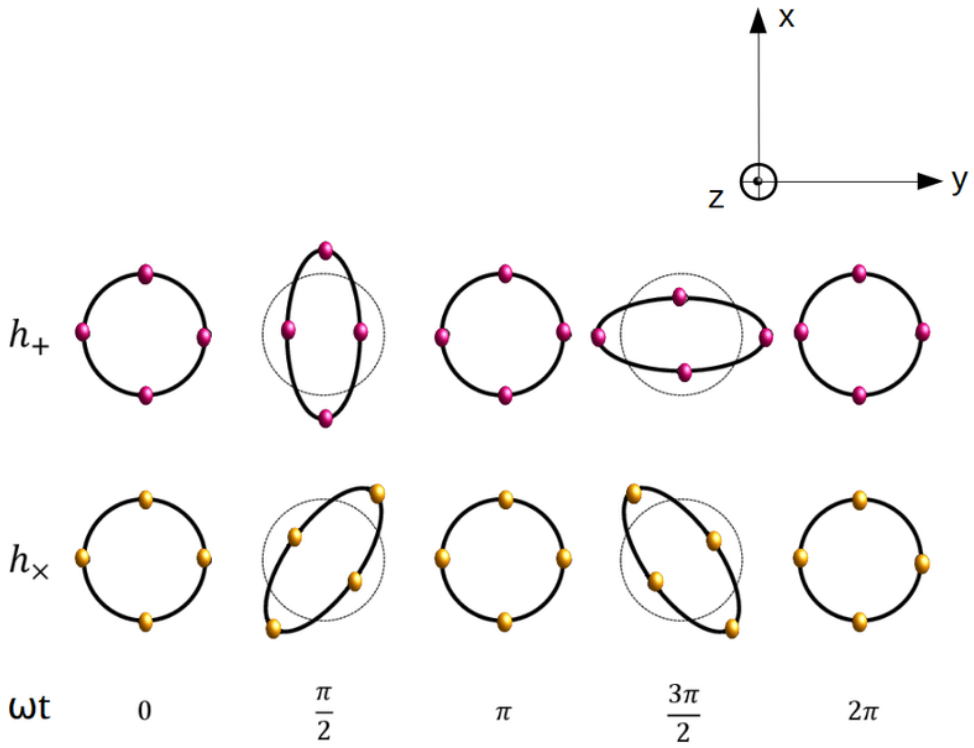

)

Figure 1.1. Illustration of the effect of a GW propagating along Z-axis on a ring of freely falling particles arranged in a circle. GWs have two polarizations, plus and cross. As a GW with plus polarization passes through the particles (top), spacetime is stretched in X-axis and compressed in Y-axis and vice versa. For a GW with cross polarization (bottom), a similar effect is observed but rotated by 45 degrees. credit:

by local disturbances. In 1969 Weber published a paper announcing the detection of GWs (Weber (1969)). Although Weber's claims of GW were eventually dismissed, he is generally credited to be the founder of experimental GW physics.

Weber outlined several methods on how to detect GWs. Among other various projects, he conceived the use of interferometric detectors. However, he did not pursue this concept and his work is only documented in the pages of his laboratory notebook (Stephen Hawking (1987)). In the 1970s, Rainer Weiss independently conceived the idea of building a laser interferometer. Weiss built a 1.5-m prototype at MIT, while at Caltech

Ronald Drever was building a 40 m prototype of an interferometric GW detectors. In 1979, Weiss offered to conduct a study in collaboration with industry partners to determine the feasibility and cost of an interferometer whose arms would measure in kilometers. The results of his study funded by National Science Foundation (NSF) was documented in a paper "A study of a long Baseline Gravitational Wave Antenna System," co-authored by Peter Saulson and Paul Linsay (Russell (1992)). This fundamental document is popularly called "The Blue Book" and covers many important issues in the construction and operation of such a large interferometer. NSF provided a grant jointly to the MIT and Caltech groups and named the project "Laser Interferometer Gravitational-Wave Observatory".

1.2. LIGO

GWs, as mentioned earlier, are very faint by the time they reach Earth and their effect on matter is almost negligible. A dimensionless strain factor, h, is defined to evaluate the effect of a GW on matter. The factor h describes the relative displacement per unit length produced by the waves between two objects. The strain induced by the astrophysical GWs are typically 10^{-21}. This value of h depends on how the wave was produced and how far its source is from an observer.

At their cores, design of a LIGO detector is that of a Michelson interferometer (Michelson and Morley (1887)). Their basic design is L-shaped and consists of a beam splitter, two end mirrors, and a photodetector that records the interference pattern as shown in Figure 1.2 (A). The LIGO interferometers differ from simple Michelson interferometers in their size and added complexities (Abbott *et al.* (2009a)). The scale of the LIGO instruments is crucial to their search for GWs. The longer the arms of an interferometer, the smaller the strain measurements they can make. LIGO has to be sensitive to changes in distance less than $1/10,000$ times a proton. Observing such small changes in distance requires the interferometer arms to be hundreds of kilometers long. Construction of such long arms poses a lot of practical challenges. So the Michelson design is altered to include

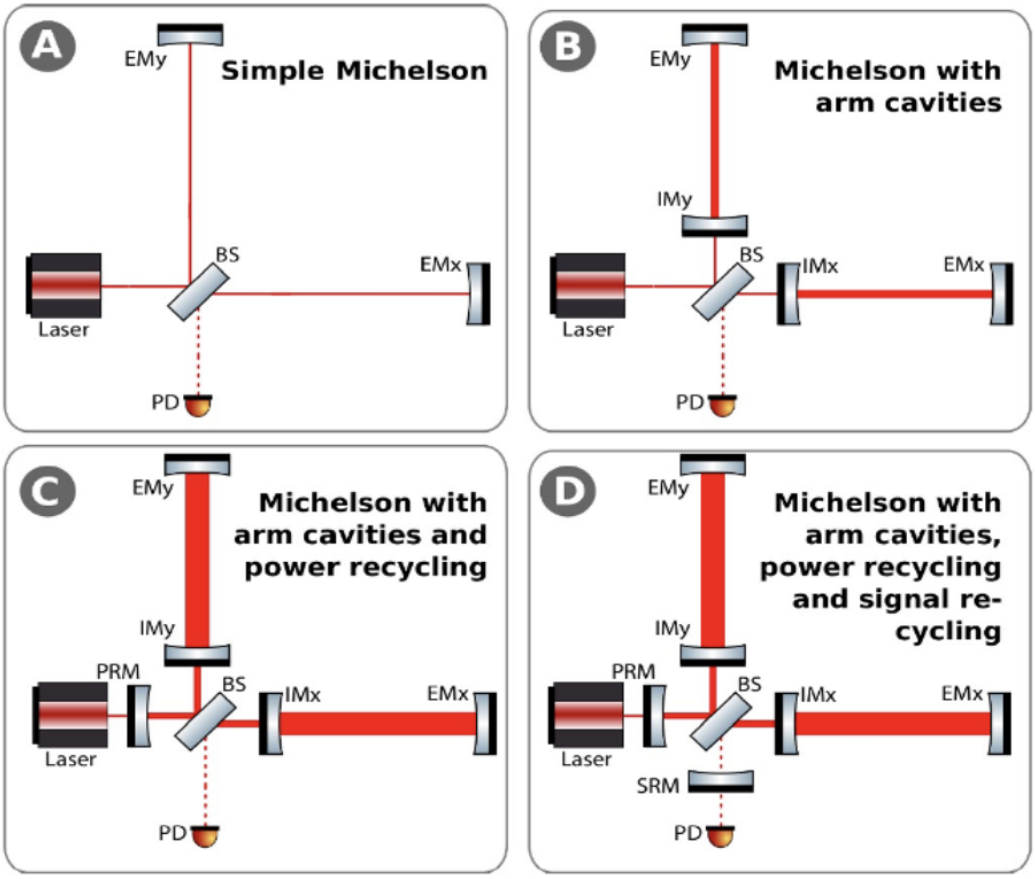

)

Figure 1.2. Schematic diagram showing the components of Dual Recycle Fabry Perot Michelson interferometer. credit: LIGO

Fabry-Perot cavities, which increase the effective arm lengths by $\sim$ 300 times (Michelson and Morley (1887)). Additional mirrors are placed in each arm near the beam splitter, 4km from the mirror at the end of that arm, see Figure 1.2) (B). The Fabry-Perot cavities also help increase the laser power build up, which in turn increases the interferometer's resolving power. LIGO's laser first enters the interferometer at about 40 Watts, but it needs to operate closer to 750kW in order to make any detection (Abbott *et al.* (2014)). To achieve such high powers, LIGO uses power recycling mirrors shown in Figure 1.2 (C). As the laser power is constantly entering the interferometer, the power recycling mirror continually 'recycles' the laser light that has traveled through the instrument back into the interferometer. This

process greatly boosts the power of the laser beam inside the Fabry Perot cavities without the need to generate such a powerful laser beam at the onset. LIGO interferometers also have signal recycling mirrors which enhance the signal that is received by the photodetector, as shown in Figure 1.2) (D), in a way similar to what power recycling mirror does to the laser power. The digital counts of the photodetector at the output of the interferometer is converted to the measured differential arm (DARM) length variation of the interferometer. The strain h is the DARM length divided by the average arm length of the interferometer and it depends upon the geometry of the measurement device, the arrival direction, and the frequency and polarization of the GW.

With these modifications, LIGO's interferometer is known as a Dual Recycled, Fabry-Perot Michelson. The LIGO detectors are discussed in much more detail in Section 4.

1.3. DETECTIONS BY LIGO

Since the discovery of GWs from a binary black hole (BBH) coalescence in 2015 (Abbott *et al.* (2016b)), ground-based GW detectors have opened a new window on our Universe. Today there is a network of ground based GW detectors that consists of the twin LIGO detectors in Livingston, Louisiana and Hanford, Washington in the US, VIRGO in Cascina, Italy (Acernese *et al.* (2015)) and KAGRA located underground in Kamioka mine, Japan (Akutsu *et al.* (2019)). Another LIGO detector in India is slated to come online by 2025 (Iyer *et al.* (2011)). The global network of currently operational or planned GW detectors is shown in Figure 1.3.

Such a world-wide network of widely-separated facilities enables extraction of more accurate astrophysical information from GWs. Specifically, adding more detectors to the network improves the ability to locate sources and test alternative theories of gravity (Abbott *et al.* (2019f)). BBH observations have also provided means to establish the rate and determine the population properties of BBH coalescences (Abbott *et al.* (2019c)). In

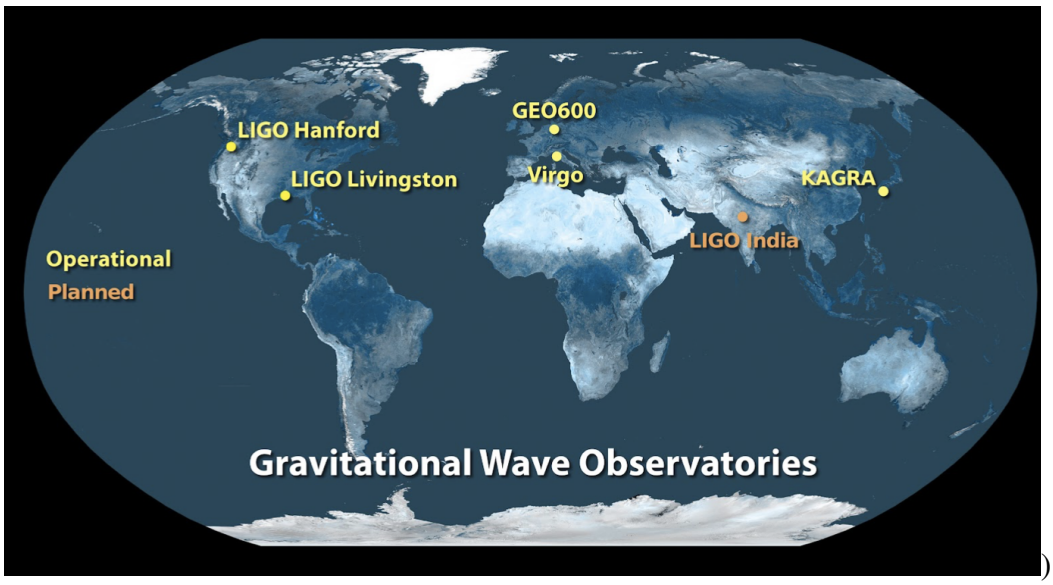

Figure 1.3. The global network of ground based interferometric GW detectors that currently operational and planned. Credit: https://www.ligo.caltech.edu

addition to BBHs, the first GW signal from a binary neutron star (BNS) coalescence, GW170817 was observed. This was also the first joint detection of GWs and EM emission (Abbott *et al.* (2017c)).

Depending on the process that generates the waves, there are 4 types of GW signals; compact binary inspiral, continuous, stochastic, and burst. The GW signals that the ground-based GW observatories have observed so far are GWs from compact binary coalescence. They are produced by orbiting pairs of massive dense objects, such as BBH, BNS or a neutron star - black hole pair (NSBH). To date, LIGO has published confident detection of GWs generated by about 90 pairs of merging black holes and neutron stars (Abbott *et al.* (2021a)). We will discuss the various sources and types of GWs in detail in Section 3.

The Sections in this dissertation are arranged in the following order: Section 2 describe how GWs mathematically follow from Einstein's GR. Section 3 elaborates the various sources of GWs in detail. Section 4 explains the design and working of LIGO detectors. It also provides a brief description of the various sources of noise that limit the

detector's sensitivity to the GW signals. The sensitivity of the detector is characterized by a noise equivalent strain curve and for detection of GWs it is required that the signal have a signal-to-noise ratio (SNR) of 8 or higher. Section 5 describes calibration of the LIGO detectors i.e., the procedure to convert the digital counts of the output photodetector to the dimensionless strain. This requires the interferometers to be characterized and modeled as accurately as possible (Abbott *et al.* (2017b)). The calibrated strain is then used for data analysis to determine the presence of the GWs which are typically buried in the detector noise and to extract astrophysical information from the signals. Section 6 elaborates how displacement fiducials are generated, the process that enables characterization and modeling of the interferometers and thus facilitate accurate and precise calibration of the entire detectors. It also explains how the uncertainty on the displacement fiducials are estimated. Section 7 implements the methodology explained in Section 6 to estimate the uncertainty in the generated displacement fiducials for the recent LIGO observing run O3. Section 8 and 9 describe a study of the effect of an overall calibration uncertainty on the information derived from the GWs, in particular, the impact of overall calibration errors on sky localizations of burst-like sources.

2. GRAVITATIONAL WAVES

The theory of SR was proposed by Albert Einstein in 1905. His theory was based on the postulate that the laws of physics are invariant in any inertial reference system. A consequence of SR is that the speed of light in vacuum is the same for all inertial observers, regardless of the motion of the source. A defining feature of SR is that time and space are not defined separately, instead space and time are interwoven into a single "spacetime". In spacetime, an event can be defined by the four coordinates x, y, z and t. If an observer measures two events as being separated in time by dt and by a spatial distance $dr^2 = dx^2 + dy^2 + dz^2$, then according to this theory, the spacetime interval is invariant and in free space is defined as $ds^2 = \eta_{\mu\nu} dx^\mu dx^\nu$ where $\eta_{\mu\nu}$ is the Minkowski metric given by $\eta_{\mu\nu} = diag(-, +, +, +)$ and $dx^\mu = (cdt, dx, dy, dz)$ (Einstein (1905); Griffiths (1999)). $c = 2.997\,924\,58 \times 10^8$ m/s is the speed of light in vacuum. Space and time are not separately invariant, but the combined spacetime interval is invariant.

The SR doesn't account for the effect of gravitational field on spacetime. The theory of GR was developed by Einstein in the years 1907–1915 to include the effects of gravitational field into the relativistic theory (Einstein (1915)) and will be discussed briefly in the following subsections. The derivations follow the notation in (Maggiore (2008)).

2.1. EINSTEIN'S EQUATION

In his theory of GR published in 1915, Einstein proposed matter and energy in the spacetime produces distortion resulting in curved spacetime. Gravity is an effect of the curvature of spacetime. Mathematically,

$$R_{\mu\nu} - \frac{1}{2} g_{\mu\nu} R = \frac{8\pi G}{c^4} T_{\mu\nu}\,, \tag{2.1}$$

where $g_{\mu\nu}$ is the metric tensor for curved spacetime, $R_{\mu\nu}$ is the Ricci tensor and R is the Ricci scalar. $T_{\mu\nu}$ is the stress-energy tensor that gives the flux of the μ-th component of the 4-momentum vector $p^\alpha = (E, \vec{p})$ across a surface with constant x^ν coordinate. $G = 6.67 \times 10^{-11}\,\mathrm{N\,kg^{-2}\,m^2}$ is the Newton's universal gravitational constant. Equations (2.1) are the Einstein's equations.

GR is a theory invariant under general coordinate transformations. Thus when $x^\mu \longrightarrow x'^\mu(x)$, where x'^μ is invertible, differentiable and has a differentiable inverse, the metric transforms as

$$g_{\mu\nu}(x) \longrightarrow g'_{\mu\nu}(x') = \frac{\partial x^\alpha}{\partial x'^\mu}\frac{\partial x^\beta}{\partial x'^\nu} g_{\alpha\beta}(x)\,, \tag{2.2}$$

where repeated indices indicate summation. This symmetry is referred to as the gauge symmetry of GR. The Ricci tensor $R_{\mu\nu}$ is obtained from Riemann curvature tensor $R^\alpha_{\mu\beta\nu}$ which is given by:

$$R^\alpha{}_{\mu\beta\nu} = \partial_\beta \Gamma^\alpha_{\nu\mu} - \partial_\nu \Gamma^\alpha_{\mu\beta} + \Gamma^\sigma_{\nu\mu}\Gamma^\alpha_{\sigma\beta} - \Gamma^\sigma_{\mu\beta}\Gamma^\alpha_{\sigma\nu}\,, \tag{2.3}$$

where the $\Gamma^\alpha{}_{\mu\nu}$ are the Christoffel symbols, given by:

$$\Gamma^\alpha{}_{\mu\nu} = \frac{1}{2}\eta^{\alpha\beta}(\partial_\mu h_{\nu\beta} + \partial_\nu h_{\mu\beta} - \partial_\beta h_{\nu\mu}). \tag{2.4}$$

The Ricci tensor is obtained by contracting the Riemann tensor, $R_{\mu\nu} = R^\alpha{}_{\mu\alpha\nu}$ and the Ricci scalar is obtained by contracting the Ricci tensor, $R = g^{\mu\nu}R_{\mu\nu}$

In the weak gravitational field limit, when the observer is far away from a given matter distribution so that spacetime is almost flat, the metric can be written as a sum of the Minkowski metric, $\eta_{\mu\nu}$, and a small perturbation $h_{\mu\nu}$:

$$g_{\mu\nu} = \eta_{\mu\nu} + h_{\mu\nu}\,, \tag{2.5}$$

where $|h_{\mu\nu}| \ll 1$ is a tensor describing the deformations of the geometry of flat spacetime induced due to matter distribution $T_{\mu\nu}$. By expanding the equations in h and keeping up to the first order, one gets the linearized equations.

After choosing a frame where Equation (2.5) holds true and the condition $|h_{\mu\nu}| \ll 1$ is satisfied, a residual gauge symmetry remains. Let us consider a coordinate transformation such that

$$x^{\mu} \longrightarrow x'^{\mu} = x^{\mu} + \xi^{\mu}(x). \tag{2.6}$$

Using the metric transformation as described in equation (2.2), the first order $h_{\mu\nu}$ transforms as

$$h_{\mu\nu}(x) \longrightarrow h'_{\mu\nu}(x') = h_{\mu\nu}(x) - (\partial_{\mu}\xi_{\nu} + \partial_{\nu}\xi_{\mu}). \tag{2.7}$$

Since $h_{\mu\nu}$ is assumed to be small, the metric can be approximated by the Minkowski metric in a small region around a point of interest. Therefore in that region there is invariance under Lorentz transformations. If $x^{\mu} \longrightarrow \Lambda^{\mu}_{\nu} x^{\nu}$, then by the definition of Lorentz transformation the matrix Λ^{μ}_{ν} satisfies

$$\Lambda^{\mu}{}_{\rho}\Lambda^{\nu}{}_{\sigma}\eta^{\rho\sigma} = \eta^{\mu\nu}\,, \tag{2.8}$$

and the metric transforms as

$$g_{\mu\nu}(x) \longrightarrow g'_{\mu\nu}(x') = \eta_{\mu\nu} + \Lambda^{\alpha}{}_{\mu}\Lambda^{\beta}{}_{\nu}h_{\alpha\beta}(x)\,, \tag{2.9}$$

which means $h_{\mu\nu}$ transforms as

$$h'_{\mu\nu}(x') = \Lambda^{\alpha}{}_{\mu}\Lambda^{\beta}{}_{\nu}h_{\alpha\beta}(x). \tag{2.10}$$

The above equation shows that $h_{\mu\nu}$ is a tensor under Lorentz transformations. Rotations don't break the condition $|h_{\mu\nu}| \ll 1$. Also boosts are restricted to only those which satisfies the condition. In addition, from Equation (2.2) it can be shown that $h_{\mu\nu}$ is invariant

under translations. Thus the linearized theory is invariant under Poincaré transformations. Equation (2.7) shows that linearized theory is invariant under a special class of local transformations as well. On the other hand, full GR does not have Poincaré symmetry, but has full coordinate invariance unlike the infintesimal version in Equation (2.7).

To linear order in $h_{\mu\nu}$, the Ricci tensor is given by

$$R_{\mu\nu} = \frac{1}{2}(\partial_\mu \partial^\alpha h_{\nu\alpha} + \partial_\nu \partial^\alpha h_{\mu\alpha} - \Box h_{\mu\nu} - \partial_\mu \partial_\nu h)\,, \tag{2.11}$$

and the Ricci scalar is given by

$$R = \partial^\mu \partial^\alpha h_{\mu\alpha} - \Box h\,, \tag{2.12}$$

where $\eta^{\mu\nu} h_{\mu\nu} = h$ and $\Box \equiv -\frac{1}{c^2}\frac{\partial^2}{\partial t^2} + \nabla^2$ is the d'Alembert operator. To linear order of $h_{\mu\nu}$, the $g_{\mu\nu}$ in the left-hand-side (LHS) of Equation (2.1) is replaced by $\eta_{\mu\nu}$. Thus the Einstein's equations can be rewritten by putting in the expressions for Ricci tensor and Ricci scalar from equations (2.11) and (2.12) as

$$R_{\mu\nu} - \frac{1}{2} g_{\mu\nu} R = \frac{1}{2}(\partial_\mu \partial^\alpha h_{\nu\alpha} + \partial_\nu \partial^\alpha h_{\mu\alpha} - \Box h_{\mu\nu} - \partial_\mu \partial_\nu h - \eta_{\mu\nu} \partial^\alpha \partial^\beta h_{\alpha\beta} + \eta_{\mu\nu} \Box h) = \frac{8\pi G}{c^4} T_{\mu\nu}. \tag{2.13}$$

The linearized equations of motion can be written in a more compact form by defining

$$\overline{h}_{\mu\nu} = h_{\mu\nu} - \frac{1}{2}\eta_{\mu\nu} h. \tag{2.14}$$

Equation (2.13) becomes:

$$\Box \overline{h}_{\mu\nu} + \eta_{\mu\nu} \partial^\rho \partial^\sigma \overline{h}_{\rho\sigma} - \partial^\rho \partial_\nu \overline{h}_{\rho\mu} - \partial^\rho \partial_\mu \overline{h}_{\rho\nu} = -\frac{16\pi G}{c^4} T_{\mu\nu}. \tag{2.15}$$

This is the linearized Einstein's equations.

Using gauge freedom, Equation (2.7), the Lorentz gauge can be chosen such that

$$\partial^{\mu}\overline{h}_{\mu\nu} = 0. \tag{2.16}$$

In terms of $\overline{h}_{\mu\nu}$, equation (2.7) takes the form

$$\overline{h}_{\mu\nu} \longrightarrow \overline{h}'_{\mu\nu} = \overline{h}_{\mu\nu} - (\partial_{\mu}\xi_{\nu} + \partial_{\nu}\xi_{\mu} - \eta_{\mu\nu}\partial_{\alpha}\xi_{\alpha}), \tag{2.17}$$

and the gauge condition can be written as

$$\partial^{\mu}\overline{h}_{\mu\nu} \longrightarrow (\partial^{\mu}\overline{h}_{\mu\nu})' = \partial^{\mu}\overline{h}_{\mu\nu} - \Box\xi_{\mu} = 0. \tag{2.18}$$

Thus if initially $\partial^{\mu}\overline{h}_{\mu\nu} = f_{\mu}(x)$, where $f_{\mu}(x)$ is some function, to impose Lorentz gauge, ξ_{μ} must be

$$\Box\xi_{\mu} = f_{\mu}(x). \tag{2.19}$$

Given any f_{μ}, the above equation can be solved. The solution is given by

$$\xi_{\mu} = \int d^4y\, G(x-y) f_{\mu}(x), \tag{2.20}$$

where $G(x)$ is the Green's function of the d'Alembertian operator.

In the Lorentz gauge, the last three terms on the LHS of the Equation (2.15) vanish and the linearized Einstein's equations become

$$\Box\overline{h}_{\mu\nu} = -\frac{16\pi G}{c^4}T_{\mu\nu}. \tag{2.21}$$

The above equation is a wave equation which tells us that $T_{\mu\nu}$ is the source of the metric perturbation, $\overline{h}_{\mu\nu}$. Therefore, $h_{\mu\nu}$ can be interpreted as describing a GWs which propagates through spacetime (Einstein (1916)).Note that $h_{\mu\nu}$ is a symmetric 4×4 matrix, , i.e. , it should have ten independent components. But, Equation (2.16) gives us four conditions, which reduces the number of independent components to six from ten.

Equations (2.16) and (2.21) together imply $\partial^{\mu} T_{\mu\nu} = 0$, which is the energy-momentum conservation in linearized theory.

2.1.1. GWs in Vacuum. Equation (2.21) tells us about the generation and propagation of GWs. To study how these GWs propagate, first consider regions of spacetime where $T_{\mu\nu} = 0$, , i.e. , outside the source:

$$\Box \overline{h}_{\mu\nu} = 0. \tag{2.22}$$

Now, the Lorentz gauge does not fix the gauge completely. Under the coordinate transformation, $\partial^{\mu} \overline{h}_{\mu\nu}$ transforms as in Equation (2.18). The condition that $\partial^{\mu} \overline{h}_{\mu\nu} = 0$ can be preserved by an additional coordinate transformation $x^{\mu} \rightarrow x^{\mu} + \xi^{\mu}$ with $\Box \xi_{\mu} = 0$.

The component ξ^0 can be chosen such that $\overline{h} = 0$, which implies $\overline{h}_{\mu\nu} = h_{\mu\nu}$ along with the three $\xi^i(x)$ such that $h^{0i}(x) = 0$. Thus the Lorentz condition with $\mu = 0$ is

$$\partial^0 h_{00} + \partial^i h_{0i} = 0. \tag{2.23}$$

Roman indices indicate the three spatial coordinates only and the Greek indices indicate all the four coordinates. Since $h_{0i}(x) = 0$ is fixed, the above equation reduces to

$$\partial^0 h_{00} = 0. \tag{2.24}$$

Thus h_{00} is constant in time. A time-independent term h_{00} corresponds to the Newtonian potential of the source that generated the GWs. The GWs itself is time-dependent, therefore $\partial^0 h_{00} = 0$ implies $h_{00} = 0$. Therefore, all the 4 components of $h_{0\mu}$ is zero. The Lorentz gauge now reduces to $\partial^i h_{ij} = 0$ and the condition for vanishing trace can be rewritten as $h^i{}_i = 0$. The set of conditions

$$h^{0\mu} = 0\,, \tag{2.25a}$$

$$h^i{}_i = 0\,, \tag{2.25b}$$

$$\partial^i h_{ij} = 0\,, \tag{2.25c}$$

define the transverse-traceless (TT) gauge. The TT gauge is imposed, in addition to the Lorentz gauge, to completely fix the gauge. By imposing the Lorentz gauge, the number of independent components of the symmetric $h_{\mu\nu}$ matrix reduces from ten to six in the previous subsection. By imposing the TT gauge, the number of independent components further reduces to two, since four more conditions are imposed from $\Box\xi_\mu = 0$.

The solutions of Equation (2.22) in the TT gauge are

$$h^{TT}_{\mu\nu} = A_{\mu\nu}(\mathbf{k}) e^{ik^\sigma x_\sigma}\,, \tag{2.26}$$

where $k^\sigma = (\omega/c, \mathbf{k})$ is the wave vector and $A_{\mu\nu}$ is the *polarization tensor* which gives us information about the wave amplitude and polarization. $k^\rho k_\rho = 0$, , i.e. , the wave vector is null which implies that the frequency of the GWs, ω, is given by $\omega/c \equiv |\mathbf{k}|$. For a plane wave with $\hat{n} = \mathbf{k}/|\mathbf{k}|$ the non-zero components of h^{TT}_{ij} are in a plane transverse to $\mathbf{k}$.

Assuming that the wave propagates in the z-direction,

$$h_{\mu\nu}^{TT} = \begin{pmatrix} 0 & 0 & 0 & 0 \\ 0 & A_{11} & A_{12} & 0 \\ 0 & A_{12} & -A_{11} & 0 \\ 0 & 0 & 0 & 0 \end{pmatrix} e^{i(kz-\omega t)} \tag{2.27}$$

$A_{\mu\nu}$ has only two independent components which means that a GWs can be completely described by two dimensionless amplitudes A_{11} and A_{12}. It is shown later that in the TT gauge, A_{11} and A_{12} are commonly called the 'plus' and 'cross' polarizations of the wave, respectively. Since they are orthogonal polarization states, it is impossible to construct the (+) pattern from the (×) pattern and vice versa.

2.1.2. GWs From Weak-field Sources. Next, consider a situation in which the stress-energy tensor is non-zero, but the linearized theory is still valid.

The metric perturbation contains both radiative and non-radiative degrees of freedom tied to the matter sources along with gauge degrees of freedom. The TT part of the metric perturbation obeys a wave equation in all gauges and hence is truly radiative.

Using the retarded Green function, $G(x-x')$ which gives the effect for the d'Alembertian operator, $\Box$, at $\mathbf{x}$ of a source element located at $\mathbf{x}'$, the solution to the Equation (2.21) is

$$\overline{h}_{\mu\nu} = -\frac{16\pi G}{c^4} \int d^4x' G(x-x') T_{\mu\nu}(x') \, . \tag{2.28}$$

In the above equation $G(x-x')$ satisfies

$$\Box_x G(x-x') = \delta^4(x-x') \, , \tag{2.29}$$

where $\Box_x$ is the d'Alembertian operator with the derivatives taken with respect to x. The solution of the Equation (2.29) is given by

$$G(x-x') = -\frac{1}{4\pi|\mathbf{x}-\mathbf{x}'|}\delta(x^0_{\rm ret}-x^0)\,, \tag{2.30}$$

where $x'^0 = ct'$, $x'^0_{ret} = ct'_{ret}$ and the retarded time is $t_{\rm ret} = t - |\mathbf{x}-\mathbf{x}'|/c$.

Then the Equation (2.28) becomes

$$\overline{h}_{\mu\nu}(x^\alpha) = -\frac{4G}{c^4}\int d^3x' \frac{1}{|\mathbf{x}-\mathbf{x}'|} T_{\mu\nu}(t-\frac{|\mathbf{x}-\mathbf{x}'|}{c}, \mathbf{x}'). \tag{2.31}$$

The notation $\mathbf{x} = r\hat{\mathbf{n}}$ is used and the typical radius of the source is defined as d. Assuming that the size of the GWs source is much less than the distance to the observer, then at $r \gg d$

$$|\mathbf{x}-\mathbf{x}'| = r - \mathbf{x}'\cdot\hat{\mathbf{n}} + ... \tag{2.32}$$

At large distances from the source, when expanding Equation (2.31) only the leading order term in $1/r$ in the limit $r \to \infty$ at fixed t is retained, thus Equation(2.32) reduces to $|\mathbf{x}-\mathbf{x}'| = r$. In addition, it is assumed that $\lambda/2\pi \gg d$, i.e. the internal motion of the source can be ignored and the radiation emission is governed by the lowest multipole moment. Under these assumptions, Equation (2.31) reduces to

$$\overline{h}_{\mu\nu}(x^\alpha) = -\frac{4G}{c^4 r}\int d^3x' T_{\mu\nu}(t-r/c, \mathbf{x}'). \tag{2.33}$$

The stress-energy tensor is non-zero only inside the source, so the integral in Equation (2.33) is restricted to $|\mathbf{x}'| \le d$. As the radiative degrees of freedom are contained in the spatial part of the metric, $\overline{h}_{ij}$ is considered from now on. Combining Equation (2.33) with the conservation of the stress-energy tensor in linearized gravity, the spatial components of

the metric $\overline{h}_{\mu\nu}$ is obtained. From the conservation of the stress-energy tensor, it follows that

$$\partial_0^2 T^{00} = \partial_k \partial_l T^{kl}. \tag{2.34}$$

Multiplying both sides of the above equation by $x^i x^j$ it can be shown that,

$$T^{ij} = \frac{1}{2}[\partial_0^2 (T^{00} x^i x^j) - \partial_k \partial_l (T^{kl} x^i x^j) + 2\partial_k (T^{ik} x^j + T^{kj} x^i)]. \tag{2.35}$$

Thus the spatial components of l.h.s of the Equation (2.33) can be written as

$$\frac{4G}{c^4 r} \int d^3x T_{ij} = \frac{2G}{c^4 r} \partial_0^2 \int d^3x (T_{00} x^i x^j). \tag{2.36}$$

Using the definition $T^{00} = \rho c^2$, where ρ is the energy density and Equation (2.33) and Equation (2.36), the spatial components of $\overline{h}_{\mu\nu}$ are

$$\begin{aligned} \overline{h}_{ij}(x^\alpha) &= -\frac{2G}{c^4 r} \frac{\partial^2}{\partial t^2} \int d^3x' \rho(t, x') x'^i x'^j \\ &= -\frac{2G}{c^4 r} \frac{\partial^2}{\partial t^2} I_{ij}(t - r/c)\,, \end{aligned} \tag{2.37}$$

where I_{ij} is the second moment of the mass distribution defined by

$$I_{ij} = \int d^3x' \rho(t, x') x'^i x'^j. \tag{2.38}$$

The tensor, I_{ij}, is the moment of inertia tensor. When the trace part is removed from the moment of inertia tensor, the quadrupole moment tensor is obtained, which is given by

$$Q_{ij} = \int d^3x' \rho(t, \mathbf{x})(x_i x_j - \frac{1}{3} x^2 \delta_{ij}). \tag{2.39}$$

The perturbation in TT gauge becomes

$$h_{ij}^{TT}(x^{\alpha}) = -\frac{2G}{c^4 r}\frac{\partial^2}{\partial t^2}Q_{ij}(t - r/c). \tag{2.40}$$

To leading order in a multipolar expansion, gravitational waves are generated by any time-varying quadrupole moment. Mass conservation excludes any monopole radiation. For gravity, the rate of change of the mass dipole moment is proportional to the linear momentum of the system and the change of the magnetic dipole is proportional to the angular momentum of the system, both of which are conserved quantities. The conservation of linear and angular momentum exclude dipole radiation. Thus, the lowest order term is quadrupolar radiation. Equation (2.40) is referred to as the quadrupolar approximation.

2.2. ANGULAR DISTRIBUTION OF QUADRUPOLE RADIATION

It is desirable to obtain the waveform of GWs emitted in a generic direction $\hat{n}$ within the quadrupolar approximation. In order to do that, the non-TT components of $\overline{h}_{ij}$ in Equation (2.37) can be projected out by defining a tensor $\Lambda_{ij,kl}$ such that $h_{ij}^{TT} = \Lambda_{ij,kl}h_{kl}$ where h_{ij} is the spatial component of $h_{\mu\nu}$. The tensor, $\Lambda_{ij,kl}$, is given by

$$\Lambda_{ij,kl} = P_{ik}P_{jl} - \frac{1}{2}P_{ij}P_{kl}\,, \tag{2.41}$$

where P_{ij} is a projector operator defined as $P_{ij} = \delta_{ij} - n_i n_j$ with $\hat{n}$ being the direction in which the GWs propagates. The projector operator eliminates the vector components parallel to $\hat{n}$, leaving only the transverse components. $\Lambda_{ij,kl}$ is also a projector operator which is transverse in all indices and traceless in (ij). Therefore, if the GWs propagates along the z-direction, the projector operator P_{ij} is a diagonal matrix, diag(0,1,1,0), i.e., the projection is on the x-y plane and $\hat{n} = \hat{z}$. Then $\Lambda_{ij,kl}\ddot{Q}_{ij}$ can be computed, where the double

dots indicate the second derivative with respect to time, which gives

$$\Lambda_{ij,kl}\ddot{Q}_{ij} = (P_{ik}P_{jl} - \frac{1}{2}P_{ij}P_{kl})\ddot{Q}_{kl} = (P\ddot{Q}P)_{ij} - \frac{1}{2}P_{ij}Tr(P\ddot{Q}). \tag{2.42}$$

For $P_{ij} = \text{diag}(1, 1, 0)$, in the matrix form is given by,

$$\Lambda_{ij,kl}\ddot{Q}_{kl} = \begin{pmatrix} 0 & 0 & 0 & 0 \\ 0 & (\ddot{Q}_{11} - \ddot{Q}_{22})/2 & \ddot{Q}_{12} & 0 \\ 0 & \ddot{Q}_{21} & -(\ddot{Q}_{11} - \ddot{Q}_{22})/2 & 0 \\ 0 & 0 & 0 & 0 \end{pmatrix}_{ij} . \tag{2.43}$$

Equation (2.40) gives the amplitude of the plus- and cross-polarized wave propagating in the z-direction to be

$$h_+ = \frac{G}{rc^4}(\ddot{Q}_{11} - \ddot{Q}_{22}) , \tag{2.44a}$$

$$h_\times = \frac{2G}{rc^4}\ddot{Q}_{12} , \tag{2.44b}$$

where the RHS is computed at a retarded time $(t - r/c)$. The h_+ and h_x are defined as the components of h_{ij} in the plane perpendicular to the direction of propagation. Thus these are the polarization amplitudes.

For a wave propagating in an arbitrary direction $\hat{n}$, a frame S' can be introduced with unit vectors $(\hat{u}, \hat{v}, \hat{n})$ such that $\hat{n}$ in the S' frame is given by (0,0,1) and in the S frame with unit vectors $(\hat{x}, \hat{y}, \hat{z})$ it is given by $\hat{n} = (\sin\theta\sin\phi, \sin\theta\cos\phi, \cos\theta)$. Alternately, it can be written as $n_i = R_{ij}n'_j$ where R_{ij} is the rotation matrix given by

$$R = \begin{pmatrix} \cos\phi & \sin\phi & 0 \\ -\sin\phi & \cos\phi & 0 \\ 0 & 0 & 1 \end{pmatrix}\begin{pmatrix} 1 & 0 & 0 \\ 0 & \cos\theta & \sin\theta \\ 0 & -\sin\theta & \cos\theta \end{pmatrix} \tag{2.45}$$

In the S' frame, the wave propagates along the z' direction. Thus using Equation (2.44) with Q_{ij} being replaced by Q'_{ij} which is the quadrupole moment in S' frame. They are related by $Q'_{ij} = R^T Q R$ where R^T is the transpose of the matrix R. Plugging the resulting values of Q'_{ij} in Equation (2.44) for the primed frame, the amplitude of the plus- and cross-polarized wave propagating in a generic direction can be obtained.

$$h_+(t,\theta,\phi) = \frac{G}{rc^4}[\ddot{Q}_{11}(\cos^2\phi - \sin^2\phi\cos^2\theta) + \ddot{Q}_{22}(\sin^2\phi - cos^2\phi\cos^2\theta) - \ddot{Q}_{33}\sin^2\theta - \ddot{Q}_{12}\sin 2\phi(1+\cos^2\theta) + \ddot{Q}_{13}\sin\phi\sin 2\theta + \ddot{Q}_{23}\cos\phi\sin 2\theta] \tag{2.46a}$$

$$h_\times = \frac{G}{rc^4}[(\ddot{Q}_{11} - \ddot{Q}_{22})\sin 2\phi\cos\theta + 2\ddot{Q}_{12}\cos 2\phi\cos\theta - 2\ddot{Q}_{13}\cos\phi\sin\theta + 2\ddot{Q}_{23}\sin\phi\sin\theta \tag{2.46b}$$

The above equations enable calculation of the angular distribution of the quadrupolar radiation for a given Q_{ij}.

Now that we have discussed expression for the waveform of GWs emitted in a generic direction, in the next section, we will discuss some of the astrophysical sources that generate these waveforms and the techniques employed by the LIGO-Virgo-KAGRA (LVK) network to identify these waveforms.

3. ASTROPHYSICAL SOURCES OF GRAVITATIONAL WAVES

In the previous section, we showed that sources of GWs must possess a time-varying quadrupole mass moment or higher order mass moments. This section is a summary of the different astrophysical sources of GWs and techniques to detect their signals. It also summarizes the current results of the LVK searches for different GW signals.

3.1. GWS FROM COMPACT BINARY COALESCING OBJECTS

The GW signals from binary compact objects such as BBHs, BNSs and NSBHs are short-lived, lasting for a few milliseconds to minutes in the detectors. As the GWs carry away energy, the orbit of the binary system decays further increasing the amplitude of the waves until the compact objects merge. The increasing amplitude and frequency of the waves result in a 'chirp' waveform. A binary system can radiate up to a few percent of its total mass as GWs in the last stages of the inspiral process (Maggiore (2008)).

In a simple approximation, one can calculate the waveform of the GWs emitted during the inspiral phase of a compact binary coalescence (CBC) by treating the two compact objects as point-like masses m_1 and m_2 at positions r_1 and r_2. In the center-of-mass frame (COM), the system is described by the reduced mass $\mu = m_1 m_2/(m_1 + m_2)$ and the relative coordinate $r = r_2 - r_1$. Assuming that there is no back-reaction on the motion of the system due to GW emission and choosing a frame so that the orbit lies on the (x, y) plane, the trajectory of the system is given by

$$\begin{aligned} x_0(t) &= R\cos(\omega t)\,, \\ y_0(t) &= R\sin(\omega t)\,, \end{aligned} \tag{3.1}$$

where ω is the orbital frequency and R is in initial the orbital radius. In the COM frame, from Equation (2.38) the non-zero components of the mass quadrupole moment are given by

$$\begin{aligned} I_{11} &= \mu R^2 \frac{1+\cos(2\omega t)}{2}\,, \\ I_{22} &= \mu R^2 \frac{1-\cos(2\omega t)}{2}\,, \\ I_{12} &= \mu R^2 \frac{\sin(2\omega t)}{2}\,. \end{aligned} \tag{3.2}$$

Plugging these values into Equation (2.37), the GW amplitudes are, for a system when the normal to the plane of the orbit is along the line of sight:

$$\begin{aligned} h_+ &= \frac{4G\mu\omega^2 R^2}{c^4 r}\cos(2\omega t_{\rm ret})\,, \\ h_\times &= \frac{4G\mu\omega^2 R^2}{c^4 r}\sin(2\omega t_{\rm ret})\,, \end{aligned} \tag{3.3}$$

where $t_{\rm ret} = (t - r/c)$ is the retarded time. The GW frequency is twice the orbital frequency of the binary system and the GW amplitude is inversely proportional to r.

The masses of the objects involved determine how long the emitted GWs last in the detector's frequency band. Compact binaries like BBHs produce signals that typically last only a fraction of seconds long in the LIGO sensitive band. On the other hand, BNS mergers can produce signals that may last minutes in the detector. Advanced ground-based GW detectors can detect coalescing BBHs with component masses of the order of $10\,\mathrm{M}_\odot$ up to a distance of several gigaparsecs (Gpc) (Abbott *et al.* (2021a)).

If the plane of the orbit is tilted at an angle ι, Eqs. (3.3) become

$$\begin{aligned} h_+ &= \frac{4G\mu\omega^2 R^2}{c^4 r}\left(\frac{1+\cos^2\iota}{2}\right)\cos(2\omega t_{\rm ret})\,, \\ h_\times &= \frac{4G\mu\omega^2 R^2}{c^4 r}\cos\iota\sin(2\omega t_{\rm ret})\,. \end{aligned} \tag{3.4}$$

The GW is linearly polarized for an edge-on orbit, $h_\times = 0$. For $\iota = 0$, both h_+ and $h_\times$ have the same amplitude, but $h_+ \propto \cos(2\omega t_{\rm ret})$ and $h_\times \propto \sin(2\omega t_{\rm ret})$. Thus the GWs are circularly polarized in (h_+, $h_\times$) plane. The GW is elliptically polarized for any other value of ι.

Matched filtering is the standard method to extract CBC signals from the detector noise. For the details on matched filtering , see (Maggiore (2008)).

The Advanced LVK network of GW detectors have identified confirmed 90 CBC detections so far. 76 of these detections were observed in the latest observing run, O3 (Abbott *et al.* (2021a)). They include the first NSBH detections (Abbott *et al.* (2021c), cite), a BBH with total mass over $150M_\odot$ (Abbott *et al.* (2020b)), and a highly asymmetric system with mass ratio q $\sim$ 9 of ambiguous nature (Abbott *et al.* (2021b)). Additionally, the BNS detection of GW170817 (Abbott *et al.* (2017c)) with an EM counterpart heralded the era of multi-messenger astronomy (MMA). A second BNS without an EM counterpart was also observed GW190425 Abbott *et al.* (2021a).

3.2. CONTINUOUS GWS

The most likely sources of continuous waves (CWs) that can be observed by ground-based GW detectors are non-axisymmetric, rapidly rotating NS. Searches for CWs have been carried out targeting various isolated sources, including known pulsars (Abbott *et al.* (2005)), NSs close to the galactic center and young supernova (SN) remnants (Aasi *et al.* (2013, 2015b)) and NSs in globular clusters (Abbott *et al.* (2017f)). Searches have also been conducted over the whole sky for CWs (Abbott *et al.* (2021d)). Young NSs may have larger non-axisymmetries than older ones and consequently may produce stronger GW emissions (Riles (2017)). As the star ages, various processes such as tectonic, thermal, or other relaxation processes work to reduce the asymmetries introduced in the birth process.

Young NSs are therefore promising targets for CW searches. Characterizing properties of these continuous GWs will provide insights into their internal structure. The expected amplitude of these generated GWs is of the order of 10^{-25}.

The latest all-sky search for continuous, nearly monochromatic GWs in the range 20 – 2000 Hz from rapidly rotating isolated NS using LIGO and Virgo data yielded no credible CW signals (Abbott *et al.* (2021e)). Instead, 95% confidence level upper limits were placed on possible source signal amplitudes. The lowest upper limits on linearly polarized GW strain amplitudes are $\sim 1.7 \times 10^{-25}$, whereas for the circularly-polarized GW strain amplitudes are $\sim 6.3 \times 10^{-26}$ (Abbott *et al.* (2021e)). A targeted search for CWs from NSs in young SN remnants with the O3a data also yielded no evidence of CWs but placed constraints on the GW strain, as well as the ellipticity and r-mode amplitudes of the sources (Abbott *et al.* (2021i)).

3.3. STOCHASTIC GW BACKGROUND

A Stochastic GW background (SGWB) consists of random signals produced by the superposition of many weak, uncorrelated and unresolved sources that can be of cosmological or astrophysical origin (Martinovic *et al.* (2021)). A variety of early universe processes, like quantum vacuum fluctuations during inflation (Guth (1981)), first order phase transitions, or cosmic strings can lead to a SGWB (Jeannerot *et al.* (2003)). An astrophysical contribution to the SGWB comes from the superposition of unresolved GW transients signals for example from CBC events. Detecting an astrophysical SGWB would be important to obtain information about the mass range for NS and BH progenitors and the rate of compact binaries.

LVK searches generally assume the SGWB to be stationary, isotropic and not polarized. The SGWB can be quantified in terms of

$$\Omega_{GW} = \frac{4\pi^2}{3H_0^2} f^3 S_h(f)\,, \tag{3.5}$$

where H_0 is the Hubble constant, f is the frequency and $S_h(f)$ is the single-sided power spectal density (PSD) of the stochastic background.

No evidence of a SGWB has been found to date. However, 95% confidence-level upper limits were placed on the normalized GW energy density spectrum from extended sources ($\Omega_{GW} < (0.57 - 9.3) \times 10^{-9}\mathrm{sr}^{-1}$) and other parameters using data from the O3 LIGO-Virgo observing runs. These limits improve upon by a factor of $2.9 - 3.5$ with respect to the previous observing runs (Abbott *et al.* (2021g)).

When a SGWB is successfully detected, there will be the challenge of identifying the sources that contribute to it. Untangling these signals will deepen our knowledge of merger rates and population models (Zhu *et al.* (2013)), our understanding of exotic objects (Jeannerot *et al.* (2003); Regimbau and Pacheco (2006)) and in particular early universe models (Abbott *et al.* (2009b)). Although efforts have been made to separate the astrophysical and cosmological contributions to the SGWB using the data from the O3 run, the current network of GW detectors may not be sufficiently sensitive to distinguish different sources. However, the detection of SGWB may look promising for the future generation detectors (Martinovic *et al.* (2021)).

3.4. GW BURSTS

Burst GW transients are emitted by extremely energetic events such as core collapse supernova (CCSN) explosions, magnetars, gamma ray bursts (GRBs) or even cosmic strings. They may also be originated by unknown and/or unforeseen GW sources. As GW bursts come from explosive and complicated phenomena, it is difficult to accurately predict their waveforms. Therefore, algorithms to detect them are designed to use minimal assumptions. Current LVK searches target burst transients in the frequency range from 32 Hz to 4096 Hz

(Abbott *et al.* (2019b)). This frequency range covers a wide parameter space of sources, including GWs from mergers of compact objects. Different algorithms increase our ability to detect a wide range of signals from both CBC and GW bursts. Thus, multiple algorithms are used to independently verify search results (Abbott *et al.* (2019b)). One of these algorithms which is widely used in LVK searches is coherent WaveBurst (cWB) (Drago *et al.* (2020)). In this section we will briefly describe its basic features. A more detailed discussion is included in Section 8.

cWB is a wavelet-based algorithm which applies the maximum-likelihood-ratio statistics on detected excess power (Drago *et al.* (2020)). Data streams from all detectors are first conditioned to remove persistent lines and noise artifacts. Next, data is converted to the time-frequency (TF) domain with the Wilson-Daubechies-Meyer wavelet transform and whitened. Pixels whose energy are larger than a given threshold are retained for further analyses. The chosen TF pixels from all detectors are combined by a constrained likelihood function that for each incoming direction takes into account the interferometer antenna patterns and the detected time delays. The likelihood is then maximized with respect to the sky position. An event is identified when a signal coherence test statistic calculated on the selected TF pixels exceeds a predetermined threshold. The cWB analyses are performed by dividing the observing run into reduced periods of consecutive time epochs (called "chunks"). The background distribution of triggers for each individual chunk is then calculated by time-shifting the data of one detector with respect to the other detectors by an amount larger than the time of flights between detectors. Performing the analyses in chunks also accounts for the fluctuating noise levels of the detectors over the duration of the observing run. The significance of each trigger found in real coincident data is then calculated by comparing the coherent network SNR with the background distribution of the chunk to which it belongs (Abbott *et al.* (2019b)).

LVK searches for GW bursts have not yet yielded any detection, although some theoretical models suggest that a CCSN can produce a GW signal with amplitude of the order of $\sim 10^{-21}$ at a distance of 10 kpc under the assumption that $10^{-7} M_{\odot}$ is radiated in GWs (Sathyaprakash and Schutz (2009)). A search for GW transients associated with five CCSNs within approximately 20 Mpc using Advanced LIGO and Advanced Virgo data yielded no GW detections (Abbott *et al.* (2020c)). However, detection efficiency as a function of the distance for waveforms derived from multidimensional numerical simulations and phenomenological extreme emission models were calculated. The sources with neutrino-driven explosions may be detectable up to a distance of $\sim$ 5 kpc at 50 % efficiency. Magnetorotationally driven extreme emission CCSNs may be detected up to a distance of $\sim$ 54 kpc and $\sim$ 28 Mpc, respectively (Abbott *et al.* (2020c)). For the first time, the first supernova model constraints were provided based on GW data with a standard candle approach. GW energy released at 235 and 1304 Hz was constrained to be around $\sim 10^{-3} M_{\odot} c^2$ and $\sim 10^{-1} M_{\odot} c^2$, respectively (Abbott *et al.* (2020c)). In case of magnetars, results of a search for short and intermediate-duration GW signals in Advanced LIGO's second observing run provided no evidence of a signal. However, upper bounds were placed on the dimensionless strain ranging from 1.1×10^{-22} at 150 Hz to 4.4×10^{-22} at 1550 Hz at 50% detection efficiency. Also the upper bounds were placed on the isotropic GW energy at 3.4×10^{44}erg at 150 Hz assuming optimal orientation (Abbott *et al.* (2019e)). Targeted analyses for GWs associated with Fermi (Meegan *et al.* (2009)) and Swift (Gehrels *et al.* (2004)) GRBs reported during the O3a LIGO–Virgo observing run yielded no GW signal in association with the GRBs (Abbott *et al.* (2021h)). Lower bounds have been placed on the distances to the progenitors of all GRBs that were analyzed for different emission models (Abbott *et al.* (2021h)). Among all sky searches long duration search, which covers the range of 2 – 500 sec in duration and a frequency band of 24 – 2048 Hz, also yielded no significant triggers using GW data from the O3 run. However, sensitivity limits could be placed on the signal strength of GWs characterized by the root-sum-square amplitude as a

function of waveform morphology. These limits improve upon the results from the previous observing run by an average factor of 1.8 (Abbott *et al.* (2021f)). The short duration all-sky search detected GWs from several BBH mergers which have been identified by previous analyses. No other significant events were found (Abbott *et al.* (2019b)). However, the search established upper limits on the source rate-density as function of the characteristic frequency of the signal and sensitivity for a variety of signal waveforms. These upper limits are a factor of ~ 3 lower than the first observing run, with a 50% detection probability for GW emissions with energies of $\sim 10^{-9}\,\mathrm{M}_{\odot}c^2$ at 153 Hz (Abbott *et al.* (2019b)).

In the next section we will describe how LIGO operates and detects GW signals produced by the various sources mentioned here. The following sections primarily focus on LIGO since the experimental work described in the later sections were carried out at LIGO. Virgo and KAGRA detectors follow the same basic design with some technical differences.

4. LIGO DETECTORS

In the previous section it was shown that GWs are quadrupolar and transverse in nature. As GWs travel, they compress the spacetime in one direction while stretching it in a perpendicular direction in a plane perpendicular to their direction of propagation. This feature is exploited when employing laser interferometer as GW detectors. Typical differential length variations induced by a GW are of the order of 10^{-18} m. Detecting these small effects require a highly sensitive interferometer (Abbott *et al.* (2009a)). Advanced LIGO is a ground-based interferometric GW observatory that is a part of a wider global network of ground-based GW detectors. To date the detector network has detected $\sim$ 90 GW signals all from CBCs (Abbott *et al.* (2021a)). This section provides a brief description of the LIGO detectors, the major sources of noise that limits LIGO's sensitivity and how LIGO detects GWs. The derivations in Subsection 4.3 follow the notations in Maggiore (2008).

4.1. LIGO DETECTORS

Advanced LIGO consists of two identical interferometric detectors with 4 km long arms, one at Hanford, WA USA and the second one at Livingston, LA USA (Aasi *et al.* (2015a)). Apart from the twin LIGO detectors, there are other interferometric GW detectors operational around the world. This global network includes the VIRGO detector in Cascina, Italy (Acernese *et al.* (2015)) which has 3 km long arms, the KAGRA detector in Japan which operates underground and has cryogenically cooled mirrors to reduce unwanted contributions from seismic and thermal noise (Akutsu *et al.* (2019)), and the GEO600 detector in Hannover, Germany with 600 m long arms (Luck *et al.* (2010)). A third LIGO detector is slated to join the global network in a few years time in India (Iyer *et al.* (2011)). Employing multiple geographically distributed detectors around the world enable coincident GW detection with increased confidence and improved source sky localization.

The LIGO detectors are designed to be sensitive to GW frequencies in the range $20 - 2000$ Hz with a peak sensitivity to differential length variations of the order of $1.0 \times 10^{-20}\,\mathrm{m}/\sqrt{\mathrm{Hz}}$ at frequencies near 200 Hz. The sensitivity of the detectors are limited by noise contributions from different sources at various frequency regions. A few of the main sources of noise will be discussed in Section 4.2.

4.1.1. Power-recycled Fabry-Perot Michelson Interferometers. The LIGO detectors are kilometer-scale Michelson interferometers, see Figure 4.1. The interferometer laser beam is split into two equal beams, which travel through the perpendicular vacuum tubes, or arms of the interferometer. These beams are reflected by highly reflective mirrors at the end of the arms, referred to as the end test masses (ETMs). The two reflected beams them recombine at the beamsplitter (BS). LIGO operates close to the dark fringe such that nearly all carrier power is directed towards the symmetric port and the signal towards the antisymmetric port (Abbott *et al.* (2009a)).

The interferometer laser is a diode-pumped Nd:YAG laser operating at 1064 nm (Abbott *et al.* (2009a)). Before entering the interferometer, the pre-stabilized laser beam is sent through a series of mode cleaners and input optics to further improve the power stability and to filter out higher transverse electromagnetic (TEM) modes. The input mode cleaner (IMC) is a triangular cavity that allows only (TEM00) mode to resonate in the cavity and completely transmit it to the interferometer (Abbott *et al.* (2009a). The IMC also suppresses frequency fluctuations of the laser when employing Pound-Drever-Hall locking technique to lock the cavity in resonance (Drever *et al.* (1983)). There is also an output mode cleaner (OMC) at the antisymmetric port before the laser beam reaches the photodetector. The OMC rejects the non-fundamental modes that might have reappeared as the laser traveled through the interferometer (Smith (2012)).

As a GW propagates through the plane of the detector, the spacetime stretches and compresses in perpendicular direction in the plane orthogonal to the direction of the propagation of the wave. As a result, the interferometer output at the antisymmetric port

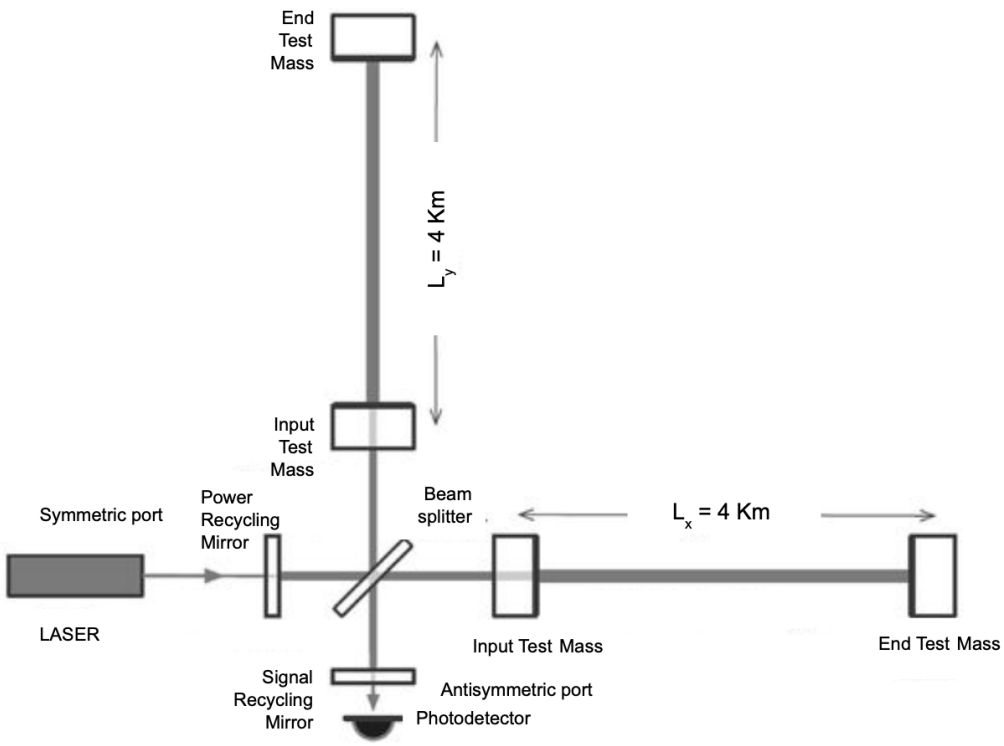

Figure 4.1. Schematic diagram of the LIGO interferometer layout showing the Michelson interferometer with the power recycling cavity at the input end, the signal-recycling cavity at the signal readout port and the Fabry-Perot cavities ~ 4 km-long in each of the perpendicular arms.

changes indicating presence of the GW. As mentioned earlier, in order to detect GWs, LIGO must be sensitive to DARM length variations of the order of 10^{-18} m. To achieve this level of sensitivity, several enhancements to the basic Michelson interferometer design have been introduced over the years.

4.1.1.1. Fabry-Perot cavities. The most significant of these enhancements are the Fabry-Perot optical cavities in each arm of the interferometer. These cavities increase the effective lengths of the arms and the interaction time of the interferometer carrier light with the GWs, thus amplifying the signal at the output photodetector. These cavities are realized by placing partially reflective mirrors at the beginning of the arms, referred to as the input test masses (ITMs), as shown in Figure 4.1. These cavities are on resonance if their length is an integer multiple of the laser half-wavelength, or the phase ϕ is an integer multiple of

2π. The round trip phase in each arm is given by $\phi = 4\pi L/\lambda$, where λ is the wavelength of the laser light and L is the average length of the interferometer arm. In the case of a simple Michelson interferometer, the phase shift $\Delta\phi$ is proportional to L. However, with Fabry-Perot cavities, phase shift is proportional to $L \times \mathcal{F}$, where $\mathcal{F}$ is the finesse of the cavity (Staley (2015)). Therefore, the higher the finesse of the cavity, the greater the phase shift, resulting in an amplified signal. In the LIGO detectors the Fabry–Perot cavities lead to a signal amplification by a factor $\sim$ 100 at 100 Hz. (Abbott *et al.* (2009a)).

4.1.1.2. Power recycling cavity. A partially reflecting mirror, called the power recycling mirror (PRM) is placed between the laser and the BS to reflect back the light returning to the main laser source. The recycled light resonates within the optical cavity formed between the PRM and the Michelson symmetric port. This configuration, known as a power recycled Fabry–Perot Michelson, leads to an increase in the power by a factor of $\sim$ 8000 with respect to a simple Michelson design (Abbott *et al.* (2009a)).

4.1.1.3. Signal recycling cavity. A signal recycling mirror (SRM) is located before the photodetector at the antisymmetric port to form a signal recycling cavity. This is designed to enhance the GW signals at the frequencies of scientific interest. The signal recycling cavity effectively reduces the finesse of the Fabry-Perot cavities without compromising the detector sensitivity, while enabling a broad detector bandwidth (Staley (2015)).

4.2. LIGO SENSITIVITY AND NOISE SOURCES

Advanced LIGO is designed to measure a GW strain as small as $4 \times 10^{-24}/\sqrt{\text{Hz}}$ at a frequency $\sim$ 100 Hz (Barsotti *et al.* (2018)). Figure 4.2 shows a comparison of the noise-equivalent strain sensitivity curve of Advanced LIGO for its various observing runs. During its O3 run, which started in April 2019 and ended in March 2020, Advanced LIGO had a strain sensitivity of $2 \times 10^{-23}/\sqrt{\text{Hz}}$ in the 200 – 1000 Hz region. Another way to describe the sensitivity of the LIGO detectors is by specifying the binary inspiral range (Abbott *et al.* (2015)). This range is the volume- and orientation-averaged distance to which

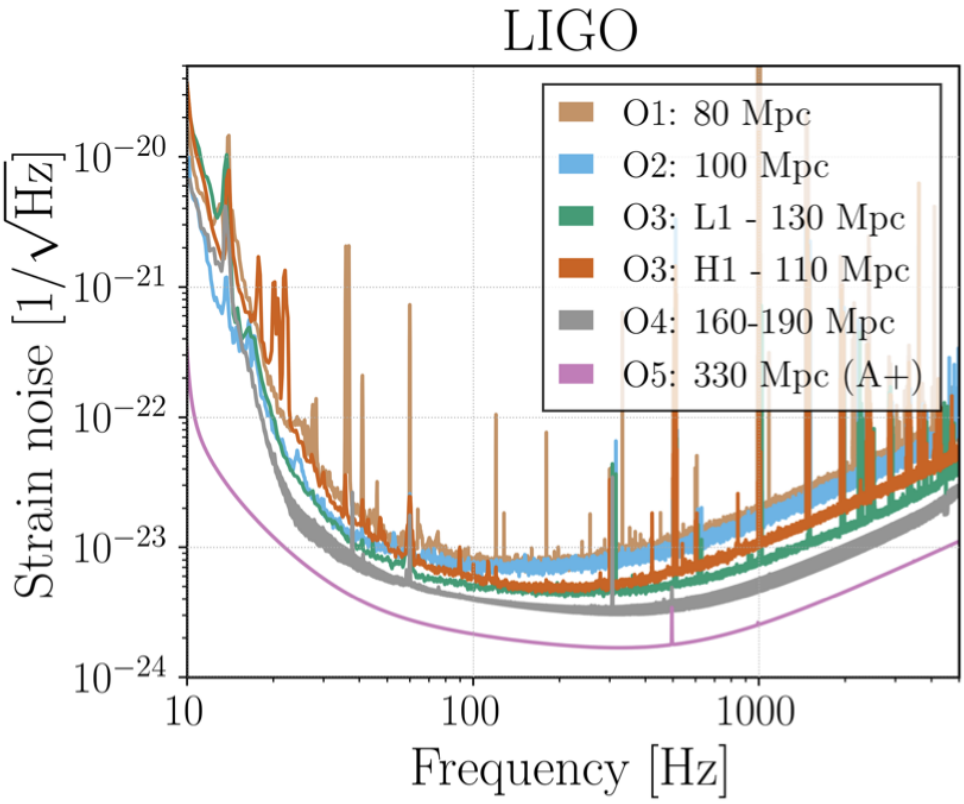

Figure 4.2. A comparison the sensitivity achieved or estimated to achieve by Advanced LIGO during its observing runs (Abbott *et al.* (2019a)).

the GW signal emitted by a binary neutron star (BNS) coalescence with component masses of $1.4M_{\odot}$ is detectable with a single detector SNR of 8. The BNS inspiral range of the Advanced LIGO detectors at design sensitivity is $\sim$ 200 Mpc. During the O3 run, the BNS inspiral range for the LIGO Hanford and Livingston sites was on average $\sim$ 115 Mpc and $\sim$ 135 Mpc, respectively.

There are various sources of noise that hinders LIGO from achieving its design sensitivity. The major sources of noise include seismic noise at low frequencies, Brownian noise at intermediate frequencies and quantum noise at low and high frequencies.

4.2.1. Seismic Noise. Seismic noise arises from ground motion that can couple to the suspended test masses. Seismometers are located throughout the interferometer to monitor the seismic motion near the test masses. Information from these seismometers are used to subtract the noise from the detector waveform. The test mass motion requirement is less than $10 \times 10^{-19}\,\mathrm{m}/\sqrt{\mathrm{Hz}}$ at 10 Hz whereas the nominal ground motion at 10 Hz is $\sim 10 \times 10^{-9}\,\mathrm{m}/\sqrt{\mathrm{Hz}}$ (D. V. Martynov *et al.* (2016)).

LIGO's ETMs and ITMs are suspended as quadruple pendula to isolate them from seismic noise. These stages are also shown in Figure 5.1. This configuration provides suppression of the horizontal motion as $1/f^{2n}$ for the n-th stage of the quadruple pendulum. Thus, at high frequencies, the mirrors can be considered as free-falling objects (Staley (2015)).

To further mitigate the effects of the seismic noise, LIGO employs active and passive feedback controls. The quadruple pendulum system is actually a pair of adjacent quadruple suspensions, with the *main chain* holding the suspended test mass, and the *reaction chain* suspending equally isolated masses upon which the actuators are mounted. Among the lowest three stages of each quadruple suspension, the upper intermediate (UIM), and penultimate (PUM) are driven by magnetic coil actuators. The lowest stage of the suspension, the test mass (TST) stage, is driven by an electrostatic actuator system.

4.2.2. Thermal or Brownian Noise. The thermal motion of the test masses can cause mirror displacements and is a source of noise. Low-loss coatings and high-Q materials are used to limit this thermal noise (Staley (2015)). The masses in the lower two stages of the quadruple pendulum (34 cm in diameter, 20 cm in thickness, and 40 kg of mass) are made of a high purity fused silica. They are suspended using fibers creating a monolithic suspension (Abbott *et al.* (2016b)). Thermal noise can also appear in the form of thermal aberrations. As the laser power is partially absorbed by the test masses, the deformations in

the mirrors can create higher order TEM modes (Staley (2015)). Advanced LIGO employs a thermal compensation system to heat up the test masses and reduce the mirror deformations in the region of the incident beam (Brooks *et al.* (2009)).

4.2.3. Quantum Radiation Pressure and Shot Noise. The quantum radiation pressure arises due to the quantum nature of the light in the low-frequency band 10 – 50 Hz (Pitkin *et al.* (2016)). This noise can be mitigated by decreasing the laser power and increasing the mass of the test masses. However, this leads to an increase of shot noise. Shot noise arise at the sensing or readout of the interferometer and limits the sensitivity at high frequencies (Matone (2012)).

4.3. LIGO AND GWS

This subsection describes the interaction of GWs with the LIGO detectors and the angular sensitivity of the detector to the GWs. The notations follow Maggiore (2008).

4.3.1. Interaction of GWs With Test Masses. As the GWs have a simple form in TT gauge, it is convenient to work in a coordinate system that satify this TT gauge. The geodesic equation of a test mass is given by

$$\frac{d^2x^\mu}{d\tau^2} + \Gamma^\mu_{\rho\sigma}\frac{dx^\rho}{d\tau}\frac{dx^\sigma}{d\tau} = 0\,, \tag{4.1}$$

where $\Gamma^\mu_{\rho\sigma}$ are the Christoffel symbols given by Equation (2.4) and τ is the proper time defined as the time measured by a clock carried along the time-like geodesics. If the test mass is at rest at $\tau = 0$, then the geodesic equation can be written as

$$\frac{d^2x^i}{d\tau^2}|_{\tau=0} = -\Gamma^i_{00}\left(\frac{dx^0}{d\tau}\right)^2\,. \tag{4.2}$$

Writing $g_{\mu\nu} = \eta_{\mu\nu} + h_{\mu\nu}$ and expanding to the first order in $h_{\mu\nu}$, Γ^i_{00} is given by

$$\Gamma^i_{00} = \frac{1}{2}(2\partial_0 h_{0i} - \partial_i h_{00}). \tag{4.3}$$

In a TT frame, the gauge conditions imply that $h_{0i} = 0$ and $h_{00} = 0$. Thus $\frac{d^2x^i}{d\tau^2}\,|_{\tau=0} = 0$. Test masses which are at rest initially remain at rest.

Consider two nearby geodesics, parametrized by $x^\mu(\tau)$ and $x^\mu(\tau) + \epsilon^\mu(\tau)$ respectively. If $|\epsilon^\mu(\tau)|$ is much smaller than the typical variation scale of the gravitational field, the equation of geodesic deviation at first order in ϵ is given by

$$\frac{d^2\epsilon^\mu}{d\tau^2} + 2\Gamma^\mu_{\rho\sigma}\frac{dx^\rho}{d\tau}\frac{d\epsilon^\sigma}{d\tau} + \epsilon^\alpha\partial_\alpha\Gamma^\mu_{\rho\sigma}\frac{dx^\rho}{d\tau}\frac{dx^\sigma}{d\tau} = 0\,. \tag{4.4}$$

Assuming $dx^i/d\tau = 0$ at $\tau = 0$ and given $dx^0/d\tau = c$, Equation (4.4) reduces to

$$\frac{d^2\epsilon^i}{d\tau^2}\,|_{\tau=0} = -\dot{h}_{ij}\frac{d\epsilon^i}{d\tau}\,|_{\tau=0}\ , \tag{4.5}$$

where we have used $\Gamma^i_{00} = 0$, $\Gamma^i_{0j} = (1/2)\partial_0 h_{ij}$ and that $\Gamma^i_{0\sigma}$ is non-zero only if σ is a spatial index. If $\frac{d\epsilon^i}{d\tau} = 0$ at $\tau = 0$ then the $\vec{\epsilon}$ remains constant at all times. This means that the coordinates of the test masses do not change.

Consider two events at $(t, x_1, 0, 0)$ and $(t, x_2, 0, 0)$, respectively. The coordinate distance between them, $(x_2 - x_1) = L$, remains constant in the TT gauge. However, for a GW propagating along the z-direction, the proper distance s between the two events is given at first order in h by

$$s = L\left[1 + \frac{1}{2}h_+ e^{ik^\sigma x_\sigma}\right]\,. \tag{4.6}$$

The proper distance changes periodically in time because of the GWs. If the spatial separation between the two events is given by a vector $\mathbf{L}$, the proper distance is given by $s^2 \approx L + h_{ij}L_iL_j$. At first order in h it follows,

$$\ddot{s} \sim \frac{1}{2}\ddot{h}_{ij}\frac{L_i}{L}L_j. \tag{4.7}$$

Since by definition $s = n_i s_i$, where $n_i = L_i/L$, the above equation can be rewritten as

$$\ddot{s}_i \sim \frac{1}{2}\ddot{h}_{ij} L_j \sim \frac{1}{2}\ddot{h}_{ij} s_j \,, \tag{4.8}$$

Equation (4.8) is the geodesic equation equation in terms of proper distance.

In the case of LIGO, the two test masses are the end mirrors. GWs affect the proper distance between these mirrors and can be detected by measuring the time that the light takes to complete a round-trip in the interferometer arms.

4.3.2. Interaction of GWs With LIGO Detectors. The test masses are at a distance much less than the reduced wavelength of the GW ($\lambda/2\pi$). Thus the displacement of the interferometric mirrors due to the stretching and squeezing of the spacetime can be described by the equation of geodesic deviation. The local spacetime metric can be considered to be flat with the origin of the coordinate system fixed on the BS. For a GW with plus polarization propagating perpendicularly towards the interferometer from the z - direction, the geodesic equation for the X-end mirror, is described in the coordinates (ξ_X, ξ_Y) by Equation (4.8)

$$\ddot{\xi_X} = \frac{1}{2}\ddot{h_+}\xi_X. \tag{4.9}$$

At zeroth order $\xi_X = L_X$, and the equation of geodesic deviation is given by $\ddot{\xi_X} = (1/2)\ddot{h_+}L_X$. The solution of the equation is

$$\xi_X = L_X + \frac{h_0 L_X}{2}\cos\left(\omega_{gw} t\right), \tag{4.10}$$

where $h_+ = h_0 \cos\left(\omega_{gw} t\right)$, ω_{gw} is the angular frequency of the GWs and h_0 is the amplitude of the GW at $t = 0$. The integration constants are chosen such that the average value of ξ_X over one GW period is L_X and the average value of $\dot{\xi}_X$ vanishes. Under these conditions and $\xi_Y(0) = \ddot{\xi}_Y = 0$, $\xi_Y(t) = 0$ at all times.

Since the local spacetime is flat, a photon starting at the BS at time t_0 and moving along the X-axis reaches the ETM at time $t_1 = t_0 + \xi_X(t)$. Since the photon follows the trajectory $x(t) = c(t_1 - t_0)$, at zeroth order in h_0, $t_1 = t_0 + L_X/c$. Therefore Equation (4.10) is given by

$$c(t_1 - t_0) = L_X + \frac{h_0 L_X}{2} \cos\big(\omega_{gw}(t_0 + L_X/c)\big). \tag{4.11}$$

The round-trip time Δt that a photon takes to get back to the BS is twice the time $t_1 - t_0$. Thus

$$\Delta t = \frac{2L_X}{c} + \frac{h_0 L_X}{c} \cos\big(\omega_{gw}(t_0 + L_X/c)\big)\,. \tag{4.12}$$

The first term in the r.h.s is the photon round trip time in the absence of the GW. The second term is the variation in propagation time due to its interaction with the GW along the X-arm:

$$\delta\tau_X = \frac{h_0 L_X}{c} \cos\big(\omega_{gw}(t_0 + L_X/c)\big)\,. \tag{4.13}$$

The light traveling in the Y-arm will also acquire the same amount of perturbation but in the opposite direction. Thus the total travel time difference due to the interaction of the light with the GW along the two arms of the interferometer is given by $\delta\tau_X + \delta\tau_Y$. If the average length of the two arms of the interferometer is the same, i.e. $L_X = L_Y = L$, then the variation in the propagation time is

$$\Delta\tau = \frac{\Delta L}{c} = \frac{2Lh_0 \cos\big(\omega_{gw}(t - L/c)\big)}{c}\,, \tag{4.14}$$

where $\Delta L = \Delta L_X - \Delta L_Y$. ΔL_X and ΔL_Y are the arm length variation along the X- and Y-arm of the interferometer, respectively. The above equation can be rewritten as a phase shift between the lights in the two arms

$$\begin{aligned} \Delta\phi(t) = \frac{4\pi\Delta L}{\lambda} &= \frac{4\pi L h_0 \cos\big(\omega_{gw}(t - L/c)\big)}{\lambda}\,, \\ &= \frac{4\pi L h_+(t - L/c)}{\lambda}. \end{aligned} \tag{4.15}$$

The phase shift is directly proportional to the amplitude of the GW and the length of the interferometer arm. The strain produced by the gravitational wave is $h_+ \approx \Delta L/L$. Therefore, larger the interferometers arms smaller the GW strain can be detected.

4.3.3. Antenna Pattern. For a detector sensitive to GWs with wavelengths much larger than its size, such that $\hat{n} \cdot \mathbf{x}/\lambda \ll 1$ over the whole detector, we can neglect the spatial dependence of $h_{ij}(t, \mathbf{x})$. When a GW impinges on such a detector, the GW amplitude can be as

$$h_{ij}(t) = \sum_{P=+,\times} A_{ij}^{P}(\hat{n}) h_P(t)\,, \tag{4.16}$$

where $A_{ij}^{P}(\hat{n})$ is the polarization tensor introduced in Equation (2.26) and h_P is one of the h_+ and $h_\times$ amplitude.

Since the output of the GW detector is a timeseries, the input of the detector can be written as $h(t) = D^{ij} h_{ij}(t)$, where D^{ij} is a constant tensor that depends on the geometry of the detector and is known as the detector tensor. Using Equation (4.16), the scalar output of the detector can be written as

$$h(t) = \sum_{P=+,x} D^{ij} A_{ij}^{P}(\hat{n}) h_P(t). \tag{4.17}$$

Defining the detector pattern function as

$$F_P(\hat{n}) = D^{ij} A_{ij}^{P}(\hat{n})\,, \tag{4.18}$$

Equation (4.17) can be rewritten as

$$h(t) = F_+(\theta, \phi) h_+(t) + F_\times(\theta, \phi) h_\times(t)\,, \tag{4.19}$$

where $\hat{n}$ is the direction of propagation of the GW.

The response of the detector to a GW with arbitrary direction of propagation and arbitrary polarization is encoded in detector pattern functions. In the long-wavelength approximation limit, where $\omega_{gw}L/c \ll 1$, for mirrors located at (L,0,0) and (0,L,0), the displacements along the X- and Y-direction are

$$\ddot{\xi}_X = \frac{1}{2}\ddot{h}_{XX}L\,, \tag{4.20a}$$

$$\ddot{\xi}_Y = \frac{1}{2}\ddot{h}_{YY}L\,. \tag{4.20b}$$

The relative phase shift between the X and Y arms is given by $(\ddot{h}_{XX} - \ddot{h}_{YY})/2$ since the motions of the mirrors are governed by the geodesic equation. The detector tensor for the interferometer is $D^{ij} = (\hat{x}_i\hat{x}_j - \hat{y}_i\hat{y}_j)/2$ and the detector output will be $h(t) = (h_{XX} - h_{YY})/2$.

Introducing as in Subsection 2.2, the frame S' with the GW propagating along the z' direction, the GW amplitude in the S' frame is

$$h'_{ij} = \begin{pmatrix} h_+ & h_\times & 0 \\ h_\times & -h_+ & 0 \\ 0 & 0 & 0 \end{pmatrix}_{ij}\,. \tag{4.21}$$

The matrix that transforms S' frame into the S frame is given by the rotation matrix

$$R = \begin{pmatrix} \cos\phi & \sin\phi & 0 \\ -\sin\phi & \cos\phi & 0 \\ 0 & 0 & 1 \end{pmatrix}\begin{pmatrix} \cos\theta & 0 & \sin\theta \\ 0 & 1 & 0 \\ -\sin\theta & 0 & \cos\theta \end{pmatrix}, \tag{4.22}$$

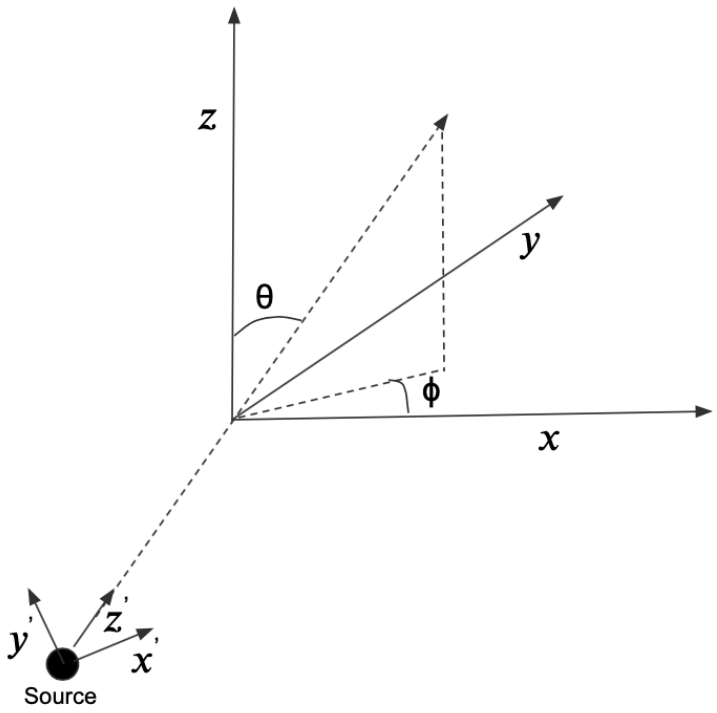

Figure 4.3. Geometry used in calculating the detector antenna pattern. The S' frame is the source frame in which the GWs propagate along the z' direction. S frame is the detector frame. The rotation that brings S' frame to S frame, is rotation by an angle θ around y-axis followed by a rotation by angle ϕ around z axis.

where the polar angles θ and ϕ are defined as in Figure 4.3. The GW in the S frame is given by $h_{ij} = R_{ik}R_{jl}h'_{kl}$, i.e.,

$$h_{xx} = h_{+}(\cos^2\theta\cos^2\phi - \sin^2\phi) + 2h_{\times}(\cos\theta\cos\phi\sin\phi)\,, \tag{4.23a}$$

$$h_{yy} = h_{+}(\cos^2\theta\sin^2\phi - \cos^2\phi) - 2h_{\times}(\cos\theta\cos\phi\sin\phi)\,. \tag{4.23b}$$

Thus the output of the interferometer is given by

$$h(t) = \frac{1}{2}h_{+}(1+\cos^2\theta)\cos 2\phi + h_{\times}(\cos\theta\sin 2\phi)\,. \tag{4.24}$$

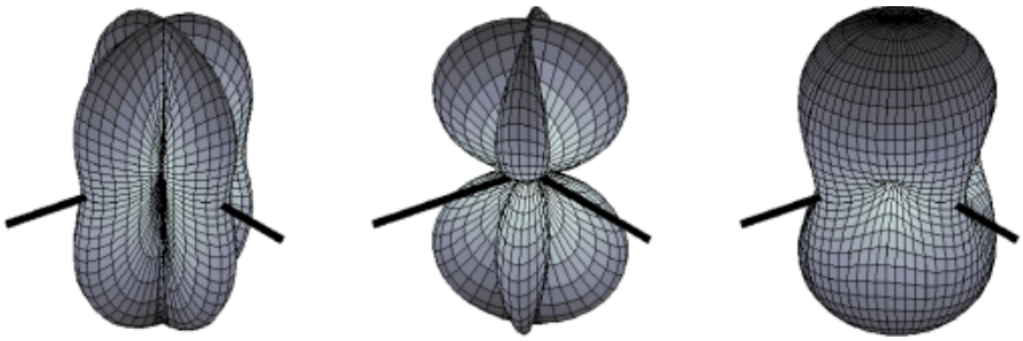

Figure 4.4. Antenna patterns for a single LIGO detector under the long-wavelength approximation for the plus polarization (left), the cross polarization (center) and the root mean squared antenna pattern (right). The BS is located at the center of each pattern and the interferometer arms denoted by the black lines.

Comparing the above equation with Equation (4.19) the antenna factors can be written as

$$F_+(\theta,\phi) = \frac{1}{2}(1+\cos^2\theta)\cos 2\phi\,, \tag{4.25a}$$

$$F_\times(\theta,\phi) = \cos\theta \sin 2\phi\,. \tag{4.25b}$$

Note that Equation (4.25) has been obtained under the long-wavelength approximation. From Equation (4.25), it can be seen that the detector has blind spots. For example, for a GW with plus polarization, the area of the sky defined by $\phi = \pi/4$ is a blind direction. This occurs because the GW produces the same displacement in X and Y-arm, so the relative phase shift is zero. Figure (4.4) shows the plus and cross antenna patterns along with the root mean squared antenna pattern for a single LIGO detector.

In summary, GW detectors are not omnidirectional, but exhibit directional variations in sensitivity.

The generalized antenna pattern for a network of N detectors, F_N, under the assumption that the detector noise streams are uncorrelated, is given by

$$F_N = \sqrt{\sum_k (F_{+,k}^2 + F_{\times,k}^2)}\,, \tag{4.26}$$

where $F_{+,k}$ and $F_{\times,k}$ are the detector pattern functions of the k-th detector (Schutz (2011)).

Co-aligned detectors can miss events that could be detected if the detectors were misaligned (Schutz (2011)). For example, the orientation of the Livingston and Hanford detectors with respect to each other implies there are four low sensitivity spots, see left panel of Figure 4.5.

Relative alignment of the detectors is crucial when searching for GW signals, especially the SGWB. The ability to determine polarization and sky position of a burst-like signal is also affected by the relative alignment of the detectors (Schutz (2011)). Adding more detectors with misaligned antenna patterns enables more accurate sky localizations from time-delay triangulation. For example, addition of Virgo to the LIGO network, the right panel of Figure 4.5, increases the sensitivity in LIGO's blind spots, which allows better detection and sky localization of the source.

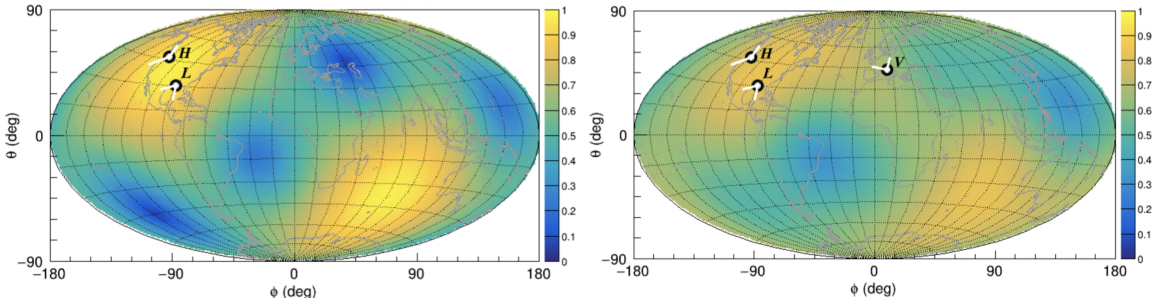

Figure 4.5. *Left*: Network antenna pattern for LIGO-Livingston and LIGO-Hanford detectors (LH). *Right*: Network antenna pattern for LIGO-Virgo detectors (LHV).

Section 8 provides a more detailed discussion on the importance of accurate sky localization, specially for multi-messenger astronomy. The next section discusses how the LIGO detectors are calibrated to extract accurate source information from the GW signals.

5. LIGO CALIBRATION

Calibration of the GW detector requires conversion of digital counts read by the photodetector at the output of the interferometer into a dimensionless strain, h. This calibrated strain data is then analyzed to determine the presence of a GW signal in the data and to extract astrophysical information about the source from it.

5.1. MOTIVATION FOR ACCURATE AND PRECISE DETECTOR CALIBRATION

Detected GW signals have been used to understand the evolution of binary mergers (Abbott *et al.* (2017a)), check the validity of equation of state models of NSs (Radice *et al.* (2018)), estimate the values of cosmological parameters (Abbott *et al.* (2019d)), test alternative theories of relativity (Abbott *et al.* (2019f)) and measure the speed of GW propagation (Vitale *et al.* (2012b)).

In 2009, it was estimated that a calibration accuracy of 0.5 % or better would be required to optimally extract information from the GW signals (Lindblom (2009)). Subsequent analyses have also highlighted the importance of reducing calibration uncertainties (Abbott *et al.* (2016a); Vitale *et al.* (2012a)). Accurate determination of the distance to GW sources requires low overall network calibration uncertainty. Also, precise relative calibration between the detectors is necessary for accurate sky localization of sources (Fairhurst (2009)) and to enable follow-up observations by EM observatories.

In O3, the estimated calibration accuracy was at the 2 % level (Sun *et al.* (2020)). This was typically considered to be sufficient for source parameter estimation of single events. However, calibration accuracy may become the limiting factor for statistically based investigations that use a set of events, such as the determination of the Hubble parameter. In 2017, the LIGO and Virgo collaborations reported the observation of a BNS inspiral (Abbott *et al.* (2017c)). While the LIGO-Virgo observation provided information on the distance of

the event, follow-up observations of an EM counterpart at multiple wavelengths by over 70 EM observatories provided information on the redshift of the host galaxy, thus enabling the estimation of the Hubble parameter, $H_0 = 70.0^{+12.0}_{-8.0}$ Km/s/Mpc (Abbott *et al.* (2019d)).

The observations of GW170817 by the LIGO and Virgo network, together with the kilonova AT2017gfo (cite) and the gamma-ray burst GRB170817A (Abbott *et al.* (2021h)), served as the first demonstration of the bright siren approach. This result was constrained by the SNR rather than calibration accuracy. In fact, a recent study by Huang *et al.* (In preparation) shows that the 90 % confidence interval for the H_0 posterior includes the true value of H_0 even in the presence of systematic calibration errors as large as $2 - 3$ % in the detectors' most sensitive frequency band.

The H_0 estimate with GW150914 lies mid-way between the results reported by *Planck* (Aghanim *et al.* (2018)) ($H_0 = 67.8 \pm 0.9$ Km/s/Mpc) and the *SHoES* (Riess *et al.* (2016)) collaboration ($H_0 = 73.24 \pm 1.74$ Km/s/Mpc). To resolve this tension, the Hubble parameter will need to be measured with a ~ 1 % accuracy (Chen *et al.* (2018)). This will require a GW detector calibration accuracy of 1 % or better, i.e., an accuracy of the fiducial length variation calibration at sub-percent level. The various techniques for generating accurate and precise fiducial length variation calibration are briefly discussed in the Section 5.3.

5.2. INTERFEROMETER CALIBRATION

Calibration of a ground-based GW detector is achieved using an accurate and precise model of the detector's response to the differential arm length variations. In this subsection, we discuss how to model the detector's response to these variations. The following discussion is mostly based on Sun *et al.* (2020) including D.Bhattacharjee and Sun *et al.* (2021) including D.Bhattacharjee.

The detectors measure the dimensionless strain h. The latter is proportional to the DARM length changes ΔL_{free}:

$$h = \frac{\Delta L_{free}}{L} = \frac{L_X - L_Y}{L}\,, \tag{5.1}$$

where L_X and L_Y are the displacements in the two perpendicular arms X and Y, respectively and L is the average arm length of the detector. To maintain the optical cavities on resonance condition, ΔL_{free} is calculated using the error and control signals of a DARM control loop rather than being directly measured (Abbott *et al.* (2017b); Cahillane *et al.* (2017)).

The interferometer response function is used suppress the DARM length variation and reconstruct thee strain from the residual displacement ΔL_{res}. A reasonably accurate estimate of the strain is generated almost in real-time for quick EM follow-up. These low-latency estimate is produced from a model in two steps. First, a crude "front-end" production of ΔL_{free} is obtained with large systematic errors, through a simple model. In the second step", a low-latency ($\sim$ 10sec) "online" estimate of the strain is generated using the best models of the detector response with lower systematic error. A final more accurate estimate of the calibrated strain is generated "offline" with latency of few months if needed. The following subsections provide a brief description of the different steps involved in the interferometer calibration process. A more detailed description can be found in (Cahillane *et al.* (2017); Sun *et al.* (2020)).

5.2.1. DARM Loop. The DARM loop consists of the interferometer, analog electronics, analog-to-digital converters, "front-end" computers, and digital-to-analog converters. A schematic diagram of the DARM loop is shown in Figure 5.1. The residual DARM length variation, ΔL_{res}, is converted to a digital error signal d_{err} by a sensing function C. The error signal is filtered by a set of digital filters, D, to produce a digital control signal, d_{ctrl}. The actuation function, A, converts d_{ctrl} to the displacement ΔL_{ctrl}, which suppress ΔL_{free}, caused by either noise or the GWs, thus keeping the optical cavities in resonance.

There remains a small residual ΔL_{res} in the DARM loop. Thus, ΔL_{free} is given by the sensing and the actuation function models according to

$$\Delta L_{free} = \Delta L_{res} + \Delta L_{ctrl} = \frac{1}{C^m} * d_{err} + A^m * d_{ctrl}\,, \tag{5.2}$$

where the superscript m denotes the models for the functions. The symbol $*$ denotes convolution in the time domain and multiplication in the frequency domain. As mentioned before, the error signal is converted to digital control signal using the digital filters $D = d_{ctrl}/d_{err}$, which are known to negligible uncertainty. Therefore, for a DARM open loop gain of $G^m = A^m * D * C^m$, Equation (5.2) can be rewritten as

$$\Delta L_{free} = \frac{1 + A^m * D * C^m}{C^m} * d_{err} = \frac{1 + G^m}{C^m} * d_{err}\,. \tag{5.3}$$

Combining Equation (5.1) and Equation (5.3), the calibrated strain can be expressed as

$$\begin{aligned} h = \frac{\Delta L_{free}}{L} &= \frac{1 + G^m}{C^m} * \frac{d_{err}}{L} \\ &= \frac{R^m * d_{err}}{L}\,, \end{aligned} \tag{5.4}$$

where the model DARM loop response function R^m is given by

$$R^m = \frac{1 + G^m}{C^m} = \frac{1 + A^m * D * C^m}{C^m}\,. \tag{5.5}$$

In the frequency domain, the response function error δR is equivalent to the GW strain data error and the response function uncertainty σ_R is equivalent to the GW strain data uncertainty.

The DARM loop transfer functions C and A are measured and modeled in the frequency domain. The values of C and A can drift slowly over time, thus they are both frequency and time dependent, $C(f,t)$ and $A(f,t)$. The online calibration model functions $1/C^m$ and A^m do not fully capture all the complexities of the LIGO interferometer. This

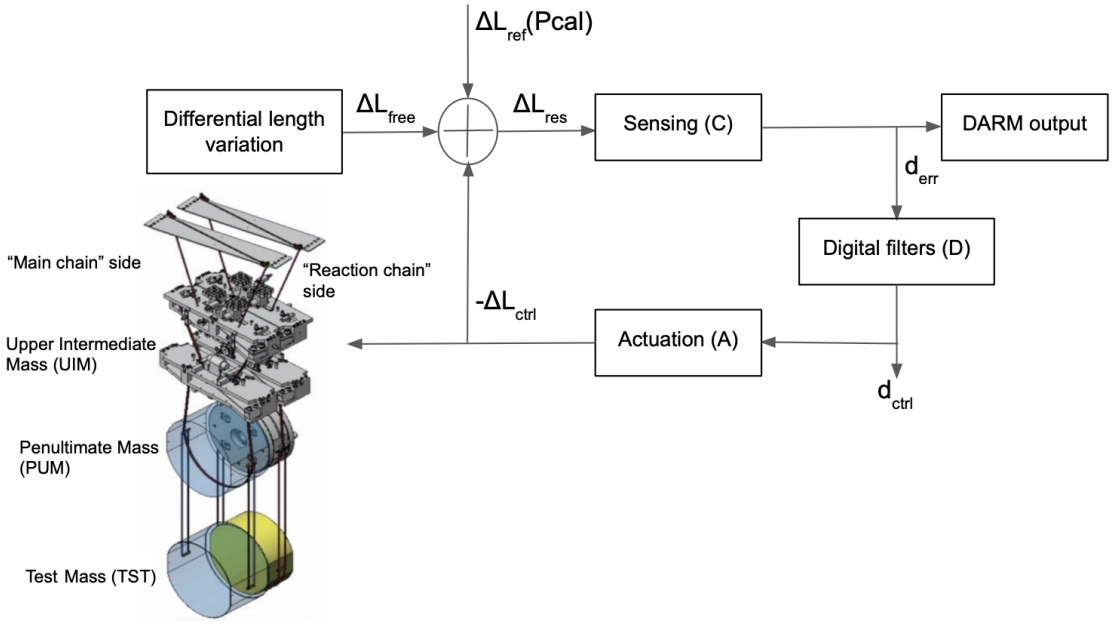

Figure 5.1. Schematic diagram of the differential arm length (DARM) feedback control loop. The sensing function, C, produces the DARM output signal, which is filtered using digital filters, D, known to negligible uncertainty. The actuation function, A, then uses the digitized control signal to move the test mass, suspended as a quadruple pendulum, to hold the interferometer resonance condition. The lower three stages UIM, PUM and the TST masses, are shown in the figure.

leads to known systematic errors in the reconstruction of $h(t)$, determined by the sensing and actuation systematic errors $\delta C(f,t)$ and $\delta A(f,t)$, respectively.

$$\frac{\delta C(f,t)}{C^m} = \frac{C(f,t)}{C^m} - 1\,, \tag{5.6a}$$

$$\frac{\delta A(f,t)}{A^m} = \frac{A(f,t)}{A^m} - 1\,, \tag{5.6b}$$

where $C(f,t)$ and $A(f,t)$ are the measured sensing and actuation transfer functions. Similarly, the systematic error for the response function model R^m is given by

$$\begin{aligned}\frac{\delta R(f,t)}{R^m} &= \frac{R(f,t)}{R^m} - 1 \\ &= \frac{1}{1+G^m}\left[G^m\frac{\delta A(f,t)}{A^m} - \frac{\delta C(f,t)/C^m}{1+\delta C(f,t)/C^m}\right],\end{aligned} \tag{5.7}$$

where $R(f,t)$ is the measured response function.

The uncertainty on the sensing and actuation functions, σ_C and σ_A, propagate to the relative response function uncertainty σ_R/R^m as

$$\begin{aligned}\frac{\sigma_R}{R^m} &= \frac{1}{R^m}\sqrt{\left(\frac{\partial R}{\partial C}\right)^2\sigma_C^2 + \left(\frac{\partial R}{\partial A}\right)^2\sigma_A^2} \\ &= \frac{C^m}{1+G^m}\sqrt{\frac{1}{C^4(f,t)}\sigma_C^2 + D^2(f)\sigma_A^2}\,.\end{aligned} \tag{5.8}$$

Together $\delta R/R^m$ and σ_R/R^m provide the entire calibration error and uncertainty budget.

5.2.2. Sensing and Actuation Function Models. From Equation (5.5) one can see that the sensing and actuation function reference models are required to construct the model DARM loop response function R^m. This subsection describes the various components and parameters of the sensing and actuation function models.

The sensing function model, C^m, accounts for the interferometric transfer function from DARM displacement to the laser power on the photodetector at the antisymmetric port, the response of the photodiodes and their analog readout electronics, and the effects from the digitization process. The Advanced LIGO detectors operate in a configuration where the SRM is detuned from the resonance condition to increase the bandwidth of the detector. When the mirrors are detuned to exactly 90 degrees, the sensing model can be approximated as a single pole system. An optical spring response is created by any detuning present between the signal recycling cavity and the arm cavities. If f_s and Q_s are the optical spring pole frequency and the quality factor, respectively, the sensing function model in the

frequency domain is given by

$$C^m(f) = \kappa_C(t)\left(\frac{H_C}{1 + if f_{cc}^{-1}}\right)\left(\frac{f^2}{f^2 + f_s^2 - if f_s Q_s^{-1}}\right) C_R(f) exp(-2\pi i f \tau_C). \tag{5.9}$$

Here H_C is the combined gain of the interferometric response and the analog-to-digital converter (ADC), which gives the digital counts produced in d_{err} in response to differential arm length displacement. The differential coupled-cavity pole frequency, f_{cc}, is the characteristic frequency defining the detector bandwidth. The time delay τ_C, which is $\sim 77.6\,\mu s$ for both the detectors, includes the light travel time along the length of the arms, computational delay in the digital data acquisition (DAQ) system, and the delay introduced due to the single pole approximation. The dimensionless quantity $C_R(f)$ accounts for additional collective frequency dependencies of the DAQ system, which are known to negligible uncertainty. The parameters $H_C,\ f_{cc},\ f_s$ and Q_s fluctuate on a time-scale of minutes due to the variations of optical alignment in the arm cavities, the relative alignment between the arm cavities and the SRC, and the laser power. The scale factor characterizing the frequency independent variations in H_C is defined as $\kappa_C(t)$.

The actuation function is the response of the control DARM displacement to the digital control signal. ΔL_{ctrl} may be induced by actuating on any one of the four stages of the quadruple pendulum systems on any of the four arm cavity optics (the two ITMs and the two ETMs). As shown in Figure 5.1, the quadruple pendulum system is actually comprises the main chain holding the suspended test mass, and the reaction chain upon which the actuators are mounted. To estimate the displacement of the test mass, only the response on the main chain is modeled to avoid the added complexity due to the reaction chain.

The total actuation model at a given time can be described by the sum of the paths the digital control signal takes through each stage to displace the TST:

$$A^m(f) = [\kappa_U(t)F_U(f)H_U A_U(f)exp(-2\pi i f\tau_U)] + [\kappa_P(t)F_P(f)H_P A_P(f)exp(-2\pi i f\tau_P)] + [\kappa_T(t)F_T(f)H_T A_T(f)exp(-2\pi i f\tau_T)] \ , \tag{5.10}$$

where U, P, and T represent the UIM, PUM, and TST stages, respectively. The functions $A_i(f)$ and H_i are the gain and the normalized frequency response of the i-th suspension stage actuator, defining the actuation transfer function for each suspension stage ($i = U, P, T$). The function $F_i(f)$ is the digital frequency-dependent filter function, and τ_i is the total time delay in the digital-to-analog conversion. The H_i are slowly varying over time due to various physical mechanisms. For example, the overall strength of the TST electrostatic actuator changes slowly on a time-scale of days to weeks due to the slow accumulation of static charges around the test masses and reaction masses. The overall strengths of the UIM and PUM magnetic coil actuators are expected to be static in time, but occasional changes in actuator electronics path often require compensation.

The $\kappa_i(t)$ are dimensionless time-dependent complex scale factors for the i-th stage accounting for variations in H_i. These time-dependent parameters, $\kappa_C(t)$, $f_{cc}(t)$, $f_s(t)$, $Q(t)$, and $\kappa_i(t)$ are collectively referred to as time-dependent correction factors (TDCFs). Additional details can be found in Sun *et al.* (2020).

5.2.3. Model Parameter Estimation and Interferometer Measurement. The parameter vectors $\lambda^C = [H_C, f_{cc}, f_s, Q, \tau_C]$ and $\lambda^A = [H_i, \tau_i]$ define a set of time-independent, reference sensing and actuation parameters whose values are fit to non-negligible precision. Thus the sensing function $C^m(f, t, \lambda^C)$ and the actuation function $A^m(f, t, \lambda^A) = [H_i, \tau_i]$ models for the i-th stage actuator are approximated. The reference parameters in λ^C and $\vec{\lambda}^A$ are determined from measurements using a Markov Chain Monte Carlo (MCMC) fitting algorithm. The maximum a posteriori (MAP) values, λ^C_{MAP} and

λ^A_{MAP} from the MCMC fitting are used to create the DARM response model. Equation (5.5) for R^m is rewritten in the frequency domain as

$$R^m(f) = \frac{1}{C^m(\vec{\lambda}^C_{MAP}; f)} + A^m(\vec{\lambda}^A_{MAP}; f))D(f)\,. \tag{5.11}$$

Any physical change in the interferometer that is too large to be accounted for by the TDCFs requires a new calibration *epoch*. If one or more parameters from the existing epoch $\vec{\lambda}^C_{MAP}$ and $\vec{\lambda}^A_{MAP}$ are no longer valid, the MCMC parameter estimation process is repeated using new measurements of sensing and actuation functions to create an updated reference model.

A fiducial displacement of the ETM is required to measure the detector's response to the DARM motion, i.e., to calibrate the detector. The DARM model transfer functions $C(f,t)$ and $A(f,t)$ of each of the actuation stages are measured by performing sweep sine transfer function measurements of the DARM control loop. A swept sine transfer function is a collection of single frequency, sequential excitations of the ETM across the relevant frequency band of the detector. A sensing function measurement is made by comparing $d_{err}(f)$ to a reference length variation, ΔL_{ref}, and then compensating for the suppression caused by the differential arm length (DARM) feedback control loop shown in Figure 5.1. The measured interferometer sensing function is given by

$$C(f) = \frac{d_{err}(f)}{\Delta L_{ref}(f)}\,[1 + G(f)]\,, \tag{5.12}$$

where $G(f)$ is the open loop transfer function measured separately using the in-loop suspension actuators. Measurements of the sensing function and the open-loop transfer function are taken sufficiently close in time such that any time dependencies of the sensing and actuation functions can be ignored. For frequencies above 1 kHz, the open-loop gain is negligible and the sensing function is well approximated by $C = d_{err}/\Delta L_{ref}$.

The actuation function measurement for the i-th stage is realized by first measuring the ratio of the error signal to amplitude of the excitations induced using the actuators on each stage of the quadruple pendulum, ΔL_i:

$$\frac{d_{err}}{\Delta L_i} = \frac{A_i(f)C(f)}{1 + G(f)} \,. \tag{5.13}$$

A second measurement is made by comparing $d_{err}(f)$, to ΔL_{ref} at the same frequencies as the actuation stage transfer function measurement.

$$\frac{d_{err}}{\Delta L_{ref}} = \frac{C(f)}{1 + G(f)} \,. \tag{5.14}$$

The two measurements are taken within a few minutes of each other so that the response of the interferometer does not change over time and one measurement does not corrupt the other. Combining the two measurements, the actuation function for the i-th stage of the quadruple pendulum is

$$A_i(f) = \left(\frac{d_{err}}{\Delta L_i(f)}\right)\left(\frac{\Delta L_{ref}(f)}{d_{err}}\right) \,. \tag{5.15}$$

Finally, the complete response of the detector to GWs is estimated by measuring the DARM loop error signal d_{err} in the presence of a reference actuator excitation, ΔL_{ref}:

$$\frac{d_{err}}{\Delta L_{ref}} = \frac{1}{R} \,, \tag{5.16}$$

where R is the measured response function of the detector.

The combined systematic error and the uncertainty in the detector's response function at a given time t are numerically estimated by constructing thousands of response functions, $R_j(f;t)$, where j indexes each response function and all draws associated with it. The j-th sensing and actuation functions are constructed using Equation (5.9) and Equation (5.10), with the j-th draw from the MCMC posterior distributions of the reference model parameters. TDCFs at time t are applied. Each $R_j(f;t)$ is divided by

$R^m(f;t)$ given by Equation (5.11) to create the probability distribution of the residual $\eta_R(f;t) = [R_j(f;t)/R^m(f;t)] - 1$. At any given time t and frequency f, the 50-th percentile value (the median) of the distribution $\eta_R(f;t)$ represents the total systematic error in $R^m(f;t)$. The 16-th and 84-th percentiles represent the lower and upper bounds, respectively, of the combined systematic error and $1-\sigma$ statistical uncertainty in $R^m(f;t)$. These percentiles represent the overall uncertainty and systematic error bounds of the reconstructed strain, h, at time t.

In O3, the systematic error in the detection frequency band $20-2000$ Hz was at levels of less than 2% in magnitude and less than 2 deg in phase, see Figure 5.2. In the LVK searches for astrophysical signals, the offline calibrated data and the 68 % percentile curve, (the central curve in Figure 5.2) are used as representatives of the uncertainty and systematic error estimates for the entire duration of search.

As LIGO and Virgo detectors improve their sensitivity and as the third-generation GW detectors with much higher sensitivity come online, improving current calibration methods to keep pace with greater number of detections with higher SNR may become challenging. Alternatively, calibration of the detector using the properties of the detected astrophysical signals have been suggested but this requires that the SNR of the detected signal be very high. However, the detected signals are comparatively weak. Only the signals above a threshold SNR at frequencies where the signals are strongest can be used (Pitkin *et al.* (2011)) , but it makes it difficult to attain the accuracy level enabled by the current calibration methods. According to another study by Schutz and Sathyaprakash (2020), in principle detector calibration at sub-1% accuracy level can be achieved using joint data streams with only calibration errors called the null streams from a network of three or more detectors. It uses an ensemble of all detected signals, not just the loud ones, in the framework of coherent detections to extract calibration errors of all detectors. However, an

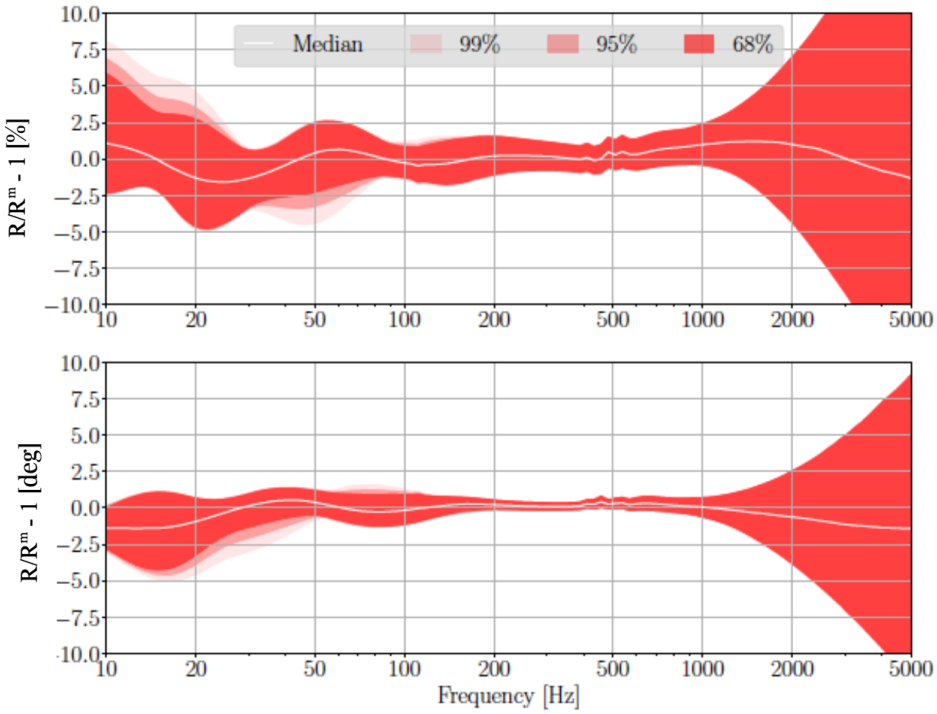

Figure 5.2. Combined frequency dependent systematic error and uncertainty in LIGO Hanford's (LHO) response function during "epoch" 1, which lasted from March 28, 2019 to June 11, 2019. The central line represents the estimated systematic error with respect to the interferometer response model and the color band represents $1-\sigma$ uncertainties for 68 %, 95 %, and 99 % of the run time. (Figure credit: Sun *et al.* (2020))

overall error in absolute calibration shared by all detectors in the network get canceled out in the null stream, and thus needs to be supplemented by some other method for at least one detector at a single frequency.

The astrophysical calibration and/or self calibration may become the optimal method of calibrating the detector, when it reaches the design sensitivity of the future generation of GW detectors. But these methods are not viable to provide the calibration accuracy level of the existing technique for the current network ground-based GW detectors.

5.3. ABSOLUTE REFERENCE LENGTH VARIATIONS

The following subsections provide a brief overview of the different techniques that have been applied in the past or are currently being used for generation of the fiducial length variations.

5.3.1. Free Swinging Michelson Method. The Free Swinging Michelson method (FSM) uses the interferometer laser wavelength as a length reference to calibrate the ETM actuation function. It relies on the measurement of interference fringes when the ETMs are misaligned but the ITMs and the BS are aligned to form a simple, *short* Michelson interferometer. The length control servo electronics are configured to lock this setup in the destructive interference condition at the output photodetector. Transfer function measurements are made by actuating on the position of the ITM. Next, the suspended mirrors are allowed to swing freely as the Michelson length difference changes, causing the output to vary between the maximum (bright-fringe) and the minimum (dark-fringe) levels. Thus the difference between the maximum and minimum values corresponds to relative ITM motion of $\lambda/4$, yielding an output signal calibration in nm/count. Combining this result with the transfer functions from the ITM actuation yields a calibrated actuation function for the ITM. The next step in the process is to misalign one of the ITMs and realign the ETM on the opposite arm. The servo electronics are then configured to feed back to the position of the ETM forming a resonant Fabry-Perot arm cavity, this is called a *single-arm* configuration. The ratio of ITM and ETM actuation along with the calibration of the ITM actuation functions yield the ETM actuation function. Similar measurements with the other interferometer arm cavity aligned provide the calibrated actuation function for the other ETM.

The measurements performed in the single-arm configuration require the actuation path electronics to be in *acquire*-mode rather than the nominal *run*-mode used for GW searches. In acquire mode the electronic noise-induced ETM displacement is 3-4 orders of magnitude higher than in run-mode. Propagating the calibration performed in the FSM

method to the interferometer configuration operating in run-mode requires correcting for the differences between the acquire-mode and run-mode actuation paths. Moreover, combining electronic transfer functions measured for various configurations and components with overall precision approaching 1 % proves to be a difficult task. This method is described in detail in (Goetz *et al.* (2010)).

5.3.2. Frequency Modulation Method. The frequency modulation method is a force-free technique to calibrate the ETM actuation. The interferometer is operated in a single-arm configuration. A sinusoidal modulation of the laser frequency is sensed as a length modulation by the arm cavity (Rakhmanov *et al.* (2002)). The length modulation is induced using the test mass actuator at a frequency close to the laser frequency modulation. By comparing the two modulations, the test mass actuator strength is calibrated. A more detailed description of this method can be found in (Goetz *et al.* (2010)). In addition to calibrating the ETM actuation, this method has been used to investigate systematic errors associated with other calibration techniques (Goetz and Savage (2010)).

The advantage of this method over the FSM method is that it is not required to precisely compensate for the differences in the run-mode and acquire-mode electronic paths. Frequency modulation measurements involve long integration times at a single frequency with actuation electronics in the run mode. However, it uses a single-arm configuration rather than the full science-mode configuration in which searches for GWs are performed. Another advantage is that, there are no localized forces on the test mass which can cause elastic deformation of the mirror surface, a dominant source of systematic error for other calibration methods, for example the photon calibrators described in the next subsection.

5.3.3. Photon Calibrator. The photon calibrator (Pcal) involves applying periodic forces on the ETMs via radiation pressure using an auxiliary power-modulated laser. It causes an ETM displacement proportional to the power of the laser beam reflected from the suspended mirror. The advantages of employing Pcal systems for generation of displacement fiducials is that they can be operated while the interferometer is running in observation mode

and they provide continuous, real time calibration for the interferometer. Pcal systems can produce DARM displacements that are orders of magnitude above the ΔL_{free} noise floor across the sensitive frequency band of the interferometer. Currently, calibration lines at different frequencies are injected to monitor the various TDCFs using the Pcal systems (Tuyenbayev *et al.* (2017)). During the observation runs the Pcal systems were employed to generate fiducial displacements of the ETM in Advanced LIGO (D Bhattacharjee *et al.* (2021); Karki *et al.* (2016)), Advanced Virgo (Acernese *et al.* (2018)) and KAGRA (Chu (2018)). Pcals are also used to generate ΔL_{ref} mentioned in Subsection 5.2.3. This technique is described in detail in the next section.

5.3.4. Newtonian Calibrator. Another method for generating displacement fiducials that has been explored at both the Virgo (Estevez *et al.* (2021)) and KAGRA (Inoue *et al.* (2018)) observatories is the method of gravitational calibration. It is also currently being tested at LIGO (Ross *et al.* (2021)). A Newtonian calibrator (Ncal) or Gravity field calibrator generates a dynamic gravitational field when a rotor with both quadrupole and hexapole mass distribution is rotated at a given frequency f. A time-varying force is exerted on the test mass of the interferometer via rotors that have been designed to simultaneously inject forces at $2f$ and $3f$, thus generating a fiducial displacement of the test mass at the end station. The force produced by this rotor can be predicted to have less than 1 % relative uncertainty and is well-resolved in the readout of the detector (Ross *et al.* (2021)). It may provide an independent check of the existing reference length variation calibration system, the Pcals.

6. GENERATING FIDUCIAL DISPLACEMENTS USING PHOTON CALIBRATORS

Photon Calibrators (Pcals) are the primary tools used in second-generation GW detectors for absolute calibration of test mass displacement. They were first installed on the 10-m prototype detector at Glasgow, Scotland (Clubley *et al.* (2001)) and subsequently on the GEO600 detector in Hannover, Germany (Luck *et al.* (2010)). Pcal systems have undergone many developments and improvements over the past years within LIGO. Virgo installed a Pcal system during its first science run, but its main function was to check the sign of strain signal, h(t) and to cross-check the mirror actuation standard calibration (Accadia *et al.* (2016)). KAGRA has also installed Pcal systems based on the Advanced LIGO Pcal design (Chu (2018)). Pcals can operate even when the interferometer is observing, providing continuous calibration. This is a major advantage of using Pcal systems over other calibration techniques.

The first two Subsections 6.1 and 6.2 are mostly based on Karki *et al.* (2016). The rest of the section is based on the publication D Bhattacharjee *et al.* (2021).

6.1. WORKING PRINCIPLE OF PCALS

As mentioned in Subsection 5.3.3, Pcals rely on auxiliary power-modulated laser beams reflecting from the suspended ETM to generate fiducial displacements proportional to the modulated laser power. The periodic force exerted on the mirror is given by:

$$F(t) = \frac{dp}{dt} \tag{6.1}$$

where p is the recoil momentum of the photons.

A single photon carries a momentum of $p = h/\lambda$ where h is the Planck's constant and λ is the wavelength of the laser light, 1047 nm for LIGO Pcals. For a photon incident on the ETM at an angle θ and reflecting from the mirror surface, the momentum imparted on the mirror is given by

$$p = 2\cos\theta\frac{h}{\lambda}. \tag{6.2}$$

The factor 2 comes from the fact that the photon reflecting from the mirror imparts a momentum that is twice the normal component of the photon momentum.

With n photons per second impinging on the ETM,

$$\frac{dp}{dt} = 2n\cos\theta\frac{h}{\lambda} = 2\frac{\cos\theta}{c}\, n\, h\, \nu. \tag{6.3}$$

Equation (6.3) can be rewritten in terms of the power of the laser as

$$\frac{dp}{dt} = \frac{2\cos\theta}{c}P. \tag{6.4}$$

where $P = nhc/t$. For a power-modulated laser beam, power $P(t)$ can be written as

$$P(t) = P_0 + P_m \sin\omega t \tag{6.5}$$

where P_0 is the average power of the auxiliary laser, P_m is the modulated power amplitude and ω is the angular frequency of the modulation.

Thus, the Equation(6.1) can be rewritten as

$$F(t) = \frac{dp}{dt} = \frac{2\cos\theta}{c}(P_0 + P_m \sin\omega t). \tag{6.6}$$

Conversion of the periodic Pcal-induced forces to displacements requires the force-to-length transfer function of the suspended mirror, $S(\omega)$, in units of m/N.

In the frequency domain, the amplitude of the motion induced by the modulated laser power is given by

$$x(\omega) = \frac{2\cos\theta}{c} S(\omega) P_m(\omega). \tag{6.7}$$

where $P_m(\omega)$ is the modulated power reflected off the ETM and will henceforth be denoted as $P(\omega)$.

LIGO uses a two-beam configuration to minimize local elastic deformation of the ETM surface in the region sensed by the interferometer beam (Goetz *et al.* (2009); Hild *et al.* (2007)). Pcal forces also induce bulk elastic deformation of the mirrors and is a prominent effect at high frequencies (1 kHz and above), which can result in large calibration errors. To minimize the effects of bulk deformation of the test mass, the Pcal beams are located near the nodal circle of "drumhead" vibrational mode. The two-beam configuration effectively excites the "butterfly" vibrational mode of the test mass. To minimize the butterfly mode, the interferometer beam is nominally positioned at the center of the optic (Karki (2019)). If there is a power imbalance between the two Pcal beams, or if the Pcal's centre of force is offset from the nominal position, the test mass will rotate periodically. For modulation frequencies well above 1 Hz, the equation of motion of the freely rotating test mass can be written as,

$$\ddot{\Omega} = \frac{a}{I} F(\omega). \tag{6.8}$$

where I is the moment of inertia about the axis parallel to the surface of the test mass and through the center of the test mass, $\ddot{\Omega}$ is the angular acceleration, $\vec{a}$ is the displacement offset and $F(\omega)$ is the Pcal force (Goetz (2010)). The amplitude is given by

$$\Omega = \frac{2a\cos\theta}{c} R(\omega) P(\omega). \tag{6.9}$$

where $R(\omega)$ is the torque-to-angle transfer function in units of $1/(Nm)$. If the interferometer beam is at it's nominal position at the centre of the test mass, the rotation has no effect since displacement on one side is cancelled by the negative displacement on the other side.

However, if the interferometer beam is offset, denoted by $\vec{b}$, the interferometer senses a length change given by

$$x = \frac{2\cos\theta}{c} R(\omega) P(\omega) (\vec{a} \cdot \vec{b}) \tag{6.10}$$

Combining Equation(6.7) and Equation (6.10) we can write the induced fiducial displacement as

$$x(\omega) = \frac{2P(\omega)\cos\theta}{c}\left[S(\omega) + R(\omega)(\vec{a}\cdot\vec{b})\right] \approx -\frac{2P(\omega)\cos\theta}{c}\left[\frac{1}{M\omega^2} + \frac{(\vec{a}\cdot\vec{b})}{I\omega^2}\right] \tag{6.11}$$

where $S(\omega) \approx -1/M\omega^2$ and $R(\omega) \approx -1/I\omega^2$ for frequencies above 20 Hz i.e. at frequencies much higher than the ETM pendulum resonant frequency of 1 Hz, where the suspended mass can be approximated as a free mass. The negative sign is due to the fact that the force acts opposite to the direction of the displacement. M and I is the mass and the moment of inertia of the suspended mirror. $S(\omega)$ and $R(\omega)$ for a LIGO 40 kg ETM are plotted in the upper-left and lower-left panels of Figure 6.1 along with the longitudinal and rotational transfer functions for a free mass, respectively. As shown in the right panels of Figure 6.1, at frequencies above 20 Hz both $S(\omega)$ and $R(\omega)$ are well approximated by the response of a free-mass within 0.1 % and 0.3 % respectively.

6.2. HARDWARE

Each Advanced LIGO detector has two Pcal systems, one installed at each end station. Conventionally, the calibration of the detector is performed using one Pcal system and the second system serves as a backup system and for injecting simulated GW signals to test the performance of detection pipelines. In this dissertation we will discuss a new formalism that uses both of the Pcal systems to estimate the fiducial displacement of the suspended mirrors, which allows us to improve accuracy of the estimate. A schematic diagram of a LIGO Pcal system is shown in Figure 6.2. It consists of a transmitter module that houses the laser, an acousto-optic modulator (AOM), power sensors, BS, relay

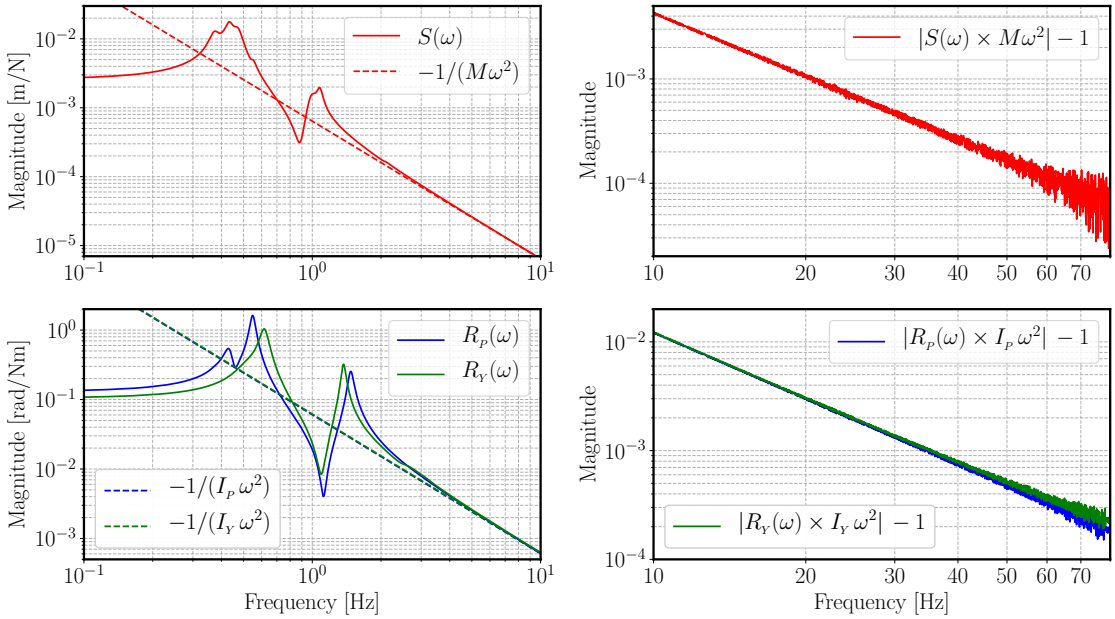

Figure 6.1. *Upper-left panel*: Modeled force-to-displacement transfer function for a suspended LIGO end test mass and for a free mass, -1/($M\omega^2$). *Lower-left panel*: Modeled torque-to-rotation transfer functions for a suspended LIGO end test mass for both pitch and yaw, and for a free mass, -1/($I\omega^2$). *Upper-right panel* and *Lower-right panel*: Discrepancy between the modeled and free-mass transfer functions. Above 20 Hz, the $S(\omega)$ discrepancy is less than 0.1 %, and $R(\omega)$ discrepancy is less than 0.3 %. credit:D Bhattacharjee *et al.* (2021)

optics, etc and a receiver module that houses relay optics and a receiver power sensor. The output of a 2 W laser operating at 1047 nm is directed to an AOM after passing through a polarizing BS cube. The laser wavelength is close enough to the 1064 nm wavelength of the interferometer beam to ensure high reflectivity from the test mass coatings. The AOM diffracts a fraction of the laser power that varies in response to a control signal. The maximum diffraction efficiency is 80%. The first-order diffracted beam is incident on an uncoated wedge BS oriented near Brewster's angle, which generates the sample beams for the two photodetectors. The non diffracted beam is dumped. One of the sample beam generated by the wedge BS is directed to a 2-inch-diameter integrating sphere with an InGaAs photodetector that monitors the laser power directed into the vacuum chamber. The

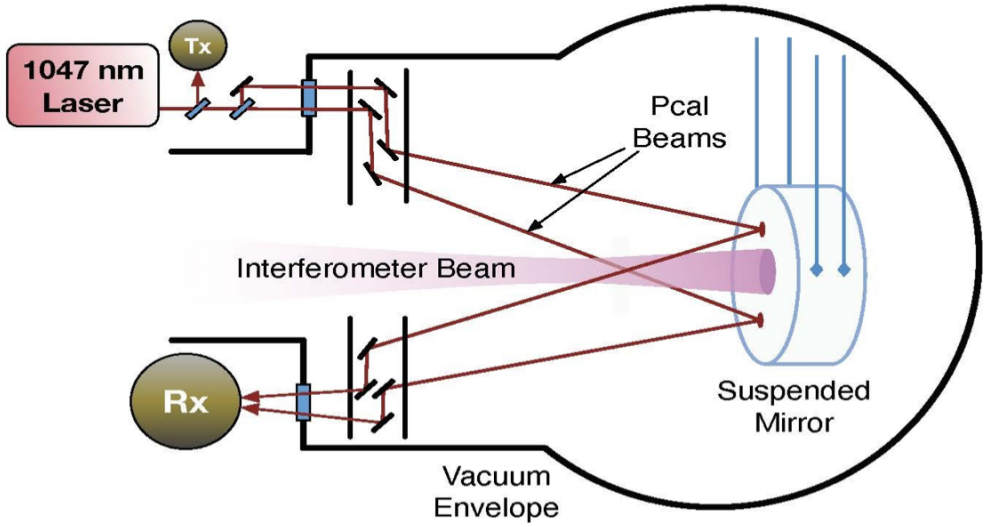

Figure 6.2. Schematic diagram showing the Pcal layout. The calibrated power sensors enable on-line monitoring of the amplitudes of the fiducial periodic displacements induced by the power modulated Pcal beams reflecting from the suspended mirror.

second sample beam is directed to a similar photodetector which serves as the sensor for Optical Follower Servo (OFS) (Canete (2013)). The OFS ensures that the output of the OFS photodetector matches the requested modulation waveform, compensating for non-linearity in the acusto-optic modulation process. The beam transmitted through the wedge BS is mode-matched so that it forms a 2 mm radius beam waist near the surface of the ETM. It is then passed through a BS which divides the beam into two beams with equal power. The two beams enter a separate section of the transmitter module housing that is used to place a transfer power standard, called the Working Standard (WS) power sensor, for laser power calibration as described in detail in the next section. A schematic diagram of the transmitter module and receiver module layout is shown in Figure (6.3).

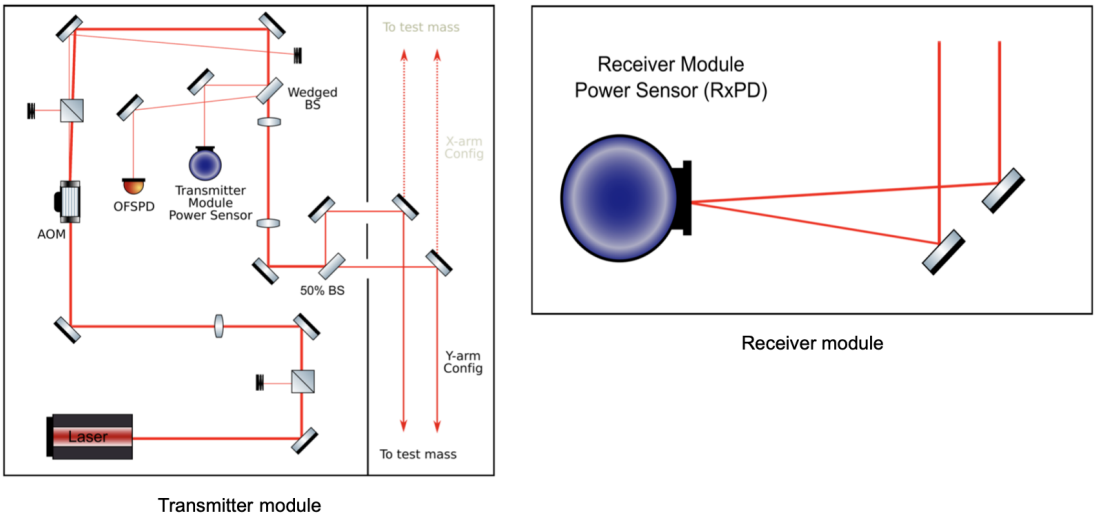

Figure 6.3. Schematic diagram showing the optical layout inside the transmitter (left) module and the receiver (right) module. The power-modulated laser being reflected off the suspended mirror, is continually monitored by the receiver module power sensor, Rx. credit:Karki *et al.* (2016)

The two beams from the transmitter module are directed to the vacuum chamber through optical-quality windows with anti-reflection coatings. Each beam is relayed by mirrors mounted on a periscope structure located inside the vacuum envelope to reduce angles of incidence on the ETM and thus avoid occlusion by stray light baffles. The nominal angle of incidence is 8.72 degrees.

The reflected beams are relayed by a second set of mirrors mounted on the periscope structure on the receiver side and exit the vacuum chamber through similar windows. The beams are directed to a power standard located inside the receiver module by a pair of mirrors. Monitoring the laser power before being directed into the vacuum envelope and after exiting it enables tracking changes in optical efficiency between the transmitter side and the receiver side. The power reflectivity of the ETM is greater than 0.9999 but the anti-reflection coated vacuum windows and the relay mirrors located inside the vacuum

envelope reduce the optical efficiency, η, between the transmitter and receiver modules to approximately 0.985 - 0.990, i.e. the overall optical loss is about 1.0 to 1.5 % (Karki *et al.* (2016)).

6.3. PCAL DISPLACEMENT FIDUCIALS

The periodic force exerted on the ETM due to the power-modulated laser beam reflecting from the mirror surface is given by Equation (6.11) in Subsection 6.1, which can be rewritten as

$$x(\omega) \simeq -\frac{2\cos\theta}{Mc\,\omega^2} P(\omega) \left[1 + \frac{M}{I}(\vec{a}\cdot\vec{b})\right]. \tag{6.12}$$

Since neither the magnitude nor direction of the Pcal center of force offset is known, only the maximum magnitude of $\vec{a}$ can be estimated. Therefore, $(2\cos\theta/Mc\omega^2)P(\omega)$ is the nominal displacement induced by the Pcal system and the second term in the square brackets is treated as the relative uncertainty in the displacement resulting from unintended rotation of the ETM, denoted by ϵ_{rot}. The calculation of the nominal displacements induced by the Pcal systems requires estimates of three parameters: the angle of incidence of the Pcal beams on the ETM surface, the mass of the ETM, and the laser power reflecting from the highly-reflective ETM surface inside the vacuum envelope. Accurate estimates of the Pcal displacements rely on the accurate measurement of these parameters.

6.3.1. Calibration of The Power Sensors. In order to measure the power being reflected from the ETM accurately, accurate calibration of the Pcal laser power sensors located outside the vacuum envelope, inside the transmitter and receiver module is required, (the Tx and Rx sensors in Figure 6.2) accounting for the optical loss between the ETM and the Rx sensor. The Tx sensor samples a fraction of the laser power when the beam is directed into the vacuum chamber and is used for optical efficiency measurements. Howevr, the Tx sensor is subject to variations in the BS that reflects the small sample of the input

light. The Rx sensor, on the other hand, receives almost all of the laser power reflected from the ETM and hence is the primary power sensor for continuous displacement fiducial calibration.

Calibrating the Rx sensor in terms of power reflected from the ETM requires compensating for optical losses between the ETM and the sensor. For that, the overall optical efficiency, η, measured from outside the vacuum chamber, needs to be apportioned between the input path (between the Tx sensor and the ETM), η_T, and the output path (between the ETM and the Rx sensor), η_R.

$$\eta_R = \sqrt{\eta/\beta} \text{ and } \eta_T = \sqrt{\eta\,\beta}, \tag{6.13}$$

where $\beta = \eta_T/\eta_R$ is the optical efficiency ratio. The power reflecting from the ETM is thus estimated in terms of the power measured by the Rx sensor, $P_R(\omega)$ corrected for the optical efficiency on the receiver side. It can be written as

$$P(\omega) = P_R(\omega)/\eta_R\,. \tag{6.14}$$

The power at the ETM can also be calculated as $P(\omega) = \eta_T\ P_T(\omega)$ where $P_T(\omega)$ is the power measured by the Tx sensor. However, this sensor is less reliable because it is insensitive to changes in the optical efficiency between the BS in the TX module and the Rx sensor, in addition to changes in the BS ratio as mentioned earlier.

The on-line power sensors at each end station are calibrated via a three-step process as shown schematically in Figure 6.4: *i*) a transfer standard referred to as the *Gold Standard* (GS) is calibrated to SI units at the National Institute of Standards and Technology (NIST) in Boulder, Colorado; *ii*) the calibration of the GS is propagated to another transfer standard referred to as the *Working Standards* (WS) by making a set of responsivity ratio measurements in a dedicated optical laboratory at LHO. Each observatory maintains its own WS,

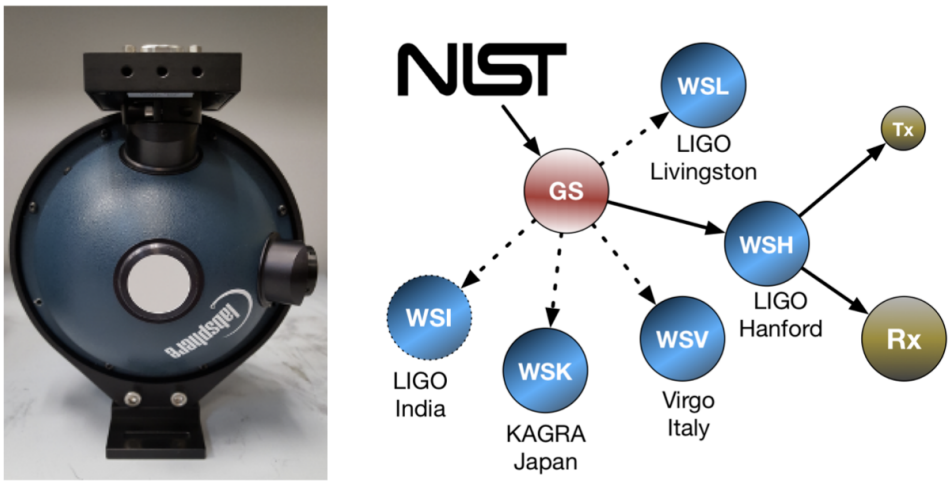

Figure 6.4. *Left*: Image of a Pcal power standard comprising an integrating sphere with Spectralon® interior shell and custom-built photodetector. *Right*: Schematic diagram showing the transfer of laser power calibration from SI units via calibration of a GS by NIST. Then from the GS to WS, one for each observatory, and then to the power sensors (Tx and Rx) located at the interferometer end stations. These calibrated power sensors enable on-line monitoring of the amplitudes of the fiducial periodic displacements induced by the power modulated Pcal beams reflecting from the suspended mirror.

and all of them are referenced to a single GS by making measurments at LHO, and finally *iii*) the calibration of a WS is transferred to the Tx and Rx power sensors at each observatory by making responsivity ratio measurements at the end stations.

The Figure 6.4 also shows a typical Pcal transfer standard comprising an integrating sphere with a Spectralon® interior shell (Labsphere model 3P-LPM-040-SL) and a custom-built InGaAs photodetector.

The GS is sent to NIST annually for calibration. As mentioned earlier, to transfer the GS calibration to the various working standards, a series of responsivity ratio measurements are made in a laboratory at LHO (LIGO Pcal Group (2020b)). A spare Pcal transmitter module is used (Karki *et al.* (2016)). It incorporates laser power stabilization and delivers two output beams with powers balanced to within 1 %. The GS and one WS are mounted

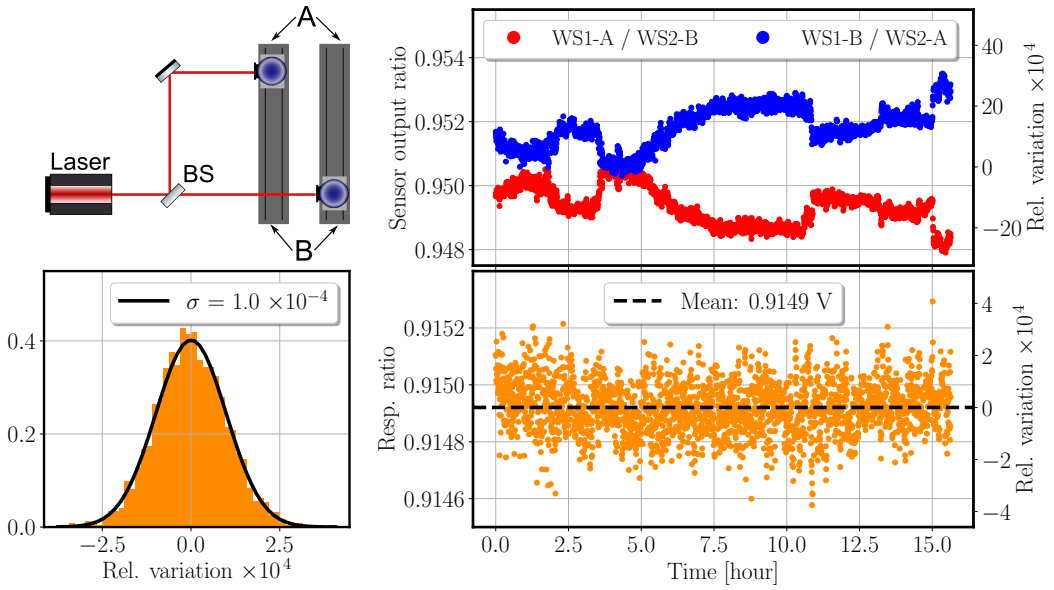

Figure 6.5. Responsivity ratio measurement setup and results for two working standards. *Upper-left panel*: schematic diagram of laboratory setup with pneumatic slides for alternating positions of the two sensors between the BS transmitted and reflected beams; *Upper-right panel*: time series of ratio in A-B configuration (red) and in B-A configuration (blue); *Lower-right panel*: square root of the product of subsequent A-B, B-A ratios, $\alpha_{\mathrm{W1W2}} = \rho_{\mathrm{WS1}}/\rho_{\mathrm{WS2}}$; *Lower-left panel*: normalized histogram of the relative variations in the 2800 measurements, each a from a twenty second long sequential measurement suite. credit:D Bhattacharjee *et al.* (2021)

on automated pneumatic slides that allow us to switch the detectors' position between the transmitted beam and the reflected beam as shown schematically in the upper-left panel of Figure 6.5. Recording the output voltages of the two detectors simultaneously in a given configuration minimizes variations induced by laser power changes; sequential measurements with the detector positions swapped minimizes the impact of variations in the BS that separates the two beams. The integrating spheres are largely insensitive to the incident beam position, angle, polarization, and size. However, they exhibit laser speckle due to the coherence of the laser light that temporally correlates the output time series (Goodman (2009)). Thus laser speckle limits the precision of the responsivity ratio measurement and is a potential source of systematic errors. During responsivity ratio

measurements in the LHO laboratory, the temporal correlation of the output time series is broken by recording shorter time series segments and swapping sensor positions more frequently.

A typical reported responsivity ratio value, α_{WG}, is given by the average of 100 measurements. The data for each measurement is comprised of four, five second long time series sampled once per second. The first two are recorded simultaneously with the detectors in the A-B configuration as shown in the upper-left panel in Figure 6.5, and the last two with the detector positions swapped to the B-A configuration. Assuming that at time t_1 WS is in the transmitted beam path (A) and GS is in the reflected beam path (B) and then swapped such that at t_2 WS is in B position and GS is in A position, the output of each detector can be written as

$$V_W(t_1) = T_{BS}P(t_1)\rho_W\,, \tag{6.15a}$$

$$V_G(t_1) = R_{BS}P(t_1)\rho_G\,, \tag{6.15b}$$

$$V_W(t_2) = R_{BS}P(t_2)\rho_W\,, \tag{6.15c}$$

$$V_G(t_2) = T_{BS}P(t_2)\rho_G\,. \tag{6.15d}$$

Here V_W and V_G are the output voltages from the two standards, T_{BS} and R_{BS} are the power transmisson and reflection coefficients of the BS and P is the power of the laser source. ρ_W is the responsivity of the WS and ρ_G is that of the GS. Laser power variations are eliminated by taking the ratio of the pair of time series recorded simultaneously:

$$R_1 = \frac{1}{N_1}\sum_{i=1}^{N_1}\frac{V_{W_i}(t_1)}{V_{G_i}(t_1)} = \frac{T_{BS}\rho_W}{R_{BS}\rho_G}\,, \tag{6.16a}$$

$$R_2 = \frac{1}{N_2}\sum_{i=1}^{N_2}\frac{V_{W_i}(t_2)}{V_{G_i}(t_2)} = \frac{R_{BS}\rho_W}{T_{BS}\rho_G}\,. \tag{6.16b}$$

The index i denotes the i^{th} sample in the time series and typically $N_1 = N_2 = 5$. The square root of the product of the two ratios ($\sqrt{R_1 R_2}$) yields an estimate of the responsivity ratio every twenty seconds (5 seconds to measure each time series and 5 seconds to re-position the sensors). The responsivity ratio is thus given by

$$\alpha_{WG} = \sqrt{(R_1 R_2)} = \frac{\rho_W}{\rho_G}. \tag{6.17}$$

To elucidate this method, individual ratios R_1 and R_2 for 2800 twenty-second long-measurement suites are plotted in the upper-right panel in Figure 6.5. The two data sets 'mirroring' each other indicates variations in the BS ratio. The square root of the product of the ratios from sequential measurements in Equation (6.17), assuming the BS transmission and reflection coefficients haven't changed between the sequential swapped measurements, minimizes the effect of the changes in the BS ratio. The "mirroring" effect is clearly absent in the lower-right panel of Figure 6.5, which shows the 2800 sequential measurements of α_{W1W2}. The standard deviation of the relative variation of the ratio measurements is 1.0×10^{-4} as shown in the normalized histogram in the lower-left panel in Figure 6.5. Since the Pcal power sensor responsivities have non-negligible dependence on temperature (discussed in more detail later), the data in the lower panels of Figure 6.5 were "de-trended". During this fifteen hour long measurement, variation of relative responsivity of the power sensors due to the laboratory ambient temperature variation by (1.3 K), were corrected by (1.1×10^{-4} /K).

To propagate the WS calibration to the on-line Pcal power sensors at the end stations, a series of measurements are made with a working standard (LIGO Pcal Group (2020a)). They involve placing the WS alternately in the path of one or the other Pcal beam in both the transmitter and receiver modules and recording four minute long time series of the WS, Rx, and Tx power sensors using the observatory digital data acquisition system (Bork *et al.* (2020)). At the end station, there is no provision to swap detector position to break

the temporal correlation of the output time series due to laser speckle as was done for the responsivity ratio measurements in the LHO laboratory. Instead, longer time series are recorded and averaged to minimize the impact of laser speckle.

The end station data acquisition system is used for the WS signal, rather than the digital volt meter that is used for the responsivity ratio measurements in the laboratory setup. This is both for convenience and to synchronize the WS data with the Rx and Tx sensor data. Propagating the WS calibration to the end station thus involves the additional step of measuring the conversion factor, ζ_W, between volts registered by the digital volt meter and digital counts reported by the end station data system for the WS. This is accomplished via a calibrated voltage source (Martel Model IVC-222HPII). Each time, before making end station measurements, the factor ζ_{MW} which is the ratio of the Martel output in volts to the Keithley voltmeter output in volts in the LHO optics laboratory is measured. At the end station, another factor ζ_{WM} which is the ratio of the WS readout recorded by the end station data acquisition system in counts to the Martel calibrated voltage source in volts is measured. These two factors together yield the volts-per-counts converter factor $\zeta_W = \zeta_{WM}\zeta_{WM}$ for the WS.

Synchronizing these time series reduces the impact of laser power variations. The measurements yield the Rx/WS responsivity ratio, $\rho_R/\rho_W = \alpha_{RW}$. They also yield estimates of the overall optical efficiency, η. Combining the measurements described above, the responsivity calibration factor for the Rx end station power sensors is given by

$$\rho_R = \rho_G \, \alpha_{WG} \, \alpha_{RW} \, \zeta_W \, , \tag{6.18}$$

in units of ct/W.

The laboratories where Pcal calibration measurements are made i.e., at the NIST, at LHO and the end stations are all maintained at different temperatures. Thus, to realize high-accuracy calibration, the temperature coefficients of the transfer standards must be

taken into account when transferring laser power calibration from NIST to the sensors at the interferometer end stations. For a given power sensor, the temperature dependence of the responsivity can be expressed as

$$\frac{\rho(T)}{\rho_0} = 1 + \kappa(T - T_0), \tag{6.19}$$

where ρ_0 is the responsivity of the sensor measured at a reference temperature, T_0, and κ is the temperature coefficient of the relative responsivity for the given power standard. By including the temperatures at which each measurement in the calibration transfer process is made, Equation (6.18) can be rewritten as

$$\rho_R|_{T_E} = \rho_G|_{T_N} \frac{\rho_G|_{T_L}}{\rho_G|_{T_N}} \frac{\rho_W|_{T_L}}{\rho_G|_{T_L}} \frac{\rho_W|_{T_E}}{\rho_W|_{T_L}} \frac{\rho_R|_{T_E}}{\rho_W|_{T_E}} \zeta_W = \rho_G \, \xi_{LN} \, \alpha_{WG} \, \xi_{EL} \, \alpha_{RW} \, \zeta_W \,, \tag{6.20}$$

where T_N is the NIST laboratory temperature, T_L is the LHO laboratory temperature, and T_E is the end station temperature. The factor ξ_{LN} corrects for differences in the GS responsivity measured at the NIST and LHO laboratory temperatures and the factor ξ_{EL} corrects for differences in the WS responsivity measured at the LHO laboratory and end station temperatures. These temperature-related correction factors can be written as

$$\begin{aligned} \xi_{LN} &= \frac{\rho_G|_{T_L}}{\rho_G|_{T_N}} = (1 + \kappa_G \Delta T_{LN}) \,, \\ \xi_{EL} &= \frac{\rho_W|_{T_E}}{\rho_W|_{T_L}} = (1 + \kappa_W \Delta T_{EL}). \end{aligned} \tag{6.21}$$

Here κ_G and κ_W are the temperature coefficients for the GS and WS sensors normalized to their respective responsivities at their reference temperatures, T_N and T_L. $\Delta T_{LN} = T_L - T_N$ and $\Delta T_{EL} = T_E - T_L$.

Correcting for the temperature difference between various laboratories and for the optical loss suffered by the laser beam, the power calibration factor of the Rx power sensor ρ_R from Equation (6.18) can be rewritten as

$$P(\omega)|_{T_E} = \frac{d_R(\omega)}{\eta_R\,\rho_R} = \frac{d_R(\omega)}{\eta_R\,\rho_G\,\xi_{LN}\,\alpha_{WG}\,\xi_{EL}\,\alpha_{RW}\,\zeta_W}\,. \tag{6.22}$$

where d_R is the digital output of the Rx sensor in counts.

6.3.2. Calculation of Displacement Factors. Once the power reflecting from the suspended mirror inside the vacuum chamber is accurately estimated, the fiducial displacement of the ETM induced by the Pcal forces can be calculated by combining Equation (6.12), and Equation (6.22) in units of m/ct as

$$x(\omega) \simeq -\frac{2\cos\theta}{M\,c\,\omega^2}P(\omega) = -\frac{2\cos\theta}{M\,c\,\omega^2}\frac{d_R(\omega)}{\eta_R\,\rho_G\,\xi_{LN}\,\alpha_{WG}\,\xi_{EL}\,\alpha_{RW}\,\zeta_W} = -\frac{X}{\omega^2}\,d_R(\omega)\,. \tag{6.23}$$

Here the displacement factor, X, is defined as

$$X = \frac{2\cos\theta}{M\,c}\frac{1}{\eta_R\,\rho_G\,\xi_{LN}\,\alpha_{WG}\,\xi_{EL}\,\alpha_{RW}\,\zeta_W}\,. \tag{6.24}$$

Equation (6.23) gives the calibrated digitized output of the Rx sensor. Like LIGO, most GW observatories have implemented, or plan to implement, Pcals at both end stations. The Pcal systems at each end station are typically calibrated using the same procedures. Laser interferometers are designed to sense DARM length variations induced by ETM motion and respond equally to ETM movement in either arm (except for the sign of the relative displacement) to the level of 1×10^{-4}% citeprivate communications with G. Vajente and H. Yamamoto. Thus, comparing Pcal fiducials produced at both end stations in the interferometer output signal directly measures the ratio of the Pcal calibrations at each end. This comparison can be used to reduce the uncertainty in the induced displacements due to factors that are not common to both ends. The X/Y calibration comparison is realized by

modulating the two Pcal systems at frequencies very close to each other within the sensitive band of the interferometer. Comparison of the amplitudes of the peaks in fast Fourier transforms (FFTs) of the calibrated Pcal end station sensor outputs, each normalized to the amplitudes of the peaks in the interferometer output signal, yields the X/Y Pcal calibration comparison factor, χ_{XY}. Using the Equation (6.23), χ_{XY} can be written as

$$\chi_{XY} = \frac{X_X d_{R_X}/\omega_X^2}{\Delta L_X|_{\omega_X}} \Bigg/ \frac{X_Y d_{R_Y}/\omega_Y^2}{\Delta L_Y|_{\omega_Y}}, \tag{6.25}$$

where subscript X and Y denote the X- and Y-end station respectively. ΔL is the amplitude of the peak in the interferometer output signal.

If there were no uncertainties in the displacement calibration factors for both end stations, χ_{XY} would be 1. However, errors induced by uncertainties in non-common factors between the two end stations ($\cos\theta$, M, η_{R}, ξ_{EL}, α_{RW}, ζ_{W}, and ϵ_{rot}) cause it to deviate from 1.

Using χ_{XY} and these uncertainty estimates, correction factors for each end station can be calculated. The *combined* displacement factors are defined by

$$X_X^c \equiv X_X/C_X \text{ and } X_Y^c \equiv X_Y\ C_Y \tag{6.26}$$

where C_X and C_Y are the X-arm and Y-arm correction factors such that

$$\frac{X_X^c}{X_Y^c}\chi_{XY} \equiv 1\,. \tag{6.27}$$

The superscript c denotes that these displacement factors are calculated from the combination of the X-end and Y-end calibration results. From Equation (6.27), it can be derived that

$$C_X C_Y \equiv \chi_{XY}\,. \tag{6.28}$$

For the special case where the uncertainties are the same at both end stations, the factors are given by $C_X = C_Y = \sqrt{\chi_{XY}}$.

In general, the correction factors are calculated using the weighted geometric mean, μ_g, of 1 and χ_{XY}. The weighting factors are given by the inverse of the estimated variances in the end station displacement factors, X_X and X_Y, due to uncertainty contributions that are not common to both end stations. With the X_X weighting factor, w_X, applied to 1 and the X_Y weighting factor, w_Y, applied to χ_{XY}, the weighted geometric mean is given by

$$\begin{aligned} \mu_g &= exp\left(\frac{w_X ln(1) + w_Y ln(\chi_{XY})}{w_X + w_Y}\right) = \left(\frac{w_Y ln(\chi_{XY})}{w_X + w_Y}\right) \\ &= \chi_{XY}^{w_Y/(w_X+w_Y)} \end{aligned} \tag{6.29}$$

Note, if $w_X \gg w_Y$, $\mu_g \approx 1$ and the Pcal displacement factor at the X end is corrected by a negligible amount, i.e. $C_X \approx 1$ and the displacement factor at the Y end is corrected by an amount almost equal to χ_{XY}. On the other hand, if $w_Y \gg w_X$, then $\mu_g \approx \chi_{XY}$ and the Pcal displacement factor at the X end is corrected by an amount almost equal to χ_{XY} and the displacement factor at the Y end is corrected by a negligible amount, i.e. $C_X \approx 1$. Thus, a solution for the correction factors is given by

$$C_X = \mu_g \text{ and } C_Y = \chi_{XY}/\mu_g\,. \tag{6.30}$$

The uncertainties in these factors are given by the weighted relative standard error on the geometric mean. The uncertainties in the parametersC_X or C_Y along with uncertainties in ρ_G, α_{WG} and ξ_{LN} added in quadrature gives the overall uncertainty estimate in the displacement fiducials generated by the Pcal systems.

In the next section we will apply the formalism detailed in this section to calculate the Pcal-induced displacement factors and estimate the uncertainty associated with them for the O3 run.

7. MEASUREMENTS AND UNCERTAINTY ESTIMATES

In this section the results of Pcal measurements made during Advanced LIGO's O3 run are presented. The methods described in Subsections 6.3.1 and 6.3.2 were applied for Pcal calibration. Measurements were made for both the LHO and LLO interferometers, but for simplicity only the LHO results are presented. The content of this section is based on (D Bhattacharjee *et al.* (2021)), in which I was the lead author.

7.1. MEASUREMENT RESULTS AND UNCERTAINTY ESTIMATES

The measured and estimated values of the parameters that contribute to the displacement factors described in Section 6.3.2, and their associated relative uncertainties, are summarized in the tables below. We follow the convention used by NIST and detailed in (Taylor and Kuyatt (1994)), employing *Type A*, *Type B*, or *Type C* evaluations for estimates of relative standard uncertainties for each parameter.

According to (Taylor and Kuyatt (1994)) evaluation of uncertainty by statistical analysis of a series of measurements is referred to as Type A. The individual measurements are assumed to be independent and normally distributed. Thus the relative standard uncertainty u_{rel} is determined by

$$u_{rel,A} = \frac{\sigma}{\overline{x}\sqrt{N}} = \frac{1}{\overline{x}\sqrt{N}}\sqrt{\frac{1}{N-1}\sum_{i=1}^{N}(x_i - \overline{x})^2} \tag{7.1}$$

where x_i are the individual measurements, $\overline{x}$ is the average of the measured values, N is the number of measurements and σ is the standard deviation of the N measurements.

Evaluation of uncertainty using means other than statistical analysis of measurements, based on scientific judgement using all relevant information available, is referred to as Type B. We estimate a lower and upper limit for the value, a_- and a_+ respectively. The probability that the value of the quantity lies within the estimated window is close to 100%.

If we model the value of the quantity by a uniform or rectangular probability distribution, then the relative standard uncertainty is given by

$$u_{rel,B} = \frac{a_+ - a_-}{2\sqrt{2}} \,. \tag{7.2}$$

In the case, where we model the value by a sine wave or a U-shaped probability density function, then the relative standard uncertainty is given by $u_{rel} = (a_+ - a_-)/2\sqrt{3}$.

Uncertainty estimates resulting from combinations of Type A and Type B evaluations of uncertainty are referred to as a Type C. The overall uncertainty is estimated by adding the relative uncertainties of all component types in quadrature

$$u_{rel} = \sqrt{\sum u_{rel,A}^2 + \sum u_{rel,B}^2 + \sum u_{rel,C}^2} \,. \tag{7.3}$$

In the following subsections we describe how we measure the different parameters discussed in Subsection 6.3 to calculate the fiducial displacement generated using the Pcals and to estimate the uncertainties associated with the measured values. Type A uncertainties have been corrected for small sample size using Student's T corrections.

7.1.1. End Station Power Sensor Calibration. Calibration of the Pcal power sensors at the end stations is achieved by measurement of the individual parameters on the right-hand side of Equation (6.20). The transfer standards, GS and WS, were upgraded in 2018 (Lecoeuche *et al.* (2019)), before the start of the O3 observing run. The modifications included changes in the mounting of the photodetector housing to the integrating sphere port to improve robustness and reduce the impact of laser speckle. The transimpedance amplifier was also changed to reduce complexity and minimize dark offsets.

The upgraded GS was calibrated by NIST in December 2018. The reported GS responsivity, ρ_G, is -8.0985 V/W with a relative uncertainty of $0.315\,\%$ ($1\,\sigma$) (LIGO Pcal Group (2018)). The responsivity ratio measurements between one or more of the working

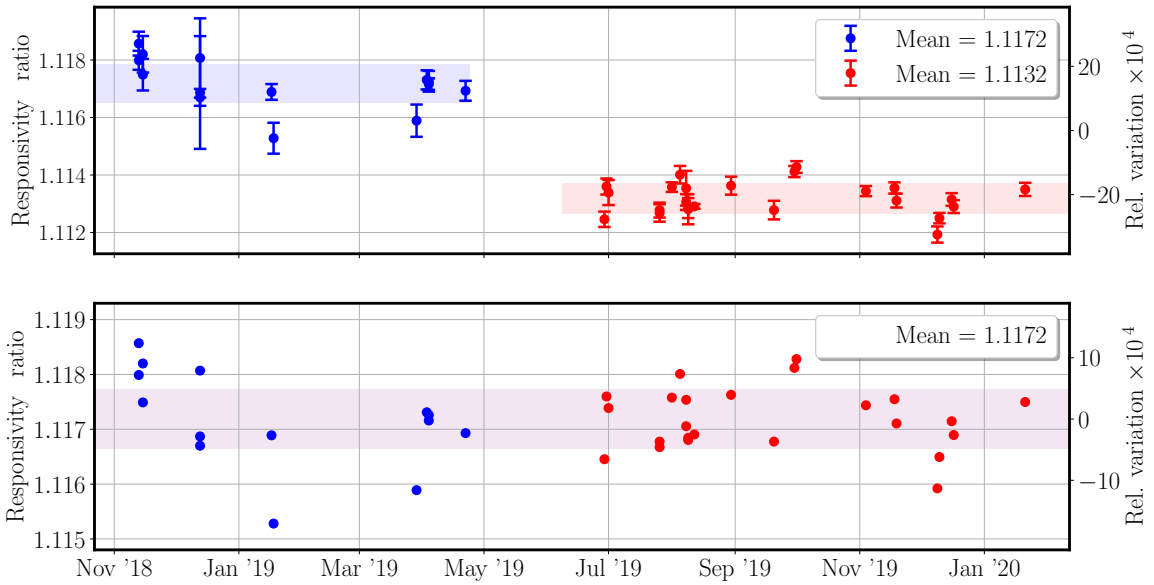

Figure 7.1. WSH to GS responsivity ratio, α_{WG}, measured between November 2018 and February 2020. *Upper panel*: The data plotted in red were measured after June 2019 when the Pcal responsivity measurement setup was moved to another building. The colored bands indicate ± 1 standard deviation for each measurement group. The error bars, ± 1 standard error on the mean for each data point have been magnified by a factor of twenty to increase visibility. Note that they are not used for weighting, as explained in the text. *Lower panel*: Same data as upper panel, but with the red data points shifted by the ratio of the means of the blue and red data sets (multiplied by 1.00359). The step in the data is attributed to a change in the GS responsivity that occurred during the move.

standards and the GS, both before shipping the GS to NIST and immediately after its return from calibration at NIST, were used to determine whether changes occurred during shipping. No statistically significant changes were observed.

However, it can be seen in the upper panel of Figure 7.1 that there was a significant drop in α_{WG} values by almost a factor of 0.36 % between May and July 2019. This drop coincided with the responsivity ratio measurement setup being moved to a different building at the LHO. The fact that measurements of the responsivity ratio between WS for Hanford (WSH) and the Rx sensors at the LHO end stations (see Figure 7.2) show no corresponding change in the value seem to indicate that the change in α_{WG} was caused by a change in the

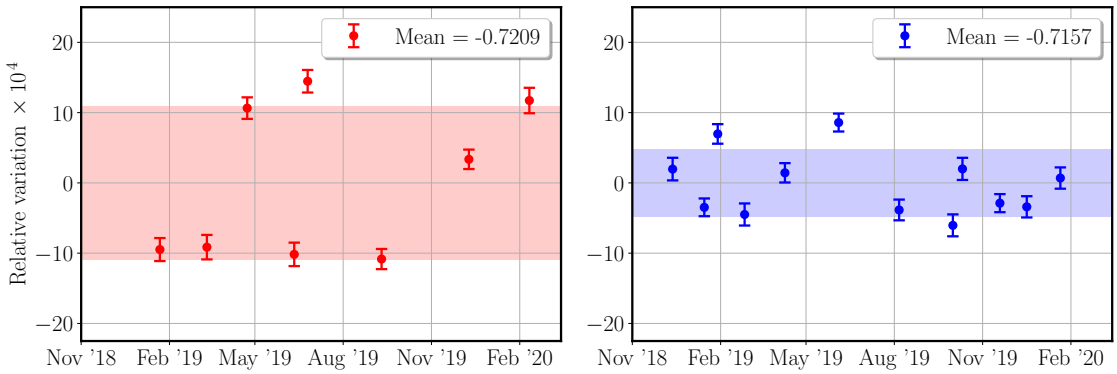

Figure 7.2. Relative variation of the responsivity ratio, α_{RW}, of the Rx and WSH power sensors, measured at the LHO X-end (*left panel*) and Y-end (*right panel*) stations. The shaded regions are ± 1 standard deviation about the weighted mean values listed in the legends. The errors bars are estimated using the formalism detailed in Appendix A of Karki (2019).

GS responsivity, ρ_G, alone. This increase in responsivity was due to a shift in the interior Spectralon shell of the GS. The lower panel in Figure 7.1 shows the same data as in the upper panel, but with the data plotted with the red points, for measurements taken after the move to the new building at LHO, shifted up (multiplied by 1.0036).

The error bars in the upper panel have been magnified by a factor of twenty for better visibility, but have not been used for weighting. Since each data point is the mean of a set of between 25 and 1200 measured values, the variations in the data are dominated by systematic variations, not the statistical variations of the measurements within each set. Thus, weighting the data points would bias the estimate of the overall mean towards the suites with larger numbers of measurements. The mean and the relative uncertainty (estimated using the Equation (7.1)) of α_{WG} for WSH, from the lower panel of Figure 7.1, in which the error bars have been omitted, are listed in the Table 7.1.

Table 7.1. Measured responsivities of the Pcal end station power sensors, ρ_R, together with contributing factors (indented) and uncertainties, for the LHO interferometer during the O3 observing run. For Type A uncertainties, the number of measurements is noted in parentheses.

Param	LHO X-end		LHO Y-end		**Units**	**Type**
	Values	**u_{rel} (%)**	**Values**	**u_{rel} (%)**		
ρ_R	1.068e4	0.328	1.061e4	0.326	ct/W	C
ρ_G	-8.0985	0.315	Common with X-end		V/W	C
α_{WG}	1.1172	0.010 (38)	Common with X-end		-	A
α_{RW}	-0.7209	0.042 (8)	-0.7157	0.014 (12)	-	A
ζ_W	1636.9	0.002 (8)	1637.6	0.002 (9)	ct/V	A
ξ_{LN}	1.0020	0.070	Common with X-end		-	C
ξ_{EL}	0.9986	0.028	0.9986	0.028	-	C

To calibrate the on-line Pcal Rx and Tx power sensors at the end stations, a series of responsivity ratio measurements using a WS are performed (LIGO Pcal Group (2020a)). The Rx to WSH responsivity ratios, α_{RW}, for the LHO X-end and Y-end sensors measured between December 2018 and March 2020, are shown in Figure 7.2.

The error bars are estimated from the 240 second long time series recorded for each element of the measurement suite, using the formalism described in Appendix A of (Karki (2019)). This method uses the standard deviations of the data sets rather than estimating standard errors on the mean values, because the data are correlated due to laser speckle. The reported values of α_{RW} are the weighted means of the data points, w, calculated using

$$w = \frac{\sum_{i=1}^{N} w_i x_i}{\sum_{i=1}^{N} w_i} \,. \tag{7.4}$$

The weighting factor w_i is the inverse of the variance of each data point. The α_{RW} value and its relative uncertainty for both end stations are listed in the Table 7.1. The α_{RW} measurements are shown in Figure 7.2.

For measurements of α_{WG}, a digital voltmeter (Keithley Model 2100) is used to record the output of the WS photodetector. An ADC converter that is part of the LIGO DAQ system is used for measurements of α_{RW} at the end stations. As mentioned before, the factor that converts the volts measured in the laboratory to the digital counts measured at the end station, ζ_W in Equation (6.18), is measured using a Martel calibrated voltage source. ζ_W is close to, but vary slightly from, the ideal value of 1638.4 ct/V. The measured values of ζ_W and their relative uncertainties are listed in Table 7.1.

7.1.2. Temperature Dependence of the Power Standards. The two temperature correction factors on the right-hand side of the Equation (6.20), ξ_{LN} and ξ_{EL}, compensate for variations in the responsivity of the GS and WS power sensors due to differences between the NIST laboratory, the LHO laboratory, and the end station ambient temperatures. To measure the temperature dependence of the WS responsivity, a temperature sensor (Analog Devices, AD590) was bonded to the photodetector circuit board. The WS was then heated in an oven to about $\sim 7K$ above the ambient laboratory temperature. It was then installed in the responsivity ratio measurement setup and measurements of the WS/GS responsivity ratio were made as the WS cooled to room temperature.

The upper-left panel of Figure 7.3 shows α_{WG}, normalized to the mean value of 1.1172 (see Figure 7.1), and the difference between the WS and GS temperatures plotted versus time as the WS cooled. The lower-left panel shows a linear, least-squares fit to the data indicating a relative responsivity temperature coefficient for WS, κ_W, of $4.38 \times 10^{-4}\,/K$. The uncertainty in the fit is $0.06 \times 10^{-4}\,/K$. To investigate the temperature coefficient of the GS, data was taken with both the WS and the GS at the laboratory ambient temperature. During this period the ambient temperature varied by about 1.3 K. In the upper-right panel of Figure 7.3, the normalized responsivity ratio and the ambient laboratory temperature are plotted versus time. As shown in the lower-right panel, a linear, least-squares fit to

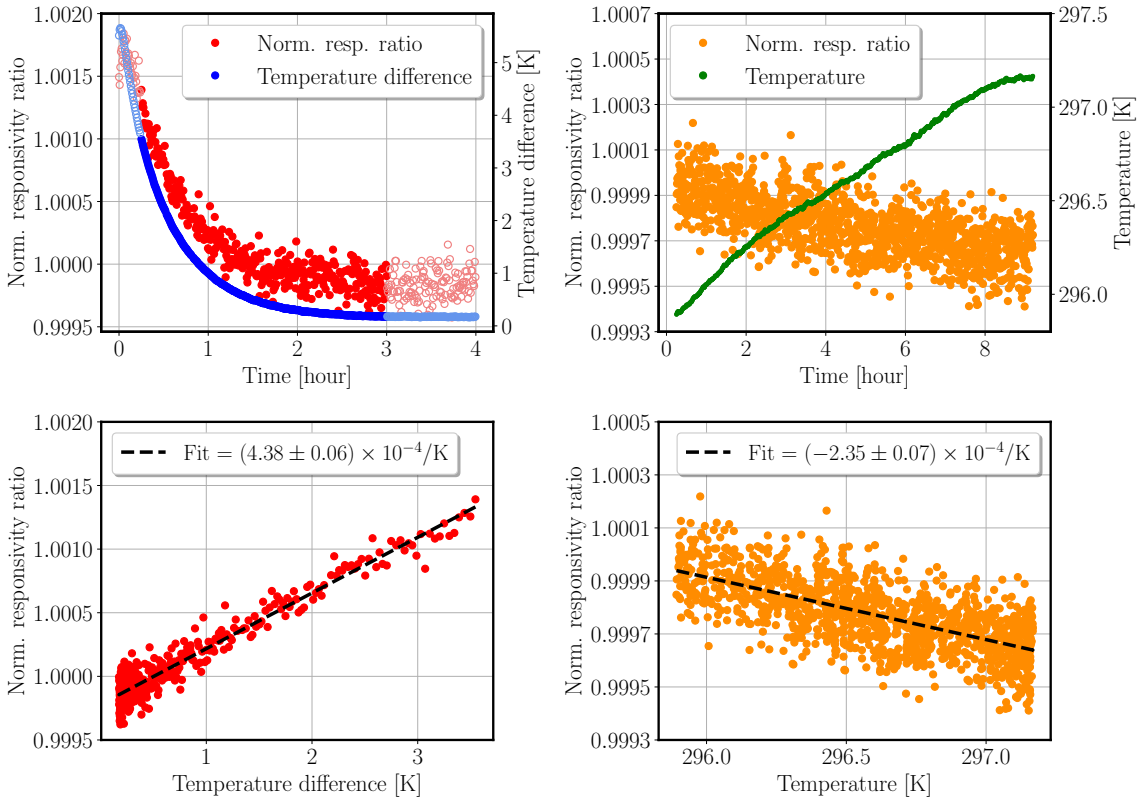

Figure 7.3. *Upper-left panel*: Responsivity ratio normalized to 1.1172 (see 7.1) and temperature difference between the WS and GS versus time as the WS cools after being heated in an oven. *Lower-left panel*: Linear least-squares fit to the data in the upper-left panel. The slope and uncertainty are listed in the legend. *Upper-right panel*: Normalized responsivity ratio and the ambient laboratory temperature plotted versus time when both sensors were at the ambient temperature that varied more than 1 K over almost ten hours. *Lower-right panel*: Linear least-squares fit to the data in the upper-right panel with slope and uncertainty listed in the legend.

the data, yields a slope of -2.35×10^{-4} /K with uncertainty of 0.07×10^{-4} /K. Using κ_W, from the data in the left panels of Figure 7.3, the inferred coefficient for the GS, κ_G, is 6.73×10^{-4} /K.

Temperature differences between the NIST, the LHO, and end station measurement environments were quantified using a set of digital thermometers that were huddled to assess relative offsets, then deployed to each location. The NIST measurement laboratory temperature was set to 20 °C, the mean temperature of the LHO responsivity ratio mea-

Table 7.2. Measured temperature correction factors, ξ_{LN} and ξ_{EL}, for the Pcal end station power sensor calibrations, together with contributing factors (indented) and uncertainties, for the LHO interferometer during the O3 observing run.

Param	LHO X-end		LHO Y-end		**Units**	**Type**
	Values	**u_{rel} (%)**	**Values**	**u_{rel} (%)**		
ξ_{LN}	1.0020	0.070	Common with X-end		-	C
κ_G	6.73e-4	1.4	Common with X-end		1/K	A
ΔT_{LN}	3.0	34	Common with X-end		K	C
ξ_{EL}	0.9986	0.040	0.9986	0.040	-	C
κ_W	4.38e-4	1.4	Common with X-end		1/K	A
ΔT_{EL}	-3.2	28	-3.3	28	K	C

surement laboratory was 23 °C, and the mean X-end and Y-end temperatures were 19.8 °C and 19.7 °C respectively. The end station temperatures varied by about ± 0.5 °C over six months. The calculated values for ΔT_{LN} and ΔT_{EL}, together with the measured GS and WS temperature coefficients, κ_G and κ_W, used to calculate temperature correction factors according to Equation (6.21) are listed in Table 7.2. The relative uncertainties associated with the measured and calculated values are also listed in Table 7.2.

7.1.3. Optical Efficiency. The end station measurements made with the WS also yield measurements of the overall optical efficiency, η, for propagation of the laser beams between the Tx and Rx modules. Assuming that β, which is the optical efficiency ratio of the transmitter or input side efficiency to the receiver or output side efficiency, is constant, using Equation (6.13) we can estimate η_R from the end station measurements. Measured values of η for the LHO X-end and Y-end stations from November 2018 to February 2020 are plotted in Figure 7.4. The error bars, used for calculating weighted values, are generated using the formalism detailed in Appendix B of Karki (2019). The mean values of η_R, β, and η, together with their relative uncertainties, are listed in Table 7.3.

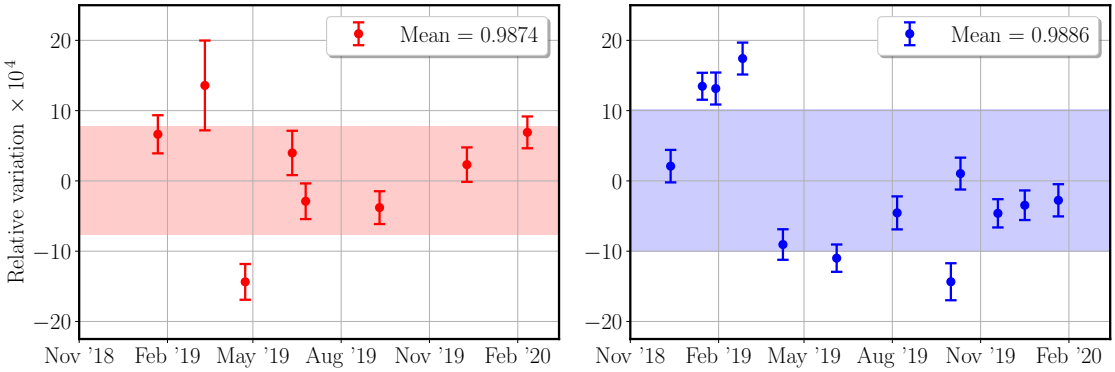

Figure 7.4. Relative variation of the optical efficiency between the transmitter and receiver modules at the end stations, η, measured at the LHO X-end (*left panel*) and Y-end (*right panel*) stations. The shaded regions are ± 1 standard deviation about the weighted mean values listed in the legends. The errors bars are estimated using the formalism detailed in Appendix B of citeP1900127.

7.1.4. Mass of the ETM and Angle of Incidence. At frequencies above the ETM resonance frequency the suspension displacement and rotation transfer functions on the right hand side of Equation (6.12) can be approximated by the responses of a free mass (within 0.1% and 0.3% level respectively, see Figure 6.1). In that case, only the mass of the ETM, M, is required to convert the force to the displacement factor, X, in Equation (6.23). The ETM masses are measured by the vendor that polishes the mirrors and at the end stations before they are suspended. The calibration of the electronic balances used before suspending have been verified using two 20 kg calibrated reference masses. The maximum estimated Type B uncertainty in the ∼ 40 kg suspended mass is 10 g.

The angle of incidence, θ, is determined by the last relay mirrors on the periscope structure located inside the vacuum envelope (Karki *et al.* (2016)). These mirrors direct the Pcal beams such that they impinge on the ETM above and below center, on the vertical center line of the face of the ETM. As mentioned in Subsection 6.2, the nominal angle of incidence is 8.72 degrees. The maximum deviations of this angle are bounded by the size of the periscope optics (2 inch diameter) that relay the beams to the end test mass.

Table 7.3. Measured optical efficiency correction factors, η_R, for the receiver-side end station power sensors, together with contributing factors (indented) and uncertainties, for the LHO interferometer during the O3 observing run. For Type A uncertainties, the number of measurements is noted in parentheses.

Param	LHO X-end		LHO Y-end		**Type**
	Values	$\mathbf{u_{rel}}$ **(%)**	**Values**	$\mathbf{u_{rel}}$ **(%)**	
η_R	0.9942	0.04	0.9948	0.04	C
η	0.9874	0.03 (8)	0.9886	0.03 (12)	A
β	0.9989	0.08 (3)	0.9988	0.08 (3)	A

7.1.5. Uncertainty Due to Unintended Rotation of the ETM. During O3 observation run, the interferometer beams were purposely positioned away from their nominal positions at the center of the suspended ETMs to reduce the impact of point absorbers in the mirror coatings (Brooks *et al.* (2020)). Thus potential uncertainties due to Pcal-induced rotations increased. Angle-to-length coupling investigations using the ETM orientation actuators were used to infer the interferometer beam offsets, denoted by $\vec{b}$ in Figure 7.5, but for Pcal beam position offsets, denoted by $\vec{a}$ in the Figure 7.5, we currently only have estimates of their maximum magnitudes.

The Pcal beams are carefully positioned on the ETM surface when the vacuum envelope is vented, using targets bolted to the suspension structure surrounding the ETM (see left image in Figure 7.5). Monitoring the locations of the beams within the aperture indicates that the maximum Pcal beam position offset is ± 2 mm.

The nominal locations of the two Pcal beams are ±111.6 *mm* above and below the center of the ETM surface. The two beam powers are well balanced to within 1%. Assuming a maximum power imbalance of 1% between the two Pcal beams, adds an additional Pcal beam position offset of $\sim$ 0.5 *mm* to $\vec{a}$. The magnitude of $\vec{a}$ is estimated by adding the Pcal beam position offset and power imbalance contributions in quadrature. During the O3 run the maximum interferometer beam position offsets from center were 29 mm for

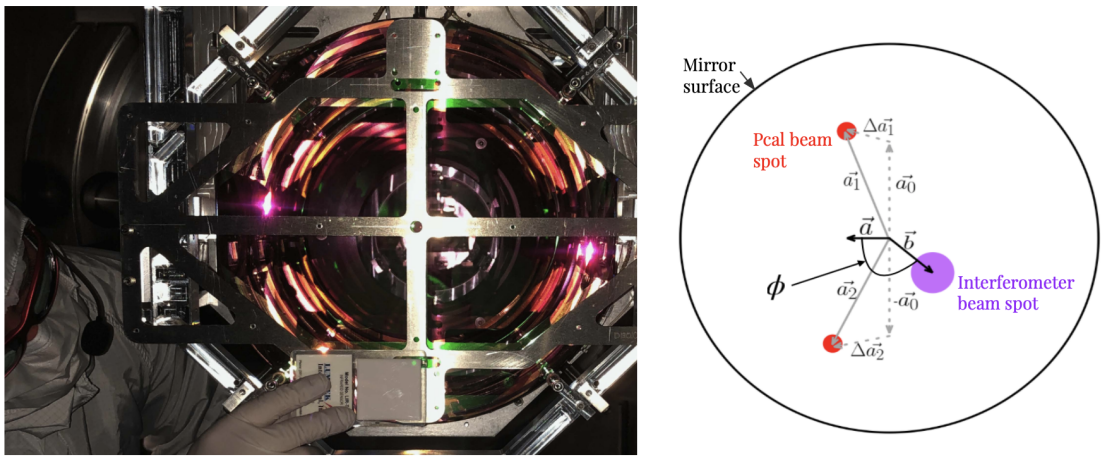

Figure 7.5. *Left image*: Alignment of Pcal beams using a target mounted to the suspension frame of the ETM. *Right image*: Schematic diagram showing the Pcal beam spot positions and the interferometer beam spot position on the surface of the ETM.

the X-end ETM and 22 mm for the Y-end ETM. The uncertainty introduced by unintended rotation of the ETM, ϵ_{rot}, is proportional to $|\vec{a}||\vec{b}|\cos\phi$, where ϕ the angle between $\vec{a}$ and $\vec{b}$, see Figure (7.5). Since ϕ has equal probability of being any value between -π and π, we use a *sine wave*, or *U-shaped*, probability density function (Bendat and Piersol (2010)) to estimate the variance in $\cos\phi$. We treat it as a Type B uncertainty and it is estimated using Eqs. (6.12) and (7.2), $\epsilon_{rot} = Mab/(\sqrt{2}I)$. The values of the relative uncertainty estimates for both the X-end and Y-end stations at LHO are listed in Table 7.4. Because of these large interferometer beam position offsets, ϵ_{rot} was currently one of the largest sources of uncertainty for the LIGO Pcal systems.

Combining the factors discussed above, the displacement factors for each end station are calculated using Equation (6.24). They are listed together with their relative uncertainties in Table 7.5. The overall uncertainties are dominated by the uncertainties due to unintended rotation of the ETM, ϵ_{rot}, and uncertainty in the calibration of the end station power sensors, ρ_R. Still, the relative uncertainties of 0.53 % for the X-end and 0.45 % for the Y-end are smaller than the lowest values previously reported, 0.75 % (Karki *et al.* (2016)).

Table 7.4. Estimated uncertainties due to unintended rotation of the ETM induced by Pcal forces, ϵ_{rot}, together with contributing factors (indented), for the LHO interferometer during the O3 observing run.

Param	**LHO-X**	**LHO-Y**	**Units**
ϵ_{rot}	0.41 %	0.31 %	-
$\lvert\vec{a}\rvert$	2e-3	2e-3	m
$\lvert\vec{b}\rvert$	22e-3	29e-3	m
I_p	0.419	0.419	$\mathrm{kg\,m^2}$
I_y	0.410	0.410	$\mathrm{kg\,m^2}$
M/I_p	94.65	94.47	$1/\mathrm{m^2}$
M/I_y	96.68	96.50	$1/\mathrm{m^2}$

Table 7.5. Measured Pcal displacement factors, together with contributing factors (indented) and uncertainties, for the LHO interferometer during the O3 observing run.

Param	LHO X-end		LHO Y-end		**Units**	**Type**
	Values	$\mathbf{u_{rel}}$ **(%)**	**Values**	$\mathbf{u_{rel}}$ **(%)**		
X_X, X_Y	1.565e-14	0.53	1.578e-14	0.45	m/ct	C
$\cos\theta$	0.9884	0.03	0.9884	0.03	-	B
M	39.657	0.01	39.584	0.01	kg	B
ϵ_{rot}	-	0.41	-	0.31	-	B
ρ_R	1.068e4	0.33	1.061e4	0.33	ct/W	C
η_R	0.9942	0.04	0.9948	0.04	-	C

7.1.6. Combining X- and Y-end Pcal Calibration. The interferometer responds equally to variations in the length of either arm enabling us to compare the the Pcal calibrations at X- and Y-end stations. To compare the Pcal calibrations at the two end stations, periodic displacements with high SNR were induced at frequencies separated by 0.1 Hz by the X- and Y-arm Pcals as shown in the right panel in Figure 7.6. The Spectral Line Monitoring tool (Anders *et al.* (2013)) was used to perform 100 s long FFT measurements of the line amplitudes in the interferometer and Rx sensor output time series. The left panel of Figure 7.6 shows measured values of χ_{XY}, the Pcal end station calibration comparison factor.

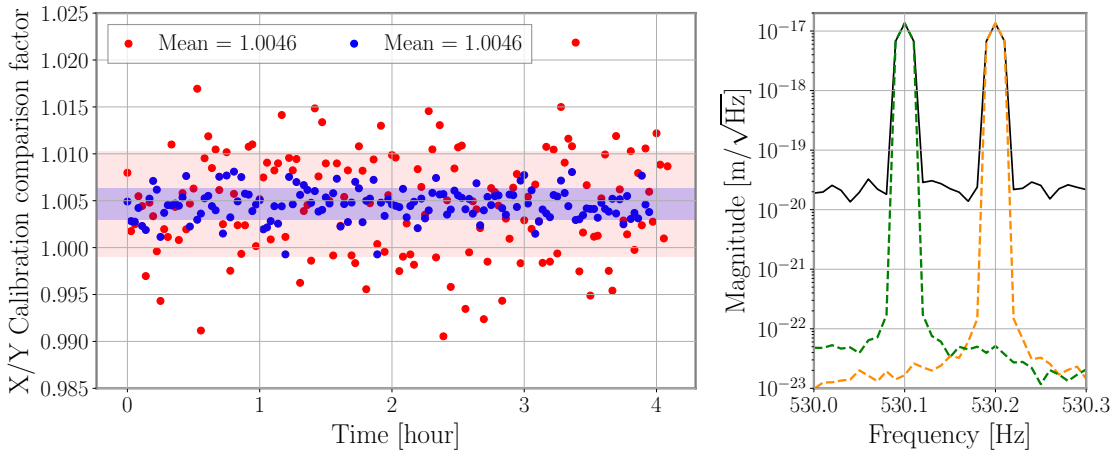

Figure 7.6. *Left panel*: χ_{XY}, the ratio of the amplitudes of the displacements reported by the calibrated X-end and Y-end Pcal Rx sensor signals, divided by the ratios of the amplitudes of the peaks in the interferometer output signal. The red points, for data recorded on February 3, 2020, are with the X-end excitation at 530.1 Hz and the Y-end at 530.2 Hz; the blue points, for data recorded on March 2, 2020, are with the X-end and Y-end excitation frequencies swapped and with the higher excitation amplitudes. The shaded regions are ± 1 standard deviation about the mean values. *Right panel*: Amplitude spectral density of the calibrated Pcal X-end (orange) and Y-end (green) Rx sensor outputs and of the interferometer output signal (black). The measurement bandwidth is 0.01 Hz.

It is the X/Y ratio of the amplitudes of the calibrated Pcal Rx sensor output signals, each normalized to the amplitude of the respective peak in the interferometer output signal. To ensure that the variation in the response of the interferometer did not impact the comparison over the 0.1 Hz frequency separation between the two excitations, the analysis was repeated with the frequencies of the X-end and Y-end excitations swapped. Increasing the excitation amplitudes for this second comparison reduced the variations in the measurement results. The measured value of χ_{XY} in both cases was 1.0046.

The contributions to the relative uncertainties in X from factors that are not common to both end stations (see Section 6.3.2) are 0.42 % for the X-end and 0.32 % for the Y-end. Thus the calculated relative standard uncertainty for the ratio of the displacement factors,

Table 7.6. Calculated X-end and Y-end combined displacement correction factors, C_X and C_Y, together with χ_{XY}, μ_g, and the non-common factors contributing to end station displacement factor uncertainty (indented), and their uncertainties, for the LHO interferometer during the O3 observing run. For Type A uncertainties, the number of measurements is noted in parentheses.

Param	LHO X-end		LHO Y-end		**Unit**	**Type**
	Values	**u_{rel} (%)**	**Values**	**u_{rel} (%)**		
C_X, C_Y	1.0029	0.25	1.0017	0.25	-	C
χ_{XY}	1.0046	0.01 (148)	1.0046	0.01 (142)	-	A
μ_g	1.003	0.25	Common with X-end		-	C
$\cos\theta$	0.9884	0.03	0.9884	0.03	-	B
M	39.657	0.01	39.584	0.01	kg	B
ϵ_{rot}	-	0.41	-	0.31	-	B
α_{RW}	-0.7209	0.042 (8)	-0.7157	0.014 (12)	-	A
ζ_W	1636.9	0.002 (8)	1637.6	0.002 (9)	ct/V	A
η_R	0.9942	0.04	0.9948	0.04	-	C
ξ_{EL}	0.9986	0.040	0.9986	0.040	-	C

X_X/X_Y, is 0.52 %, which is the quadrature sum of 0.42 % and 0.32 %. The measured value of 1.0046 for χ_{XY} is thus a $\sim 0.9\,\sigma$ result i.e. the probability of getting a value of 1.0046 or less is 63.2%.

The formalism for calculating the combined end station displacement factors is detailed in Section 6.3.2. The weighted geometric mean of 1 and 1.0046 is calculated, and its relative uncertainty, using the inverse of the squares of relative standard uncertainty of 0.42 % and 0.32 % as weights for X_X and X_Y. The values of the combined displacement correction factors, C_X and C_Y calculated using Equation (6.30), together with χ_{XY}, μ_g and the non-common factors contributing to end station displacement factors, are listed in Table 7.6 with their relative uncertainty estimates.

Table 7.7. Measured *combined* displacement factors, X^c, together with contributing factors (indented) and uncertainties, for the LHO interferometer during the O3 observing run. For Type A uncertainties, the number of measurements is noted in parentheses.

Param	LHO X-end		LHO Y-end		**Unit**	**Type**
	Values	$\mathbf{u_{rel}}$ **(%)**	**Values**	$\mathbf{u_{rel}}$ **(%)**		
X_X^c, X_Y^c	1.561e-14	0.41	1.581e-14	0.41	m/ct	C
ρ_G	-8.0985	0.315	Common with X-end		V/W	C
α_{WG}	1.1172	0.01 (38)	Common with X-end		-	A
ξ_{LN}	1.0020	0.070	Common with X-end		-	C
C_X, C_Y	1.0029	0.25	1.0017	0.25	-	C

The combined displacement factors, X_X^c and X_Y^c, calculated using Equation (6.26) and their relative uncertainties are listed in Table 7.7. The uncertainties for these combined displacement factors have been estimated by summing the correction factor uncertainties, 0.25 %, in quadrature with the uncertainty of 0.32 % resulting from factors that are common to both end stations, ρ_G, α_{WG} and ξ_{LN}. The overall uncertainties of 0.41 % for the combined displacement factors are smaller than those for the displacement factors for each end station, 0.53 % for X_X and 0.45 % for X_Y. This reduction results from combining the calibrations from both end stations using the measured X/Y comparison factor, χ_{XY}. This lowers the uncertainty contributions from sources that are not common to both end stations from 0.42 % for X-end and 0.32 % for Y-end to 0.25 % for both C_X and C_Y.

7.2. PCALS IN O4

Since the completion of the Advanced LIGO's O3 run, efforts have been ongoing to get ready for the next observing run, O4, which is slated to begin in August 2022. One of the major interferometer upgrades planned at LHO for O4 is to replace the interferometer mirrors to minimize the impact of point defect in the mirror coatings (Brooks *et al.* (2020)). This upgrade may allow interferometer beam to be nominally positioned much closer to the

center of the optics than it was during O3. This implies the 0.41% and 0.31% uncertainty due to unintended rotation for the X-end and the Y-end respectively be might also be reduced significantly. If this is the case, the dominant factor limiting the precision with which the Pcal-induce displacements can be estimated will be the power sensor responsivity calibration factor, ρ_R. The uncertainty associated with ρ_R is 0.32% which was mostly dominated by the 0.315% uncertainty on the GS calibration reported by NIST.

7.2.1. Bilateral Comparison. In 2009, several national metrology institutes (NMIs) undertook a key comparison of their respective optical power calibration capabilities and have prepared a comprehensive study reported in (Kück (2010)). Relevant for LIGO are measurements made at 1064 nm (close to Pcal laser wavelength of 1047 nm) which seem to indicate that there are large discrepancies between the results from the different laboratories due to systematic differences in the absolute calibrations. The observed variations in the calibrated responsivity of two thermopile-based power meters are as large as 3.5% between the NIST and other NMIs.

The results of this study using thermal power sensors motivated a bilateral comparison study of the responsivity of a Pcal transfer standard. A spare WS (WSS) was sent alternately to NIST and Physikalisch-Technische Bundesanstalt (PTB) in Braunschweig, Germany for this study. Results of the NIST versus PTB study can be found in (M Spidell *et al.* (2021)). The WSS was first sent to NIST in February, 2020 for calibration measurements, then to PTB, Germany in June, 2020 where again it was calibrated and eventually sent back to NIST in October, 2020 in compliance with the guidelines laid out in (WG-KC (2019)).

Both laboratories used a 1047 nm laser provided by LIGO and performed calibration measurements at 100 mW and 300 mW. NIST and PTB measurement laboratories were maintained at different temperatures 20.6° and 21.5°, respectively. The measured responsivities were adjusted to the PTB temperature result. Thus the PTB measurement gives the reference responsivity. Measurements at NIST are treated as trials. Once the laboratory

weights were established according to the procedure described in (WG-KC (2019)), a key comparison reference value (KCRV) was calculated. It is given by

$$\Delta_{KCRV} = \sum_{i=0}^{N} w_i \Delta_i \tag{7.5}$$

where Δ_{KCRV} is the weighted relative difference between the reference value reported by the pilot laboratory (PTB) and a consensus value (CV). Δ_i is the relative difference from the reference value reported by the i-th NMI. w_i is the laboratory weight, which includes the uncertainty reported by the NMI along with an additional uncertainty arising from those components such as changes in the power sensor due to transportation (if identified) and different measurement conditions between the PTB and NIST laboratories that affected comparison results (if applicable). The notations used in this section are same as the notation used in Appendix B of (WG-KC (2019)). The CV is given by

$$CV = (1 + \Delta_{KCRV}) S(\text{pilot}) \tag{7.6}$$

where $S(\text{pilot})$ is the reference responsivity reported by PTB. Finally, the bilateral degree of equivalence (DoE) which is the relative variation of the reponsivity reported by PTB and NIST is calulated from the CV. The bilateral DoE between PTB and NIST and the uncertainty on the DoE are given by

$$\begin{aligned} D_{PTB,NIST} &= \Delta_{PTB} - \Delta_{NIST} \\ U_{PTB,NIST} &= k\sqrt{u^2(\Delta_{PTB}) + u^2(\Delta_{NIST})}; k = 2 \end{aligned} \tag{7.7}$$

where $u(\Delta_i)$ is the average of the uncertainty reported for the 100 mW and the 300 mW measurements for the i-th NMI, i = PTB, NIST.

Table 7.8. Bilateral DoE between NIST and PTB and the uncertainty on the DoE.

Power (mW)	DoE (%)	U (k=2)
100	-0.07	0.95
300	-0.23	0.95
composite	-0.15	0.95

The DoE calculations using Equation (7.7), show the bilateral DoE to be much lower than the comparison uncertainty, indicating that uncorrelated systematic error falls well below the uncertainty level.

The optical power scale realization by NIST and PTB is adequate, which enabled achieving an overall uncertainty of 0.41% for LIGO Pcals.

7.2.2. Implications for O4. Realizing the important role laser power sensor calibration plays in the scientific impact of gravitational wave detections, there is increased interest and activity within the NMI community to improve power sensor calibration accuracy and precision. Scientists at NIST are developing a new generation of primary calibration standards that uses bolometers and carbon nanotube absorbers (Vaskuri *et al.* (2020)) that are expected to have significantly lower uncertainties than 0.315% for the standards currently being used. Eventually similar sensors may prove suitable for locating inside the vacuum envelope where several sources of uncertainty would be mitigated, providing laser power calibration directly traceable to SI units in-situ (Lehman (2020)). These developments at NIST should enable reducing the Rx sensor power calibration factor to $\sim$ 0.1% from 0.32%.

Assuming that during O4 the Rx sensor power calibration factor will indeed be $\sim$ 0.1%, and also assuming that after the upgrade of the interferometer mirrors, the maximum interferometer beam position offset reduces to 10 mm from 29 mm for the X-end and 22 mm for the Y-end station, the uncertainty in combined Pcal displacement factors could reduce to

$\sim 0.16\%$ from the O3 level of 0.41%, provided the optical efficiencies and the uncertanties remain similar. Thus, reducing the NIST calibration uncertainty is expected to significantly improve the accuracy with which we can estimate the Pcal-induced displacement fiducials.

8. MULTI-MESSENGER ASTRONOMY AND SKY LOCALIZATION

On August 17, 2017, LIGO and Virgo observed a BNS inspiral signal (Abbott *et al.* (2017c)). Two space-based instruments, the Gamma-ray Burst Monitor (GBM) on board Fermi (Goldstein *et al.* (2017)), and the spectrometer anti-coincidence shield (SPI-ACS) on board INTEGRAL (Savchenko *et al.* (2017)) detected the short gamma-ray burst (sGRB) GRB 170817A 1.7 seconds later. This was the first time an event was observed jointly in GW radiation as well as EM radiation.

Besides compact binary mergers, other transient GW sources that may generate neutrino and EM radiation include the core-collapse of massive stars, GRBs, SN explosions, magnetars. GRBs and SN explosions are expected to produce relativistic outflows of high-energy neutrinos (Bustamante *et al.* (2015); Janka (2017)). Another class of transient GW sources which may be observed with other cosmic messengers are magnetars, i.e., rotating NSs with very high magnetic fields ($\sim 10^{-3}$ G) that may emit GWs when undergoing starquakes (Corsi and Owen (2011)).

8.1. MULTI-MESSENGER ASTRONOMY

Multi-messenger Astronomy (MMA) enables astronomers to probe the sources that emit GWs by extracting information on their different properties and their environments. Various cosmic messengers include EM radiation, GWs, neutrinos and cosmic rays (Szczepanczyk (2018)). GW signals provide information about the physical properties of their sources such as masses, inclinations, orientations and spins. The EM and neutrino counterparts provide information about the progenitor environment, the formation of relativistic and non-relativistic outflows, and the equation of state of matter. Moreover, the detection of an EM counterpart to a GW detection may also enable identification of the

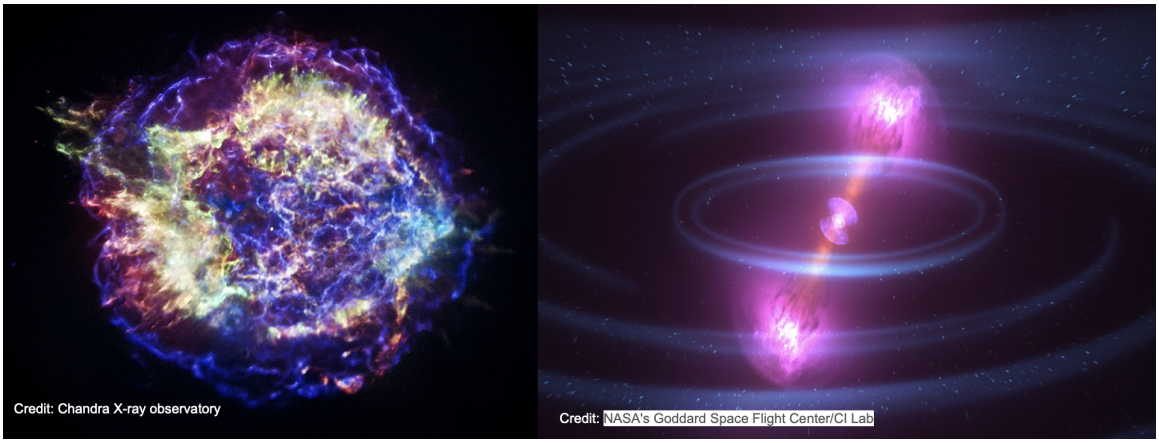

Figure 8.1. Two examples of multi-messenger sources. *Left*: A composite photo of CCSN taken from Chandra X-ray observatory *Right*: An artist's depiction of a BNS merger generating GWs accompanied by an EM counterpart.

progenitor host of the GW source. For CBC sources, the distance estimated from the GW data, together with the measured redshift of the host galaxy, may allow for an independent measurement of the Hubble constant (Abbott *et al.* (2019d)).

As for SN sources, detection of neutrinos along with GW radiation may provide insights on the explosion mechanism and its physics, enable better constraints on the timing of the collapse, and better sky localization (Szczepanczyk (2018)). MMA with CCSN would be the subject of the remainder of this dissertation.

8.2. MULTI-MESSENGER ASTRONOMY WITH CORE COLLAPSE SUPERNOVAE

Core collapse supernovae (CCSNe) are the violent explosions of massive stars (above $8M_{\odot}$) and are believed to form most of the BHs detected by Advanced LIGO and Advanced Virgo. Although multiple mechanisms for CCSNe have been proposed, the model based on neutrino driven explosion mechanism are the most widely considered. In the remainder of this section we will briefly discuss this mechanism. We will follow Couch (2017).

Towards the end of their lives, massive stars go through multiple epochs of core and shell burning of heavier elements to finally form iron cores. The core is supported by electron degeneracy pressure, strongly cooled via neutrinos, and surrounded by burning shells of Si, O, C and other elements. In this phase, the Si shell burning continues to add to the star iron core until the latter reaches the Chandrasekhar mass limit ($1.4M_{\odot}$). Once the mass of the iron core exceeds this limit, the core begins to collapse. The collapse accelerates rapidly driven mainly by two processes, photodissociation of iron-peak nuclei and electron capture, which reduce the electron degeneracy pressure support. The collapse of the core results in higher core densities and temperatures which increase the rate at which the electron capture process occurs. This reduces the electron degeneracy pressure support, thus creating a runaway process.

The inner part of the core, about $0.4 - 0.6M_{\odot}$, proceeds to collapse until the central density exceeds that of nuclear matter density, at which point the repulsive strong nuclear force causes the equation of state to stiffen. The collapse of the inner core stops suddenly, initiating a strong shock wave into the still collapsing outer core, referred to as core *bounce*. The shock initially propagates outwards rapidly through the outer core, but strong neutrino cooling and photodissociation of iron-peak nuclei use up most of the energy liberated by the collapse of the inner core, stalling the shock to a radius of $\sim$ 150 km. At this stage, the inner core is made mostly of neutrons and regains quasi-hydrostatic equilibrium. This whole process from iron core collapse to bounce takes a fraction of a second to complete. The collapse liberates an enormous amount of energy, most of which is radiated in the form of neutrinos.

If a small yet sufficient fraction of this radiated energy is reabsorbed by the post-shock plasma, the shock is reinvigorated, resulting in an explosion (Colgate and White (1966)). This prompt neutrino-driven mechanism works for only the lowest-mass progenitors, often

associated with the electron capture CCSN explosion. Bethe and Wilson (1985) showed that neutrino-driven explosions could also result at relatively 'late' times, a few hundred milliseconds following the bounce.

More recently, several studies have sought to explore the observable properties of the neutrino mechanism. For example, O'Connor and Ott (2011) explored the dependence of the BH formation time on the structure of the progenitor; they showed that more compact cores collapse to BHs sooner than the less compact ones in failed explosions. Another study by Ugliano *et al.* (2012) found that the neutrino mechanism, when appropriately parametrized, can roughly reproduce key observable features of CCSN populations, such as remnant mass distributions, including the mass gap between NSs and BHs.

8.3. SKY LOCALIZATION IN MULTI-MESSENGER ASTRONOMY

This section provides a brief discussion on sky localization from timing and coherent network analysis.

Issuing rapid GW early warnings with accurate localizations is considered to be the key for MMA. Once the GW event candidates have been validated, they are communicated to the astronomical community via Gamma-ray Bursts Coordinates Network (GCN) notices in a time frame of tens of minutes. Each GCN notice include a preliminary sky localization of the GW source candidate. Improved sky localization estimates are provided at a later time for follow-up studies.

At sky locations other than the correct location, the requirement of signal consistency reduces the reconstructed network SNR. Moreover, GW sources are assumed to be distributed almost uniformly in volume and the orientation of merging binaries are also assumed to be uniformly distributed. Hence, most of the sources are expected to be observed close to face-on, with high SNR, and at large distances (Fairhurst (2018)). This could be used to discard some of the degeneracies in sky location. For example, at positions away from the true location, the observed SNRs will not be entirely consistent with the signal and

the reconstructed orientation of the source will be increasingly edge-on (Fairhurst (2018)). Incorporating amplitude and phase consistency between sites because GWs comprise of two polarizations and imposing reasonable astrophysical priors on the source distribution allows us to localize the vast majority of sources to a single patch in the sky.

As mentioned before, using the time delay between two detectors a circle of possible source positions on the sky can be reconstructed, centered on the ideal line joining the two detectors sites. Adding another detector, three circles, one for each couple can be reconstructed. In this case, the intersection points of these circles correspond to the source locations, one above and the other below the plane defined by the locations of the detectors, thus improving the sky localization as shown in Figure 8.2. For example, despite Virgo's lower sensitivity during O2 observing run compared to the two LIGO detectors, the inclusion of data from Virgo improved sky localization significantly. This is exemplified by the LIGO–Virgo detections GW170814 and GW170817. GW170814 the first three-detector observation of GWs from a compact binary merger, was localized to $1160\,\mathrm{deg}^2$ at the 90% credible level with only the two LIGO detectors. The inclusion of Virgo reduced this area to only $60\,\mathrm{deg}^2$ (Abbott *et al.* (2017d)). For the BNS merger GW170817 the addition of data from Virgo reduced a $100\,\mathrm{deg}^2$ sky localization reported with only two LIGO detectors to roughly $30\,\mathrm{deg}^2$ (Abbott *et al.* (2017e)), enabling the swift identification of the EM transients and host galaxy (Soares-Santos *et al.* (2017)).

However, from timing information alone, it is not possible to distinguish between the two sky locations. If coherent localization is considered along with the timing information, it is, in principle, possible to distinguish between these positions. In the "mirror" sky location, the observed amplitudes and phases of the signal will generally not be consistent with a GW signal comprising of two polarizations, thereby reducing the network SNR and allowing us to reject that particular position. To obtain a single sky patch at 90% confidence for a signal of SNR 12, there must be a difference in SNR of 0.25 or greater between the true and mirror position (Fairhurst (2018)).

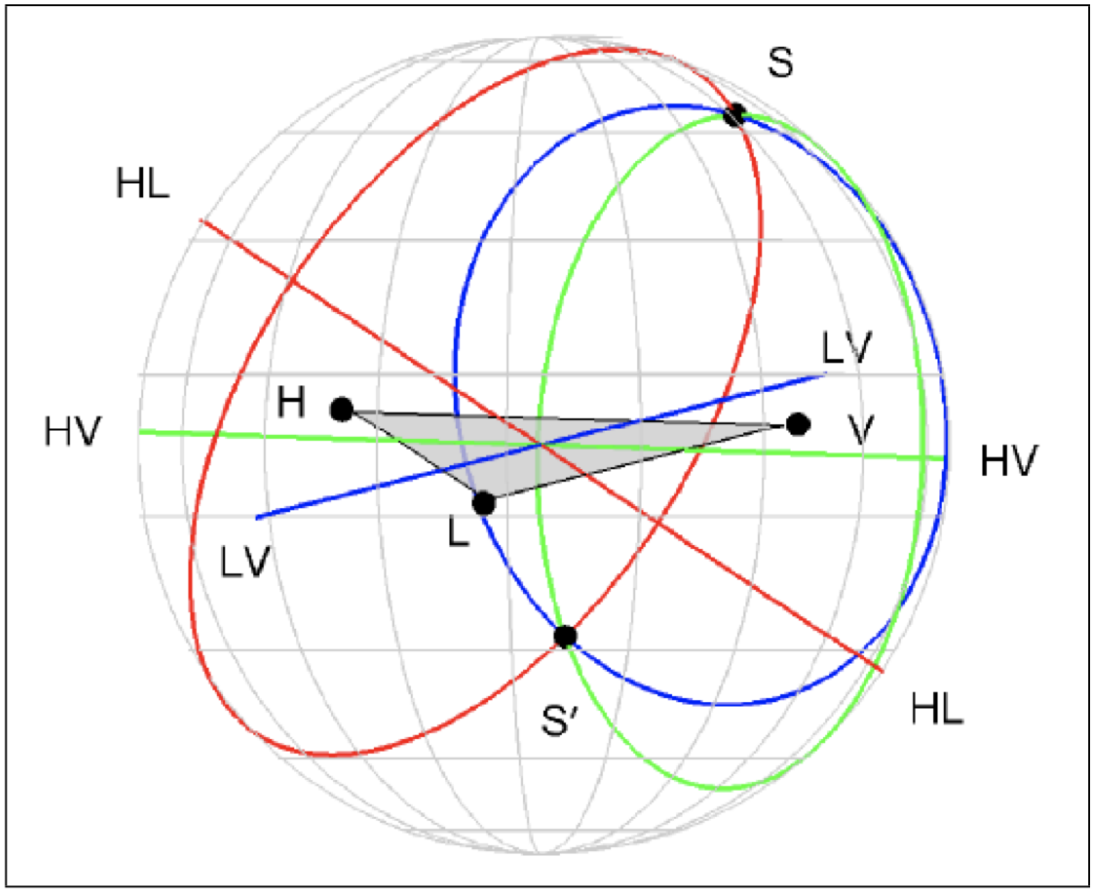

Figure 8.2. Sky localization with three detectors. The three rings denote the sky localization achieved by a network of two ground-based GW detectors, Hanford-Livingston (HL, in red), Livingston-Virgo (LV in blue), and Hanford-Virgo (HV, in green). Using all three detectors resolves the ring to two locations S and S' above and below the plane defined by the HLV network.

Although the areas enclosing 90% probability span several square degrees, with KAGRA and LIGO India joining the LIGO-Virgo network, timing information alone will be sufficient to localize the source to a single sky region. In the next section we look at the sky localization reported by a coherent network analysis algorithm cWB for LIGO-Virgo network. In Subsection 8.4, we focus on specifically on the tools, plots and parameters generated by cWB used in this study.

8.4. SKY LOCALIZATION WITH CWB

cWB's likelihood function depends on the antenna pattern, i.e., its value varies according to the direction of the source in the sky. To determine the most likely location for the GW source, cWB calculates the likelihood for all the sky positions, ranks the results, and assigns the source to the direction with the highest likelihood. For each reconstructed event, each sky position is ranked on the basis of sky statistic: the larger the sky statistic over a given sky region, the higher the probability that the source is localized within the considered region. Examples of two skymaps showing the sky statistic are shown in Figure 8.3. The color scale denotes the probability of finding the source in a given sky location.

The information about the reconstructed event is saved in a human friendly format called Coherent Event Display (CED) report (Klimenko *et al.* (2021)). A complete description of all the reconstructed parameters that are included in the CED report can be found in the CED Technical Documentation (Mercer and Klimenko (2008)). In the following subsections, we describe only those parameters and plots used in this study.

8.4.1. Sensitivity Skymap. The sensitivity of a network of k detectors is fully characterized by its noise-scaled antenna pattern vectors $|\mathbf{f}_+|$ and $|\mathbf{f}_\times|$

$$\mathbf{f}_{+(\times)} = \left(\frac{F_{1+(\times)}}{\sqrt{S_1}}, \frac{F_{2+(\times)}}{\sqrt{S_2}}, ..., \frac{F_{k+(\times)}}{\sqrt{S_k}} \right) , \tag{8.1}$$

where S_i and $F_{i+(\times)}$ are the power spectral density of the noise and the antenna patterns of the i-th detector, respectively. The power spectral density S_{net} of the network noise is defined as

$$S_{net} = \left(\sum_{i=1}^{k} S_i^{-1} \right)^{-1} . \tag{8.2}$$

In the dominant polarization frame, the overall network sensitivity depends on sky coordinates and is characterized by the effective power spectral density of the network noise (Klimenko *et al.* (2001))

$$N_{net} = (|\mathbf{f}_+|^2 + |\mathbf{f}_\times|^2)^{-1} . \tag{8.3}$$

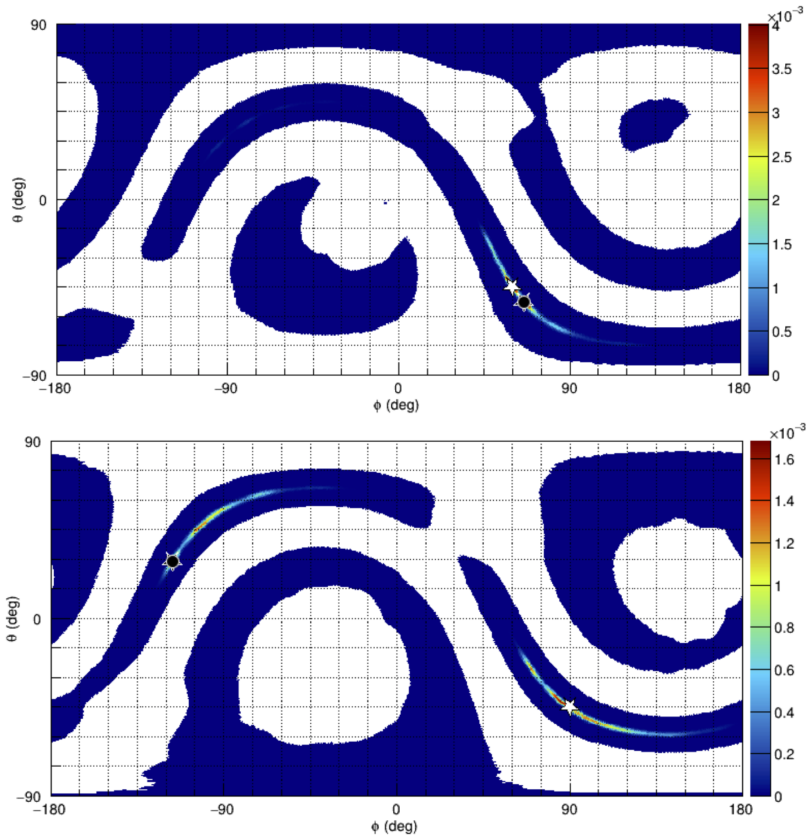

Figure 8.3. Two examples of skymaps showing the sky statistic as a function of Earth-fixed sky coordinates. The white star denotes the true sky location of the GW source. The black star denotes the most likely reconstructed sky location. In the upper panel the reconstructed sky position is close to the true sky location. In the lower panel the “mirror" position is mistakenly ranked as the most likely sky location of the source. The sky statistic is represented by the color scale, with red denoting the highest probability of finding the source while blue denoting the lowest probability.

The effective power spectral density of the network noise can be factorized into a sky-dependent factor, $\mathcal{F}$, and a sky-independent factor, S_{net}:

$$N_{net} = \mathcal{F}^{-2} S_{net} \,, \tag{8.4}$$

where $\mathcal{F}$ is the network antenna factor normalized to 1. An example of the cWB sensitivity plot included in the CED report is shown in Figure 8.4.

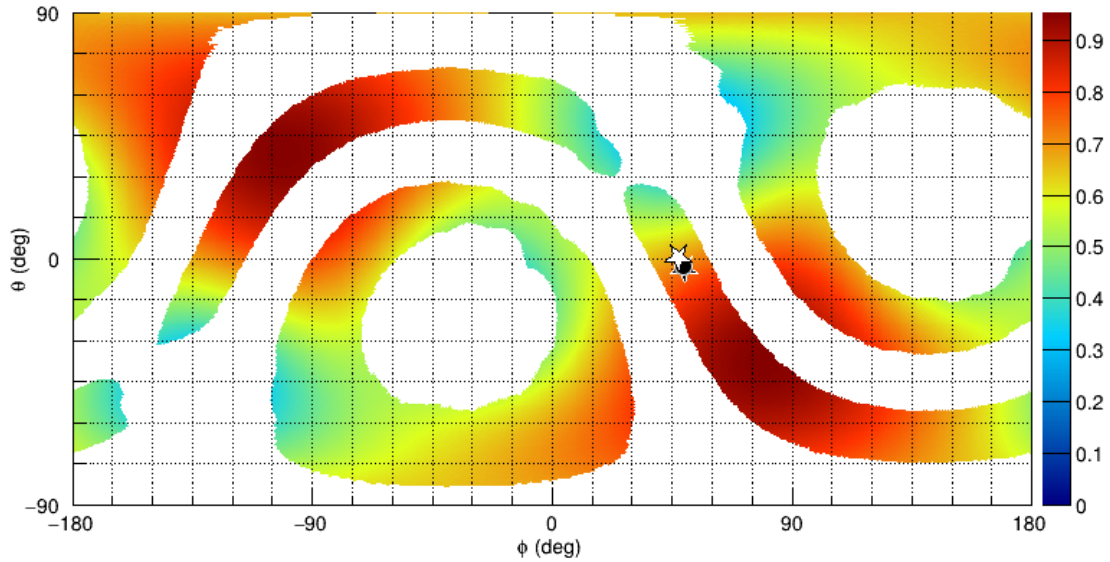

Figure 8.4. Network antenna pattern in Earth-fixed coordinates as generated by cWB. The color denotes the network sensitivity, red being the highest sensitive region and blue being the lowest sensitive. As before, the white star denotes the injected sky location whereas the black star denotes the reconstructed sky location.

8.4.2. Probability Skymap. Figure 8.5 shows an example of the probability distribution of sky localization. To create a sky map, cWB uses the Hierarchical Equal Area isoLatitude Pixelization of a sphere, HEALPix (Górski *et al.* (2019)). The sky is segmented into 196608 pixels each corrsponding to an area of $0.65\,\mathrm{deg}^2$. Each pixel is assigned a source location probability, represented in a color scale. The data used to generate the probability skymap is stored in a *probability.FITS* file.

8.4.3. SNR. The CED report also provides information on the network SNR of the reconstructed event. Under the assumption that $\mathbf{f}_+$ and $\mathbf{f}_\times$ do not vary much in the signal frequency band, the network SNR in the dominant polarization frame (Klimenko *et al.* (2005)) is

$$\rho_{net} = \sqrt{|\mathbf{f}_+|^2(h_+|h_+) + |\mathbf{f}_\times|^2(h_\times|h_\times)}\,, \tag{8.5}$$

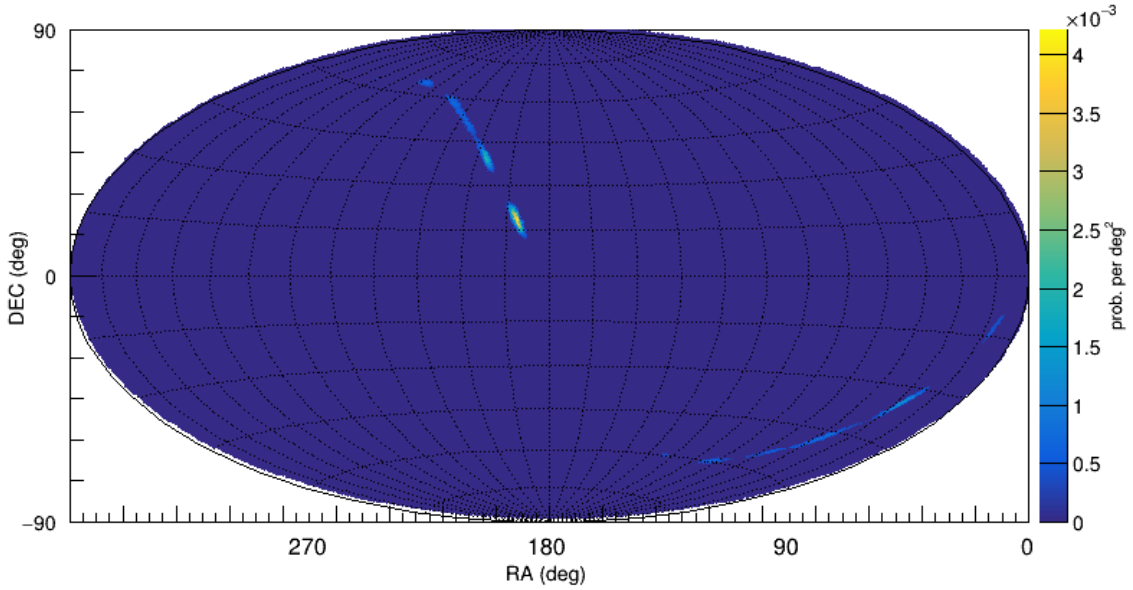

Figure 8.5. Example of a probability skymap for a CCSN event generated by cWB. Here $\theta = -90°$ is the South Pole, $\theta = 90°$ is the North Pole and $\theta = 0°$ is the Equator. Angle ϕ goes from $-180°$ to $180°$ with $0°$ signifying the Greenwich meridian and increases in the East direction.

where $(h_{+(\times)}|h_{+(\times)})$ denote the inner product of the plus (cross) polarization amplitudes with themselves.

In coherent network analysis, a likelihood ratio is defined by

$$\Lambda(\mathbf{x}, \Omega) = p(\mathbf{x}|\mathbf{h}(\Omega))/p(\mathbf{x}|0)\,, \tag{8.6}$$

where $\mathbf{x}$ is the network data, $p(\mathbf{x}|0)$ is the joint probability that the data only contains instrument noise and $p(\mathbf{x}|\mathbf{h}(\Omega))$ is the joint probability that a GW signal h with source parameters Ω is present in the data. In the cWB searches for unmodeled burst signals, the best matching waveform to the data is found by varying the likelihood ratio over a set of unknown GW waveforms $\mathbf{h}$ (Klimenko *et al.* (2001)). The network SNR is calculated using Equation (8.5) from the reconstructed waveform.

In order to quantify the impact of overall calibration errors on the reconstructed cWB sky localizations, we either directly use the quantities discussed in this section or define new parameters derived from them. The next section describes those parameters along with the methodology and the results of our quantitative study.

9. EFFECTS OF CALIBRATION ERRORS ON BURST-LIKE OBJECTS.

This section describes a study to quantify the impact of overall calibration errors (CE) on sky localizations of GW signals from CCSN sources using one of the LVK detection pipelines, cWB (Drago *et al.* (2020)).

In the following sections, we will discuss the motivations for this study and the CCSN waveform models used. We have already discussed sky localizations of the GW sources with cWB in the last section.

9.1. MOTIVATION

As mentioned in Section 7, Pcals are used to calibrate the LIGO detectors. Unaccounted or unknown systematic errors in the Pcal calibrations lead to inaccurate physical information being extracted from the signals. In this analysis, we study the impact of $\pm 10\%$ and $\pm 5\%$ errors on the sky localizations of simulated GW signals from CCSN. Since the Pcals enable the determination of the DARM displacement, the CEs are simulated by multiplying the strain data (including the signal and the noise) of one of the detectors by a constant factor. Without loss of generality in the following we apply the CE factors to the LIGO Hanford data.

9.2. CCSN WAVEFORMS

In Section 8.2 we briefly discussed the CCSN explosion mechanism and the associated GW signals. The GW waveforms depend on the theoretical model. For each of these models, there are multiple CCSN waveforms based on the GW emission mechanisms, progenitor mass and other parameters (Szczepanczyk *et al.* (2021)). Here we briefly discuss the two of these waveforms used for this study.

9.2.1. Mueller 2012 Waveform. This waveform is based on a theoretical model of post-bounce evolution in a neutrino-driven explosion (Mueller *et al.* (2012)). The GW signatures are dominated by low-frequency ($\sim$ 100 – 500 Hz) convective matter motion. The waveform model is a three-dimensional simulation for a non-rotating 15$M_\odot$ progenitor star. The approach used to calculate the waveform is outlined in Janka and Mueller (1996). Both the plus and cross polarizations are available for this waveform.

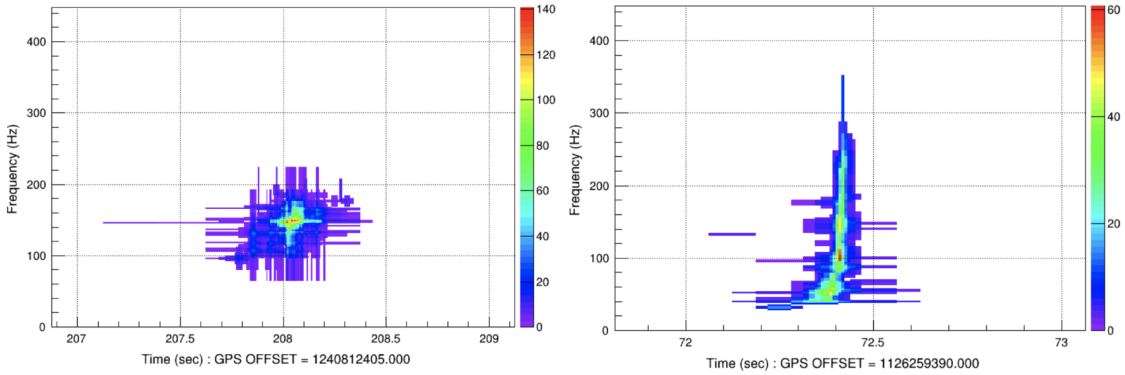

Figure 9.1. *Upper panels*: Time-frequency plot for a Mueller 2012 waveform which was used in this study (left) and for comparison the GW150914 BBH coalescence waveform (right). Most of the signal lies in the frequency band 100 – 200 Hz for the Mueller 2012 waveform, which is in the most sensitive region of the interferometer. As for the BBH, the frequency ranges from 20 Hz to $\sim$ 300 Hz and demonstrates the typical chirp signature. Since in this analysis we are considering frequency independent CEs, reconstruction of sky localization of GW signals from BBH coalescences and burst signals are expected to get affected in the same way.

9.2.2. Kuroda 2017 Waveform. This waveform is based on a model of GW emission in the pre-explosion phase in CCSN. The GW signatures strongly depend on whether the post-shock flow is dominated by the standing accretion shock instability (SASI) or convection, and the g-modes (Kuroda *et al.* (2017)). Kuroda et. al. provided waveforms for two progenitor masses, 11.2$M_\odot$ and 40$M_\odot$. In the following study, we use the waveform model with the 11.2$M_\odot$ progenitor mass. Only one polarization is available for this waveform.

9.3. METHODOLOGY

In this section, we first describe the parameters that we use to quantify the impact of CEs on the sky localization accuracy. Then we discuss in detail the methods used in our analysis. The data used by cWB to create a skymap is contained in a probability.fits file. This file provides a list of pixel indices and their associated probability that the source is located within the pixel. Assuming that the sky is searched from regions of highest probability to lowest probability, we first rank the pixels from highest to lowest probability. We calculate the cumulative probability as a function of the number of pixels searched for the skymap when no CE was introduced, referred to as the *reference* probability function. Similarly for skymaps with CEs introduced into a detector data stream we calculate the *observed* probability function. We also calculate the cumulative probability by summing the reference probability when the pixels are ordered according to the skymap with CE, referred to as the *real* probability function. We define the difference between the observed cumulative probability and the real cumulative probability as the *searched probability deficit* (SPD).

The upper panel of Figure 9.2 shows the cumulative probability as a function of the number of pixels for the reference, observed and the real map for a Mueller 2012 waveform injected at GPS time 1240812613 (06:09:55 UTC on May 02, 2019). A CE factor of 0.9 was applied to the Hanford data. It was injected at Earth-fixed coordinates ($\phi = 0°, \theta = 15.47°$) and at a distance of 1 kpc. From the plot, we see that if there is a -10 % CE in the Hanford data, a survey of the first n pixels starting from the pixel with highest probability will account for a little less than the sky localization probability in the case of no CEs. Thus the reconstructed source localization worsened due to CE. The lower panel of Figure 9.2 shows the SPD as a function of the observed probability for the same case discussed above. From the figure, we can conclude that for example, the first $\sim$ 4000 pixels only accounts for 80 %

of the sky localization probability instead of $\sim 83.75\,\%$ for no CEs, which again indicates the source localization worsened in presence of the CE. This is an example where the sky localization is not significantly changed due to CE.

Similarly, Figure 9.3 shows an example where Mueller 2012 waveform was injected at Earth-fixed coordinates ($\phi = 279°, \theta = 41.81°$) and at a distance of 1 kpc. As before, a CE factor of 0.9 was applied to the Hanford data. This is an example where the source localization is inaccurately reconstructed by cWB.

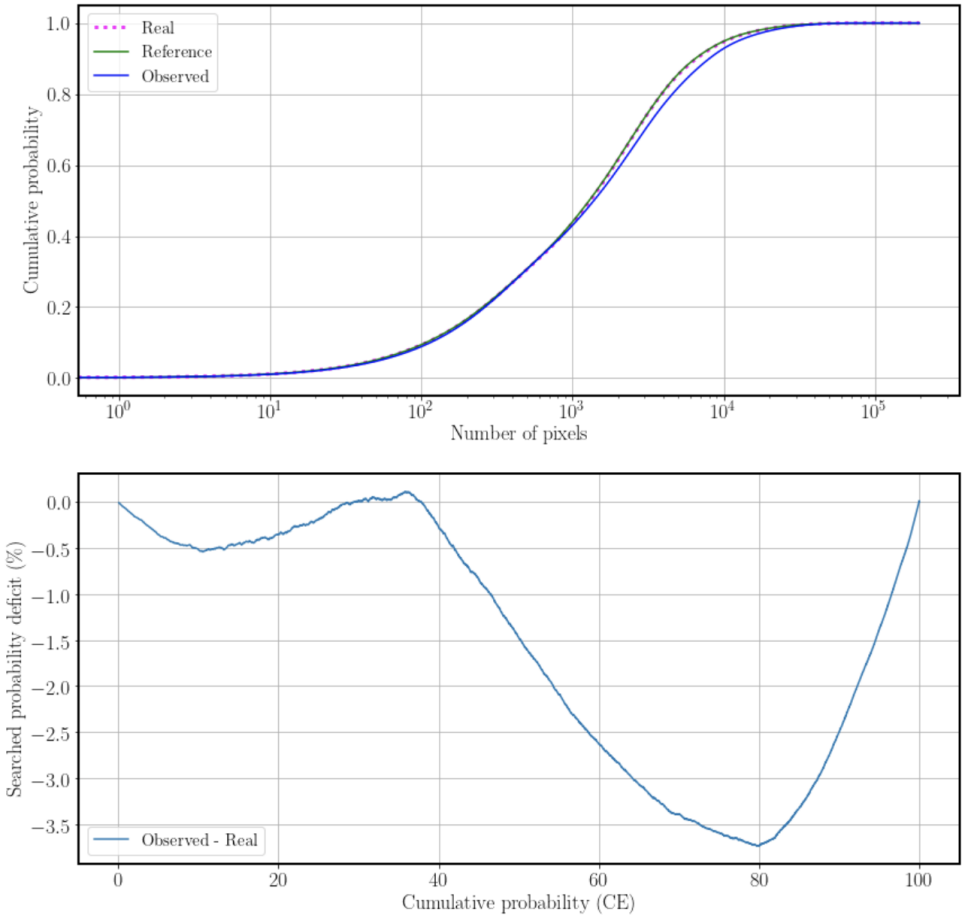

Figure 9.2. *Upper panel*: Cumulative probability versus the number of pixels for the skymap without CE (Reference) and with CE-map (Observed). When the probability from the Reference map is summed according to the pixel ordering from Observed map, we obtain the Real map. CE factor of 0.9 is applied to Hanford data. *Lower panel*: SPD as a function of observed cumulative probability.

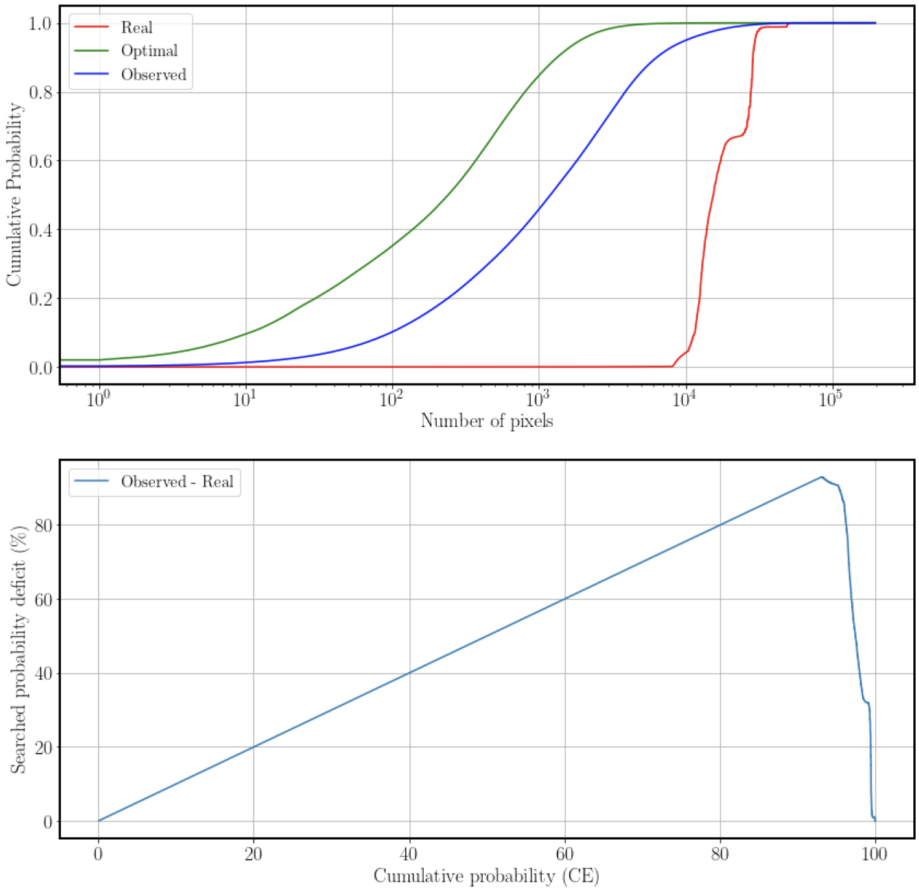

Figure 9.3. *Upper panel*: Cumulative probability versus the number of pixels for the skymap without CE (Reference) and with CE-map (Observed). When the probability from the Reference map is summed according to the pixel ordering from Observed map, we obtain the Real map. CE factor of 0.9 is applied to Hanford data. *Lower panel*: SPD as a function of observed cumulative probability.

The relative change in the searched sky area at a fixed confidence level is defined as $(A - \tilde{A})/A$ where A and $\tilde{A}$ are sky areas at the given confidence interval with no CE and with CE, respectively. It indicates the extra (or the deficit in) source localization area searched to find the source at a given confidence interval when there is a CE compared to the no CE. A positive error denotes that the source localization has improved in the presence

of a CE i.e., we can reach a fixed cumulative probability by searching a smaller sky area, whereas a negative error denotes that the skymap with CE gets delocalized i.e., we need to search a larger area to reach a fixed cumulative probability.

We injected Mueller 2012 SN waveform with a source orientation of $\phi = 120°$, $\theta = 51°$ into O3 data from all the LHV detectors at three hundred different sky locations. All injections are at a distance of 1 kpc with a polarization angle of $\psi = 30°$, and at GPS time 1240812613. This ensured that any change in the sky localization was purely due to CE and not due to changes in the detector noise floor or any other parameter.

We created dataframe file lists for each detector at the specific GPS time interval. We then multiplied the clean calibrated strain data of the LIGO Hanford detector by a CE factor and created new dataframes that could be used by the cWB algorithm. For the Livingston and Virgo detectors, the default dataframe files containing the clean calibrated strain data were directly used by cWB. In order to multiply the waveform in the Hanford data by the same scale factor we used the cWB plugin, CWB_Plugin_AmplitudeMisCal.C (Drago *et al.* (2020)). We also used data quality veto file lists containing the time periods to be excluded for each detector data as the interferometers were either not running in proper configuration or hardware injections were performed (Abbott *et al.* (2020a)).

The Mueller 2012 waveforms were injected at a distance of 1 kpc since for some sky locations the detection efficiency of cWB drops to less than $\sim 50\,\%$ beyond 1 kpc, as shown in the right panel of Figure 9.4. Detection efficiency as a function of the distance for two sky locations are shown as examples.

Figure 9.5 shows the three hundred sky locations at which the Mueller waveforms were injected. Since the cWB detection efficiency is not 100 % at a distance of 1 kpc, there were a few sky locations for which cWB was unable to recover the injections, marked in black cross in the Figure 9.5. There are 32 injections that cWB did not detect, i.e. at 1 kpc the detection efficiency of cWB for the Mueller 2012 waveform is $\sim 90\,\%$.

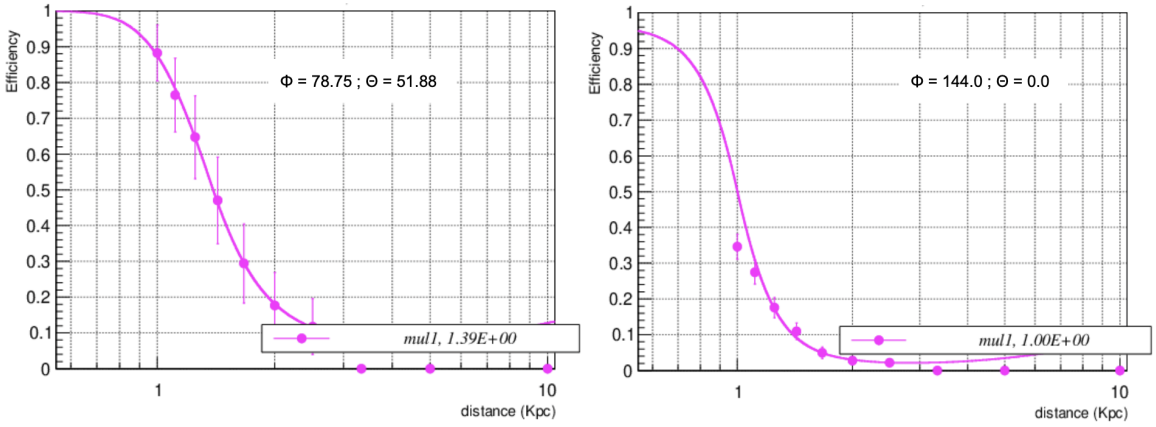

Figure 9.4. Detection efficiency of cWB algorithm as a function of the injected source distance for two different sky locations denoted by (ϕ, θ) in degrees for a Mueller 2012 waveform. The distance at 50 % detection efficiency is noted in the legend.

Usually injections reconstructed with high SNR (mostly $\geq$ 80) are analysed differently by cWB. This is because cWB sets a threshold of 100 for the total number number of TF pixels to be analysed. To save computation time for the events that exceed the threshold, the number of sky locations to compute the maximum likelihood ratio is reduced. Figure 9.6 shows two examples of network antenna pattern generated by cWB as a part of the CED report for high a high SNR event (upper panel) and a typical injection (lower panel). We removed any injection that demonstrated this dotted antenna pattern feature shown in the upper panel of the Figure 9.6.

9.4. RESULTS

For the recovered injections that pass our selection criteria in Figure 9.5, we calculated the SPD at 90 % cumulative probability and the relative change in the 90 % source localization area due to CE.

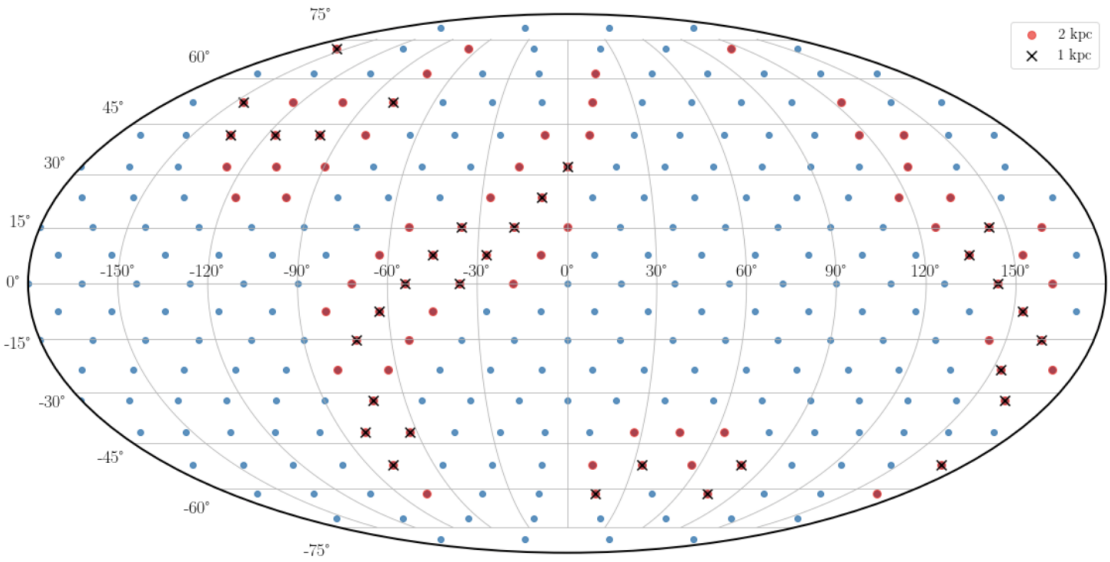

Figure 9.5. Mueller 2012 waveform injected at three hundred sky locations made at 1 kpc with polarization angle, $\psi = 30°$, at the same GPS time 1240812613. No CE have been introduced. The injections not detected by cWB are marked in black cross. The sky positions not detected by cWB when injected at a distance of 2 kpc, keeping all other parameters same, are marked in red dots. It includes the sky locations marked in black cross as well.

Figure 9.7 shows the histogram of the absolute value of the SPD at 90 %. The Y-axis indicates the fraction of the total number of source locations for which SPD yields positive (the distribution in blue) or negative (the distribution in orange) due to the presence of the CEs. From the inset of each panel in Figure 9.7, one can see that for some sky positions the SPD is significantly impacted when CEs are present in the data resulting in the spike above |SPD| = 0.75. For the CE factor of 0.9 these sky locations constitute $\sim$ 8 % of the total detected sky locations whereas for 0.95 it constitutes $\sim$ 4 %. In this case, when there is a CE of -10 % in the Hanford data, the reconstructed source location is such that the probability of finding a source in the 90 % confidence region is less than 15 %.

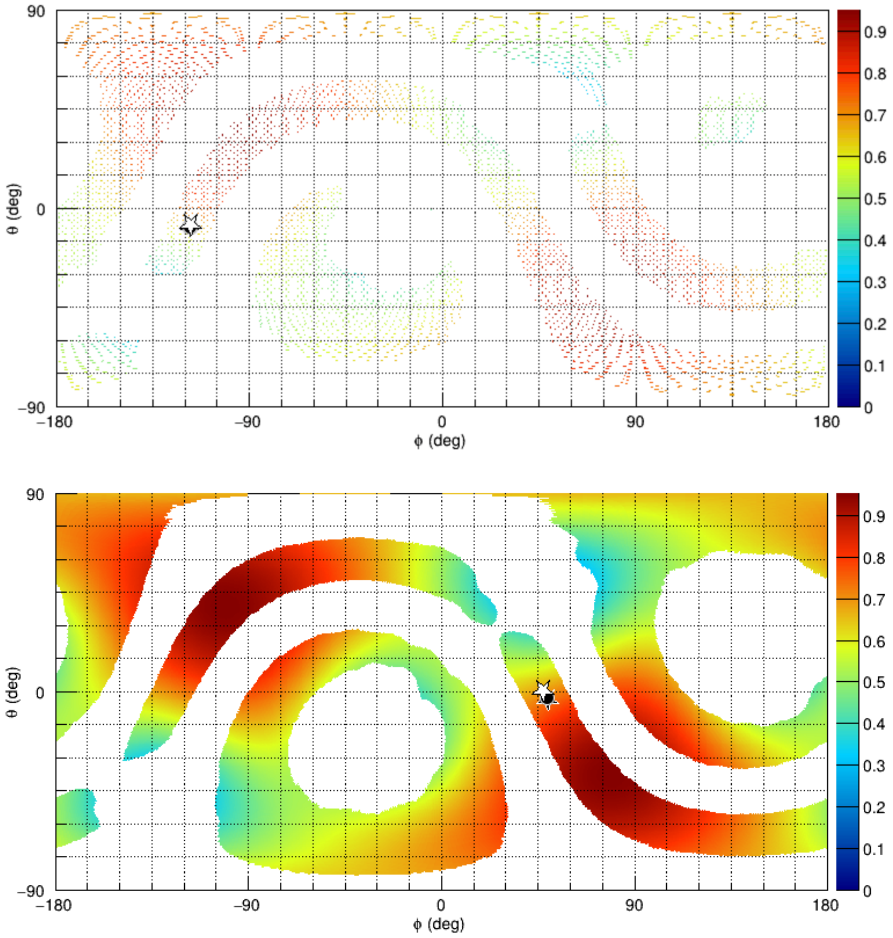

Figure 9.6. Network antenna pattern generated by cWB for a high SNR case and a typical case. *Upper*: Dotted network antenna pattern plot generated by cWB as a part of its CED report. These high SNR injections are analyzed in a different method than the usual to save computation time. They are treated as outliers and have been removed from the histogram plots in this section. *Lower*: Typical network antenna pattern plot by cWB.

Figure 9.8 shows the histogram of the absolute value of the relative change on the 90 % source localization area. The Y-axis indicates the fraction of the total number of source localizations that are improving (in blue) or worsening (in orange). From the Figure 9.8, one can see that for some sky positions the source localization worsens by a large factor, for example when CE of −10 % are present in the data the source localization worsens as high as ∼ 60 % resulting in the spike near $|(A - \tilde{A})/A| = 0.6$. Thus from Figure 9.7 and

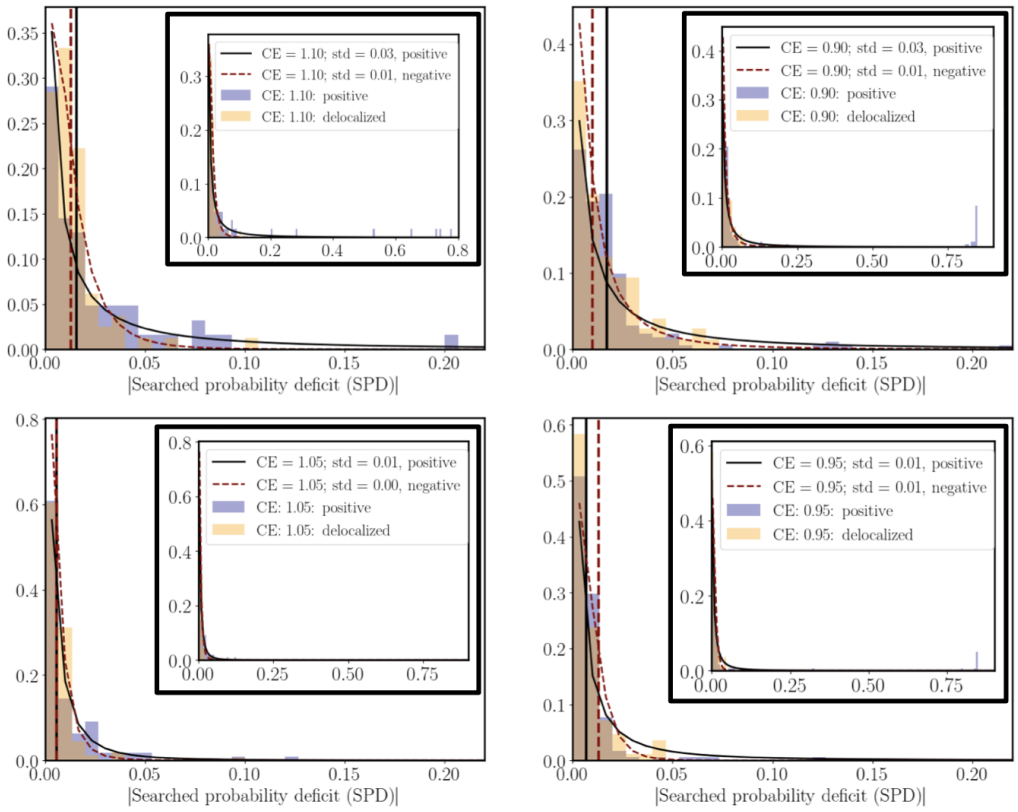

Figure 9.7. Histogram of the absolute value of the SPD at 90 % cumulative probability for all the detected injections with positive values (blue) and negative values (orange) due to CE. A Lognormal curve is fitted to the distributions: positive SPD (black solid curve) and negative SPD(red dashed curve). The vertical lines indicate the mean value of the fit. The four panels are for the four CE factors. *Inset*: Zoomed out version of the histogram shows that for some injected sky locations the SPD are as high as over 75 % indicating a significant impact.

Figure 9.8 together we can conclude that for some sky locations the probability of finding the source might be less than 15 % even though the searched sky area increases by as much as 60 %.

For example, at source location ($\phi = 279°, \theta = 41.81°$), the number of pixels required to reach 90 % source localization area increases from 1412 to 6750 for the CE factor of 0.9. Thus the 90 % source localization area increased by 3538.5 sq. deg. with

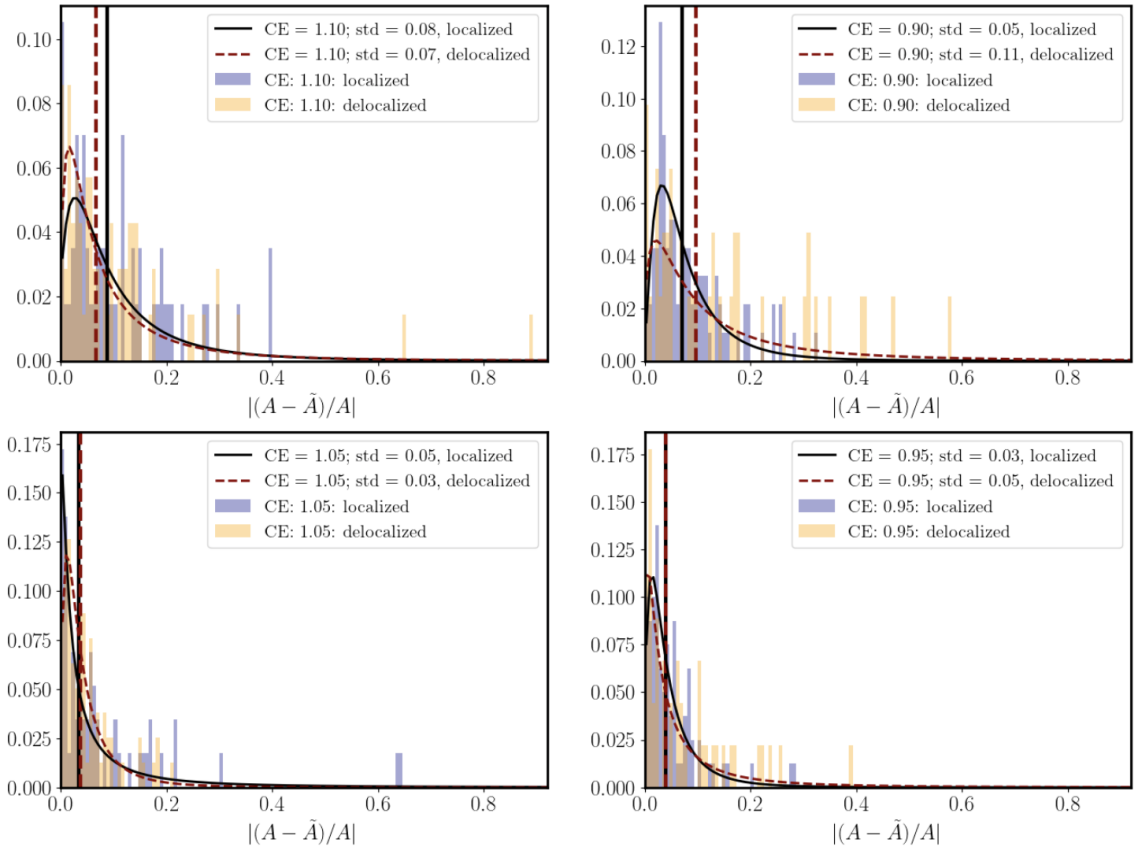

Figure 9.8. Histogram of the absolute value of the relative change in searched 90 % sky localization area due to CE only for the source locations that get more localized (blue) and delocalized (orange). A Lognormal curve is fitted to the distributions: injections reconstructed with improved localization (black solid curve) and those reconstructed with worse localization(red dashed curve). The vertical lines indicate the mean value of the fit. The four panels are for the four CE factors. For some injected sky locations, the relative change is as high as over 60 %, indicating a significant impact.

$|(A - \tilde{A})/A| = 3.7$. However, the SPD at 90 % probability in this case is $\sim$ 85 %. This indicates only an additional 10 % chance of finding the source after searching an extra 3538.5 sq. deg. of the sky area for a given -10 % CE in the LIGO Hanford data.

At the sky location ($\phi = 270.0°, \theta = 0.0°$), the number of pixels required to reach 90 % source localization area increases from 18 pixels without CE to 351 pixels with $CE = 0.95$, resulting in $|A - \tilde{A}|/A = 18.5$. This implies that the 90 % source localization area increases by 219.5 sq. deg. in this case. The SPD at 90 % probability is again $\sim$ 80 %,

indicating only an additional 10 % chance of finding the source after searching an extra 219.5 sq. deg. of the sky area. We removed both of these data points from the figure as they were an outliers with high SPD.

Figure 9.9 shows how the the median of the absolute value of the relative change for the 90 % source localization area varies as a function of the binned network SNR. In this plot, the outliers have not been removed and hence we calculate the median value. The error bars are the standard deviation on the median. From Figure 9.9, there seems to be no strong correlation between the error $|A - \tilde{A}/A|$ and the network SNR. Figure 9.10 shows a similar plot of the median of the absolute value of the SPD as a function of the binned SNR.

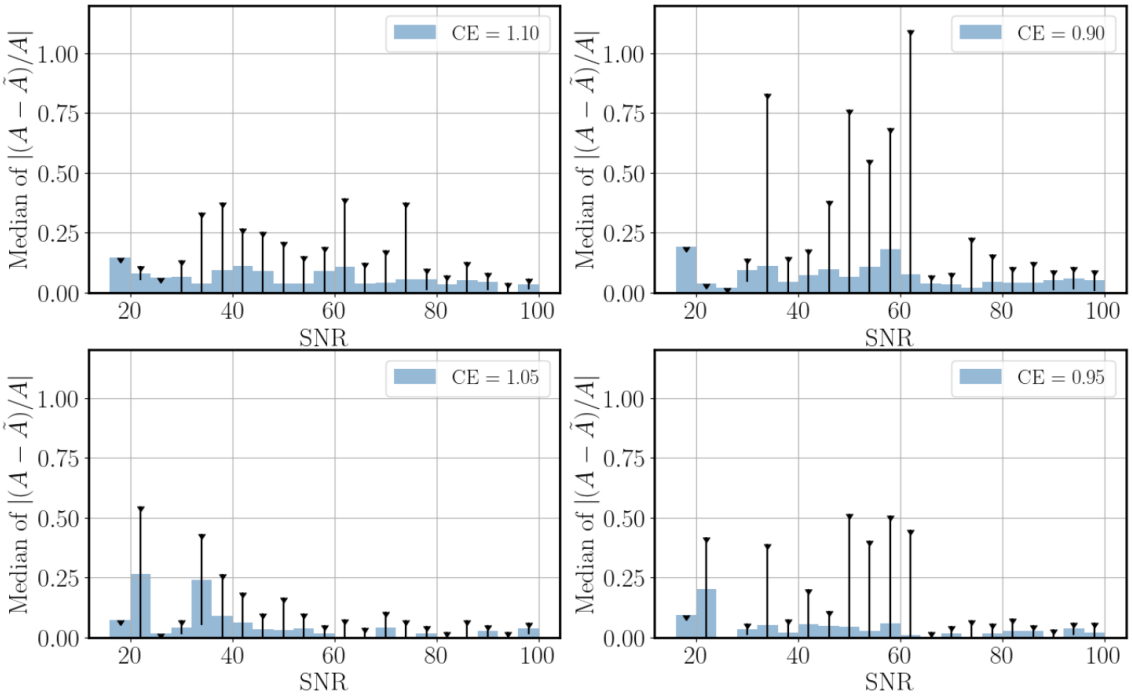

Figure 9.9. Median of the absolute value of the relative change in 90 % sky area versus binned network SNR as reported by cWB. The error bars are the positive part of the standard deviation on the median. The four panels are for the four CEs each.

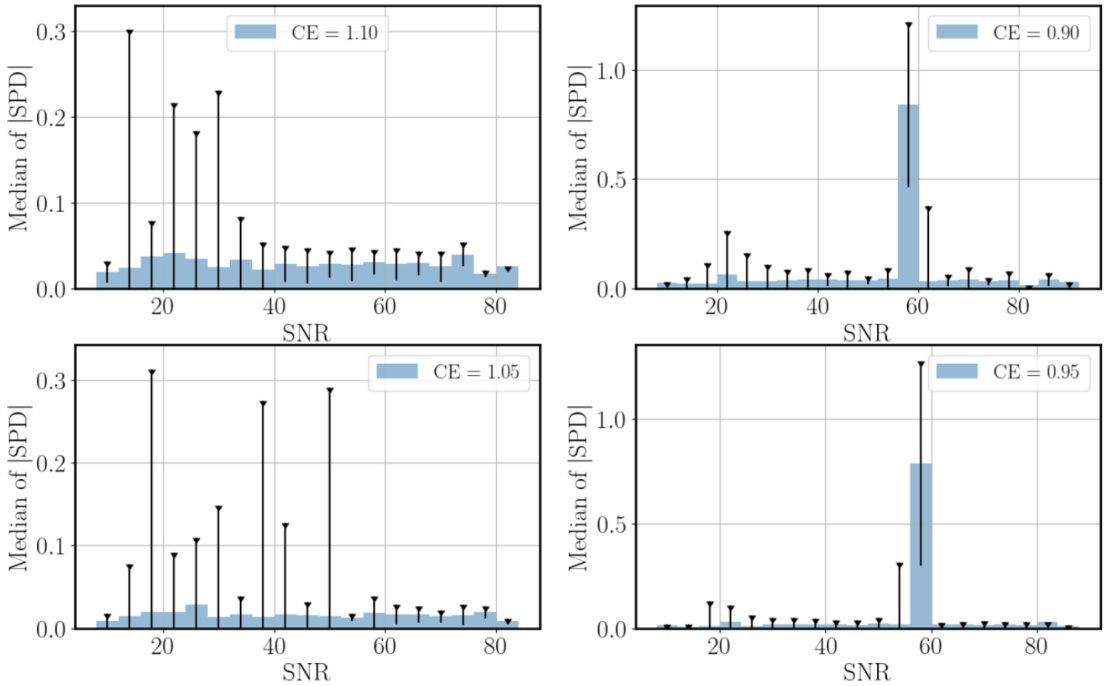

Figure 9.10. Median of the absolute value of the SPD at 90 % cumulative probability versus binned network SNR as reported by cWB. The error bars are the standard deviation on the median. The four panels are for the four CEs each.

This study was repeated for a few other cases with different polarization angle, GPS time, distance and waveform. For the comparison study we will only look at the histograms of the SPD and the relative change in the 90 % source localization area to check if the results are compatible or not.

9.4.1. At a Different Distance. To study the effect of distance, we injected the same Mueller 2012 waveform with $\psi = 30°$ at a distance of 2 kpc at three hundred different sky locations shown in Figure 9.5, all at the same GPS time 1240812613. In the figure, the sky locations marked in red are those injections that cWB could not detect. This includes the sky locations that were missed when the waveforms were injected at 1 kpc.

The plots for SPD and the relative change in the area are shown in Figures 9.11 - 9.14. These plots compare the new set of injection to the previous ones injected at GPS time 1240812613 with $\psi = 30°$ and at a distance of 1 kpc.

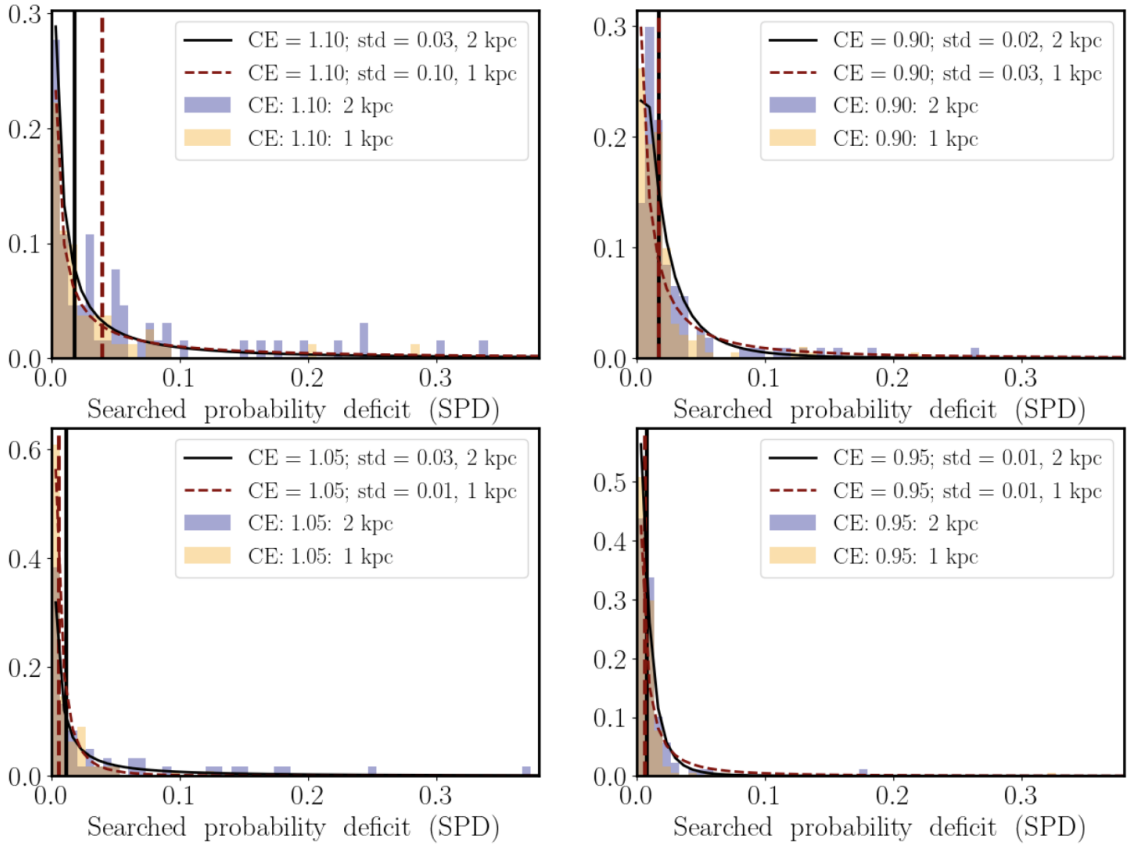

Figure 9.11. Comparison of histograms of the SPD up to 90 % cumulative probability in presence CE for the detected injections with positive SPD between those injected at 1 kpc (orange) and 2 kpc (blue). A Lognormal curve is fitted to the distributions: injections at GPS = 1240812613 (black solid curve) and those at GPS = 1240812455 (red dashed curve). The vertical lines indicate the mean value of the fit. The four panels are for the four CE factors.

9.4.2. At a Different GPS Time. The Virgo data had a glitch about 2 seconds after the GPS time at which we were injecting the Mueller waveform at three hundred different sky location into the LIGO-Virgo data stream. So another set of Mueller 2012 waveform injections were made at the same sky locations shown in Figure 9.5 at 1 kpc and with $\psi = 30°$. But the injection time was chosen to be GPS time 1240812455 ensuring that there was no glitch in any of the detector data stream till 30 seconds before and after the injection time. Figures 9.15 - 9.18 compares the plots for SPD, the relative change in the

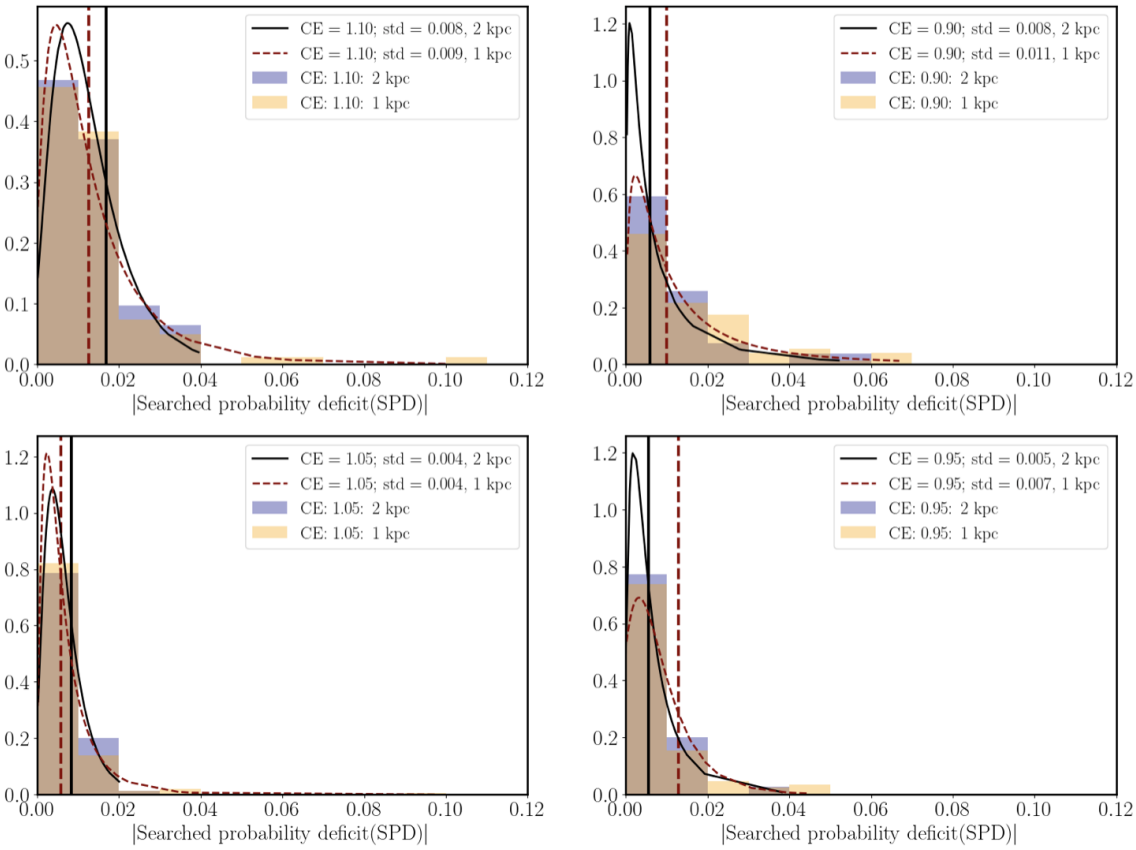

Figure 9.12. Comparison of histograms of the absolute value of the SPD up to 90 % cumulative probability in presence CE for the detected injections with negative SPD between those injected at 1 kpc (orange) and 2 kpc (blue). A Lognormal curve is fitted to the distributions: injections at GPS = 1240812613 (black solid curve) and those at GPS = 1240812455 (red dashed curve). The vertical lines indicate the mean value of the fit. The four panels are for the four CE factors.

area for the new set of injections with the previous one injected at GPS time 1240812613 at a distance of 1 kpc. The results seem similar to each each other. However, the SNR of the reconstructed events injected at GPS time 1240812613 were almost twice the ones injected at GPS time 1240812455.

9.4.3. With a Different Polarization Angle. Another set of the same Mueller 2012 waveform was injected at the same sky locations shown in Figure 9.5 at a distance of 1 kpc and GPS time 1240812455. However, the polarization angle was specified to be $\psi = 60°$.

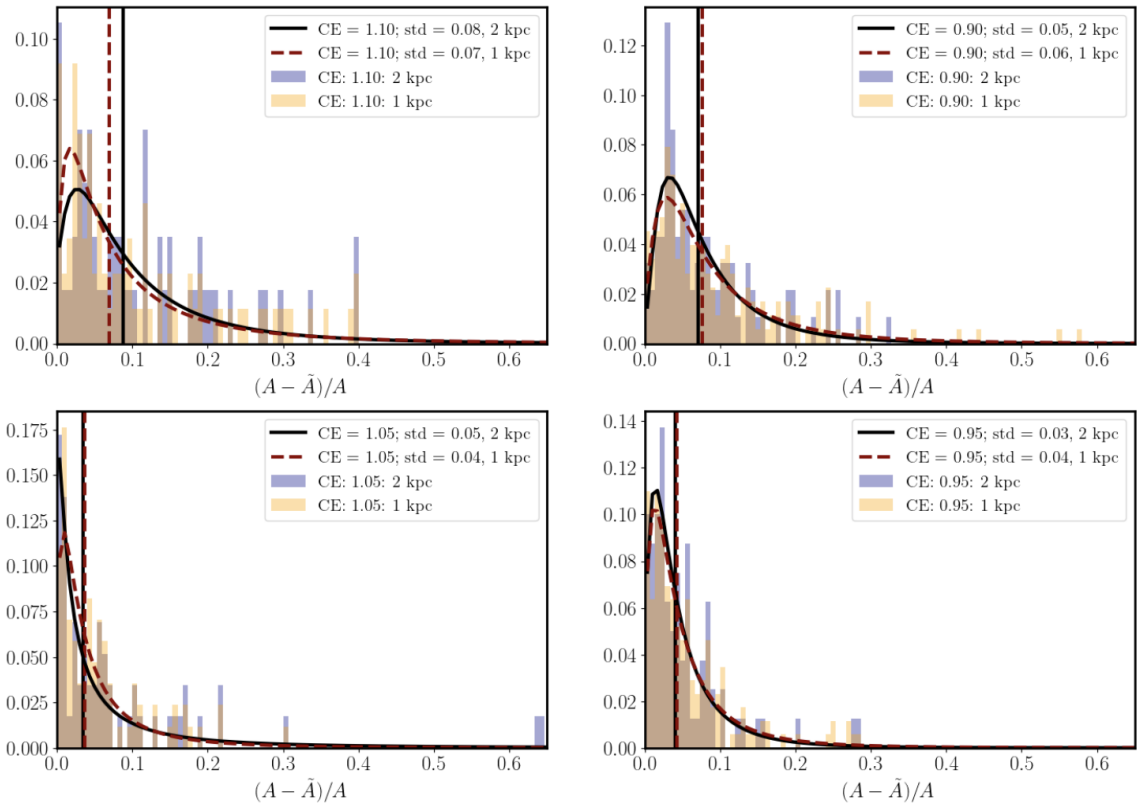

Figure 9.13. Comparison of histograms of relative change in 90 % sky area due to CE only for the detected sky locations that get localized between two sets of injections at 1 kpc (orange) and 2 kpc (blue). A Lognormal curve is fitted to the distributions: injections at 2 kpc (black solid curve) and those at 1 kpc (orange) (red dashed curve). The vertical lines indicate the mean value of the fit. The four panels are for the four CE factors.

Figures 9.19 - 9.22 compares the plots for SPD, the relative change in the area for the new set of injections with $\psi = 60°$ to the previous case.

9.4.4. With Different Waveforms. We also compared the impact of CEs for different CCSN waveforms. We injected Kuroda 2017 waveform at the three hundred sky locations in Figure 9.5 at 1 kpc with $\psi = 30°$ and at $GPS = 1240812455$.

Figures 9.23 - 9.26 compares the plots for SPD, the relative change in the area for the new set of injections to the ones with Mueller 2012 waveforms keeping all other parameters the same.

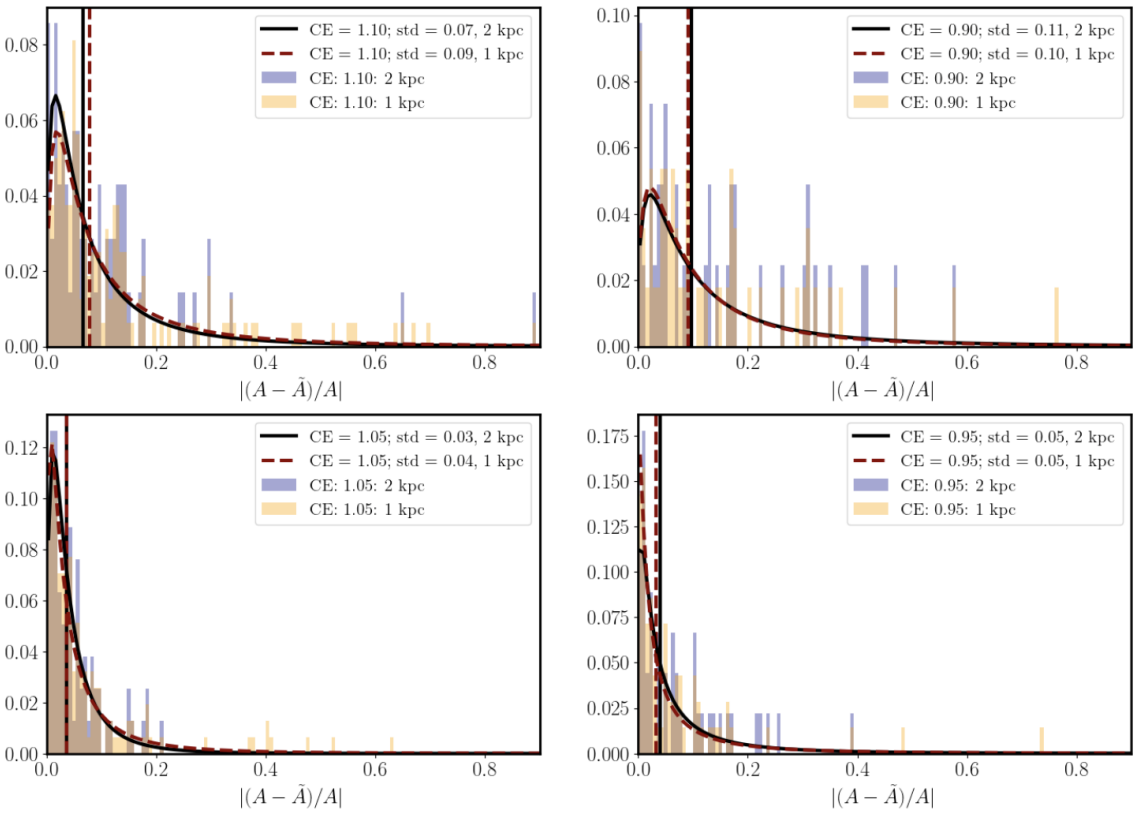

Figure 9.14. Comparison of histograms of the absolute value of the relative change in 90 % sky area due to CE only for the detected sky locations that get more delocalized between two sets of injections at at 1 kpc (orange) and 2 kpc (blue). A Lognormal curve is fitted to the distributions: injections at 2 kpc (black solid curve) and those at 1 kpc (orange) (red dashed curve). The vertical lines indicate the mean value of the fit. The four panels are for the four CE factors.

9.5. SUMMARY

This section describes a study to quantify the impact of overall calibration error on sky localization of CCSN sources for the LIGO-Virgo network. We used a LIGO detection pipeline, cWB to the study the sky localization of simulated SN sources using Mueller 2012 model. We defined two parameters the relative change in the 90 % sky localization area

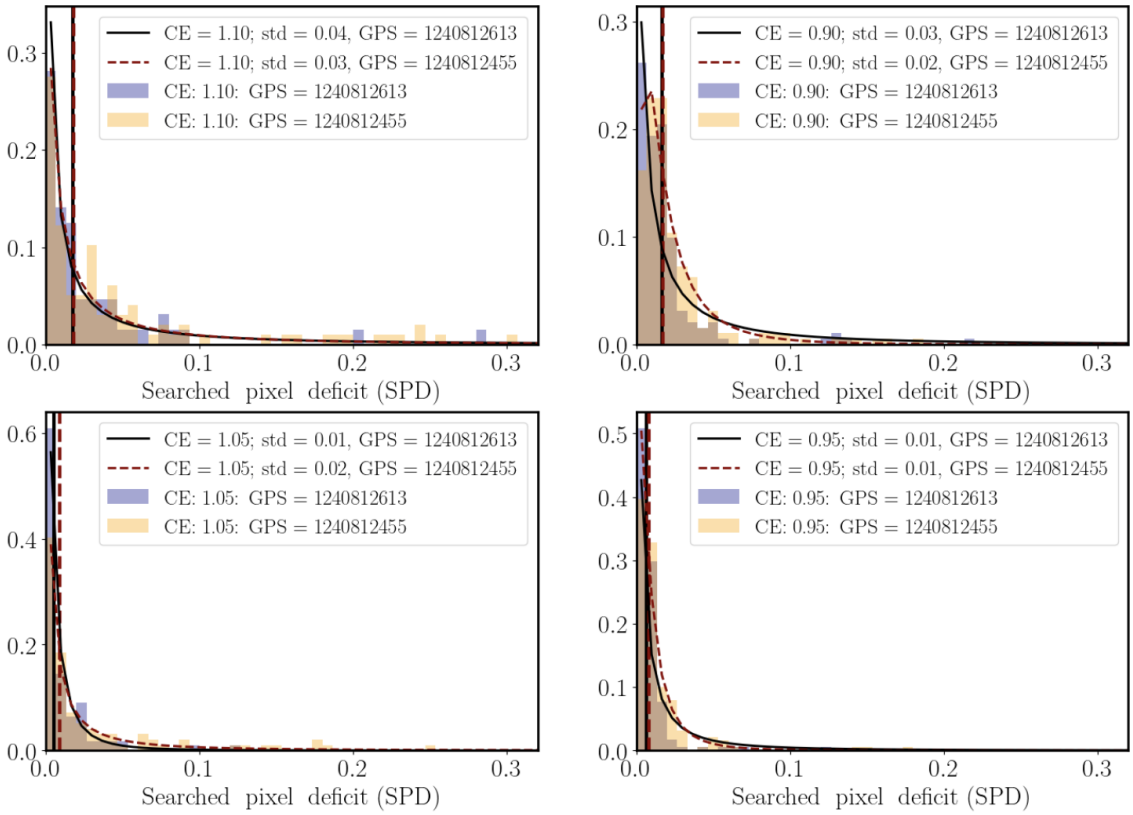

Figure 9.15. Comparison of histograms of the absolute value of the SPD up to 90 % cumulative probability in presence CE for the detected injections with only the positive SPD between those injected at GPS = 1240812613 (blue) and GPS = 1240812455 (orange). A Lognormal curve is fitted to the distributions: injections at GPS = 1240812613 (black solid curve) and those at GPS = 1240812455 (red dashed curve). The vertical lines indicate the mean value of the fit. The four panels are for the four CE factors.

and a SPD at 90 % cumulative probability to quantify the impact of CE. A positive relative change in the 90 % sky localization area indicates that the source localization improved due to the overall CE, whereas a negative value indicated that the source localization worsened.

We injected a Mueller 2012 with same source orientation at three hundred different sky locations and at a particular distance, with a specified polarization angle and at the same GPS time. We introduced overall CE of ±10 % and ±5 % into the Hanford data by multiplying the noise floor of the interferometer as well as the signal by factors of 1.1, 0.9, 1.05, 0.95 respectively. Since the detection efficiency of the cWB algorithm

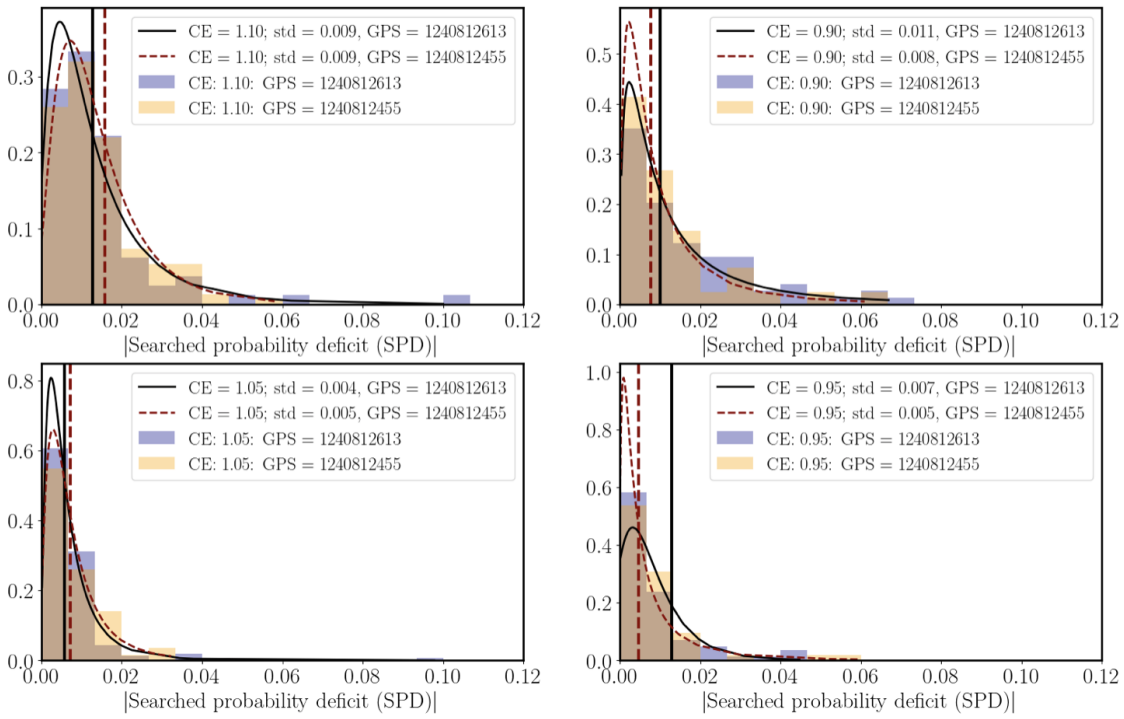

Figure 9.16. Comparison of histograms of the absolute value of the SPD up to 90 % cumulative probability in presence CE for the detected injections with negative SPD between those injected at $GPS = 1240812613$ (blue) and $GPS = 1240812455$ (orange). A Lognormal curve is fitted to the distributions: injections at GPS = 1240812613 (black solid curve) and those at GPS = 1240812455 (red dashed curve). The vertical lines indicate the mean value of the fit. The four panels are for the four CE factors.

is $\sim$ 90 % at a distance of 1 kpc, we recovered 268 of the total injected events. We then calculated the SPD and the relative change in the 90 % sky localization area for the injections that were recovered by cWB. We studied different cases, comparing the impact of CE for different polarization angles, at different GPS times, at different distances and also compared between two different waveforms, Mueller 2012 and Kuroda 2017.

Preliminary results indicate that the average relative changes in the 90 % sky localization confidence regions are from $\sim$ 10 % to as large as 18 % in presence of the CEs. Associated average errors in estimated probabilities for these regions are from $\sim$ 1 % to as large as 5 % due to overall CEs. Furthermore, for a few sky locations, SPD are as large

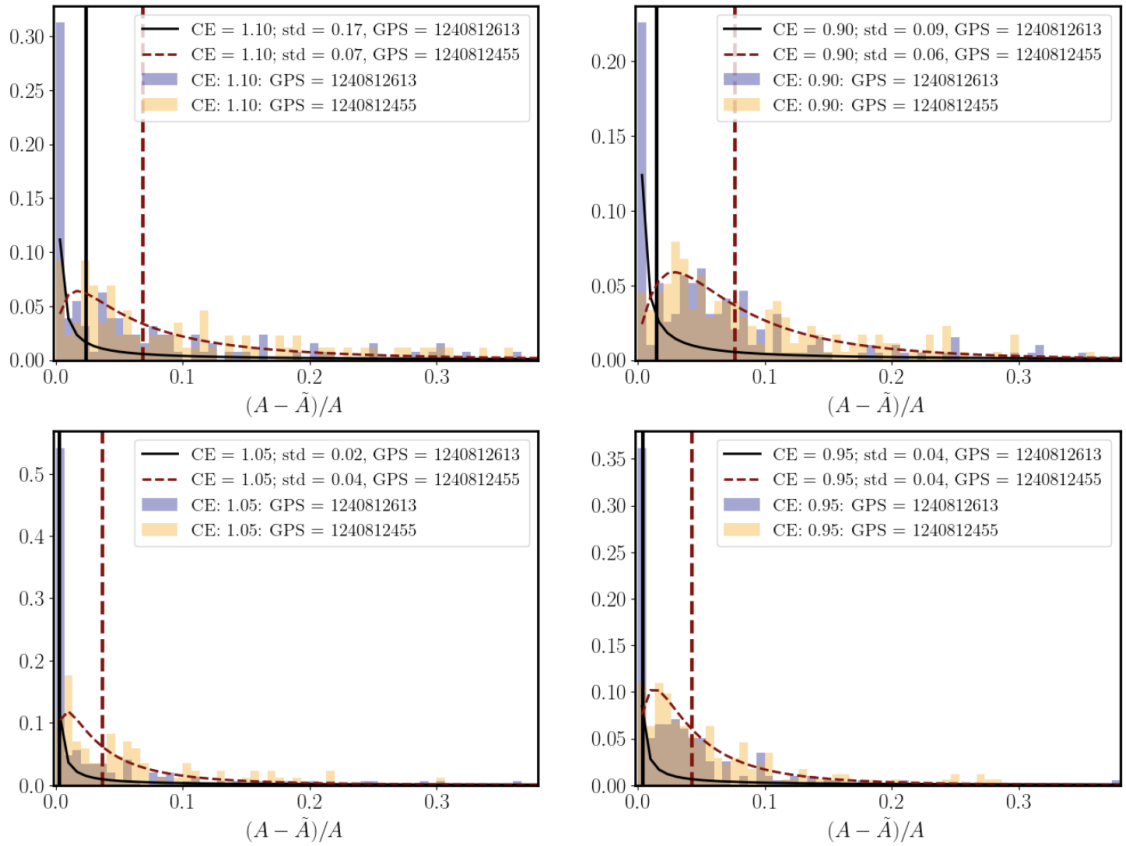

Figure 9.17. Comparison of histograms of relative change in 90 % sky area due to CE only for the detected sky locations that seems to get localized between two sets of injections at GPS = 1240812613 (blue) and GPS = 1240812455 (orange). A Lognormal curve is fitted to the distributions: injections at GPS = 1240812613 (black solid curve) and those at GPS = 1240812455 (red dashed curve). The vertical lines indicate the mean value of the fit. The four panels are for the four CE factors.

as $\sim$ 85 % for a CE factor of 1.1. This implies that in case LVK network detects GW from a CCSN event in future, there are a few sky locations where there is a low to almost negligible chance of finding counterparts to GW signals within the 90 % confidence regions in follow-up observations by EM observatories if the Hanford data has a CE of $\pm$10 %. A more in-depth study is required to understand why these particular regions in the sky are more affected due to an overall CEs in a single detector.

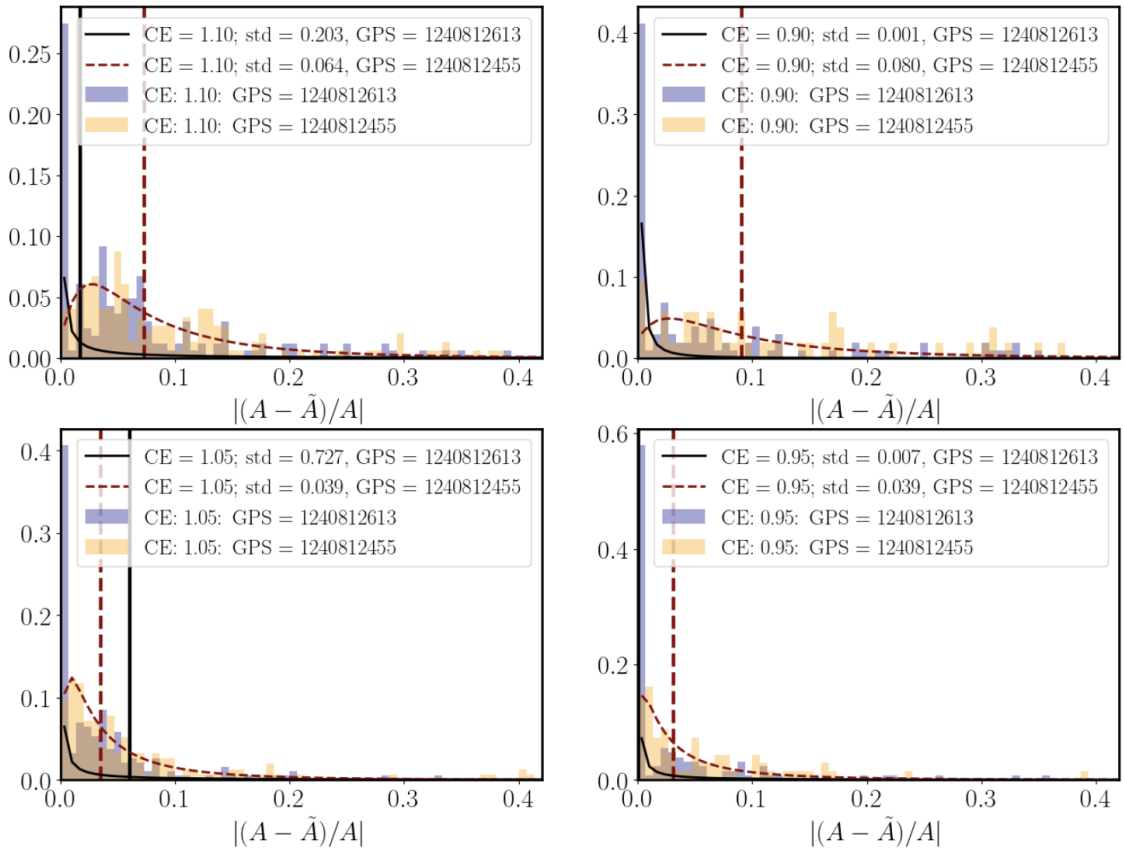

Figure 9.18. Comparison of histograms of the absolute value of the relative change in 90 % sky area due to CE only for the detected sky locations that get more delocalized between two sets of injections at GPS = 1240812613 (blue) and GPS = 1240812455 (orange). A Lognormal curve is fitted to the distributions: injections at GPS = 1240812613 (black solid curve) and those at GPS = 1240812455 (red dashed curve). The vertical lines indicate the mean value of the fit. The four panels are for the four CE factors.

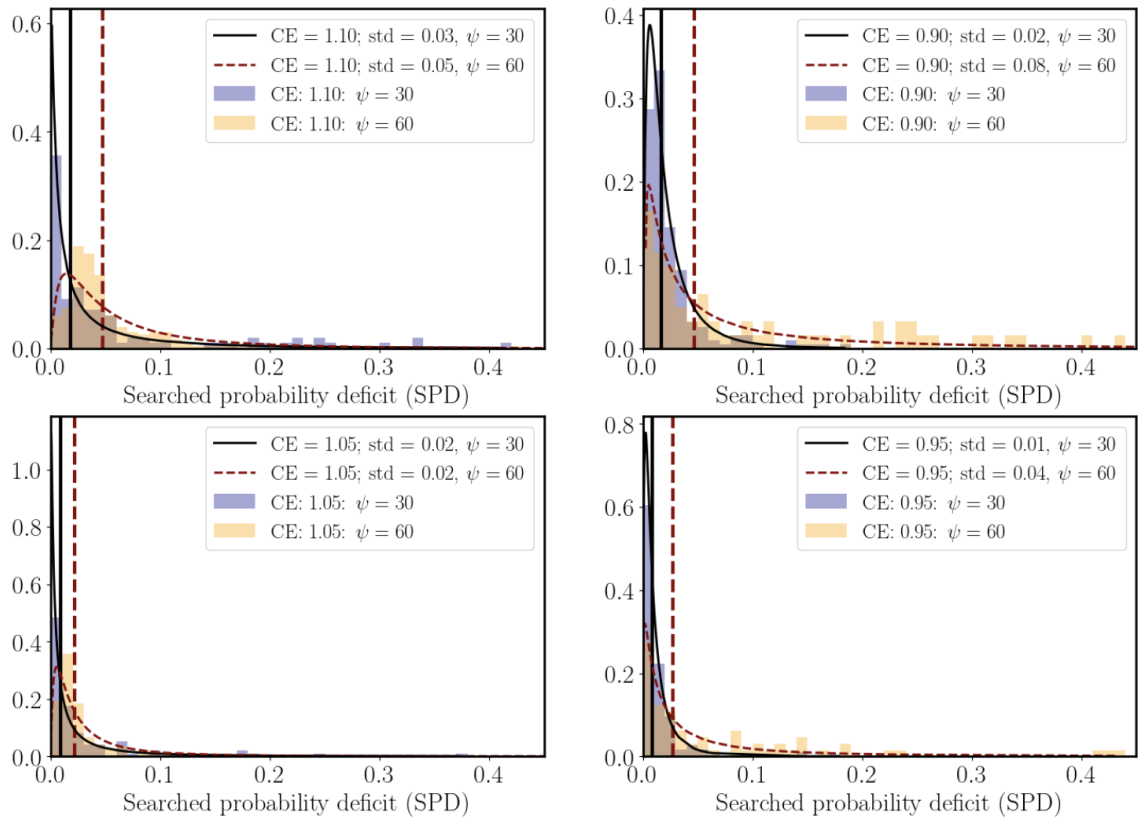

Figure 9.19. Comparison of histograms of the SPD up to 90 % cumulative probability in presence CE for the detected injections with positive SPD between those injected with $\psi = 30°$ (blue) and $\psi = 60°$ (orange). A Lognormal curve is fitted to the distributions: injections with $\psi = 30°$ (black solid curve) and those with $\psi = 60°$ (red dashed curve). The vertical lines indicate the mean value of the fit. The four panels are for the four CE factors.

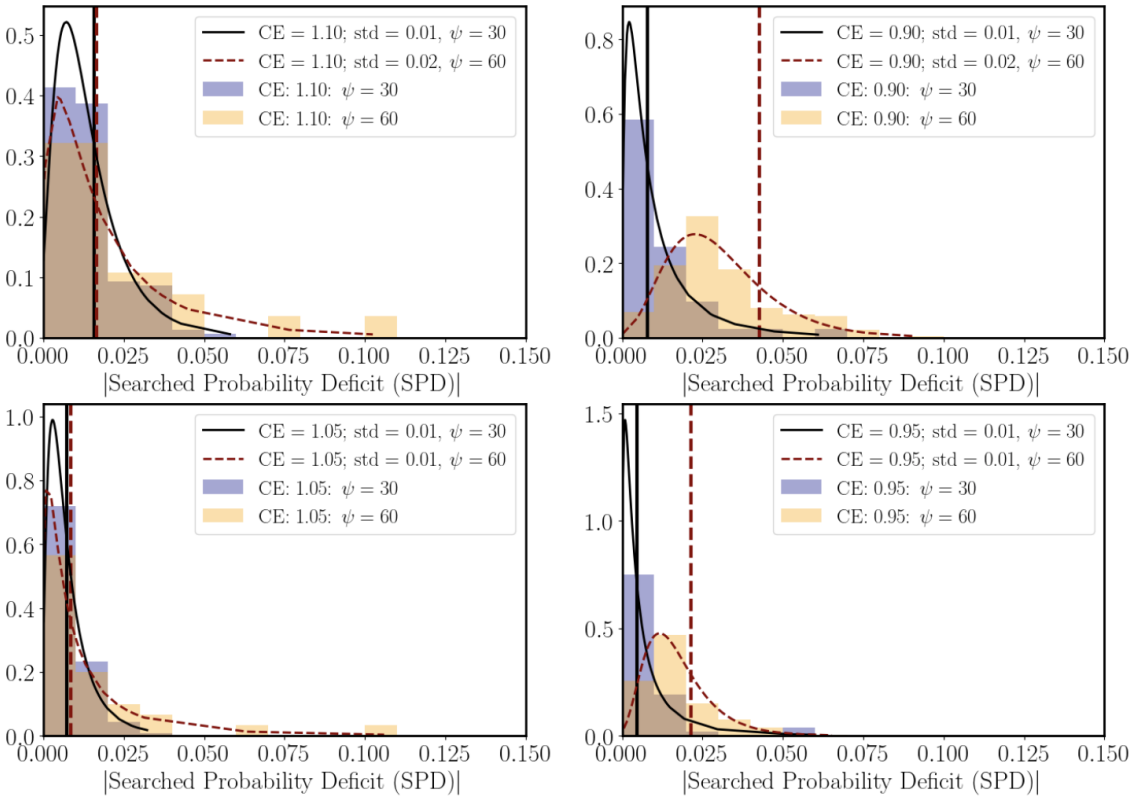

Figure 9.20. Comparison of histograms of the absolute value of the SPD up to 90 % cumulative probability in presence CE for the detected injections with negative SPD between those injected at $\psi = 30°$ (blue) and $\psi = 60°$ (orange). A Lognormal curve is fitted to the distributions: injections with $\psi = 30°$ (black solid curve) and those with $\psi = 60°$ (red dashed curve). The vertical lines indicate the mean value of the fit. The four panels are for the four CE factors.

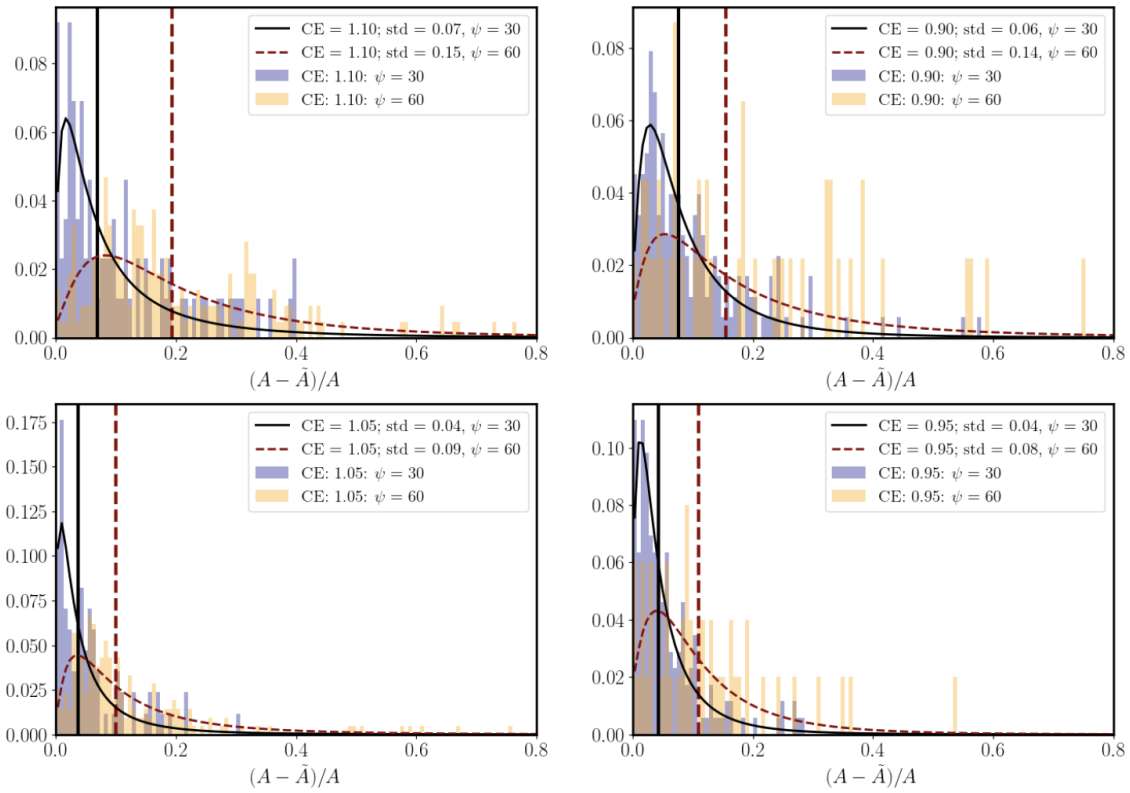

Figure 9.21. Comparison of histograms of relative change in 90 % sky area due to CE only for the detected sky locations that get localized between two sets of injections at $\psi = 30°$ (blue) and $\psi = 60°$ (orange). A Lognormal curve is fitted to the distributions: injections at $\psi = 30°$ (black solid curve) and those at $\psi = 60°$ (orange) (red dashed curve). The vertical lines indicate the mean value of the fit. The four panels are for the four CE factors.

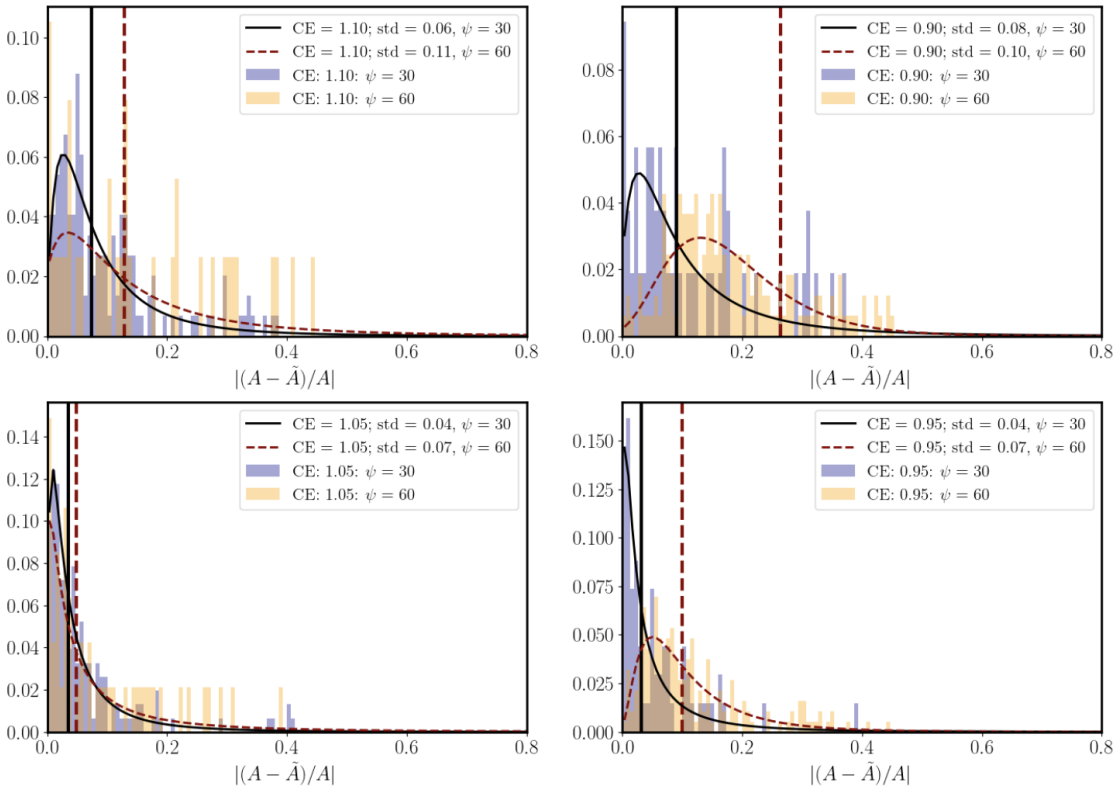

Figure 9.22. Comparison of histograms of the absolute value of the relative change in 90 % sky area due to CE only for the detected sky locations that get more delocalized between two sets of injections at $\psi = 30°$ (blue) and $\psi = 60°$ (orange). A Lognormal curve is fitted to the distributions: injections at $\psi = 30°$ (black solid curve) and those at $\psi = 60°$ (orange) (red dashed curve). The vertical lines indicate the mean value of the fit. The four panels are for the four CE factors.

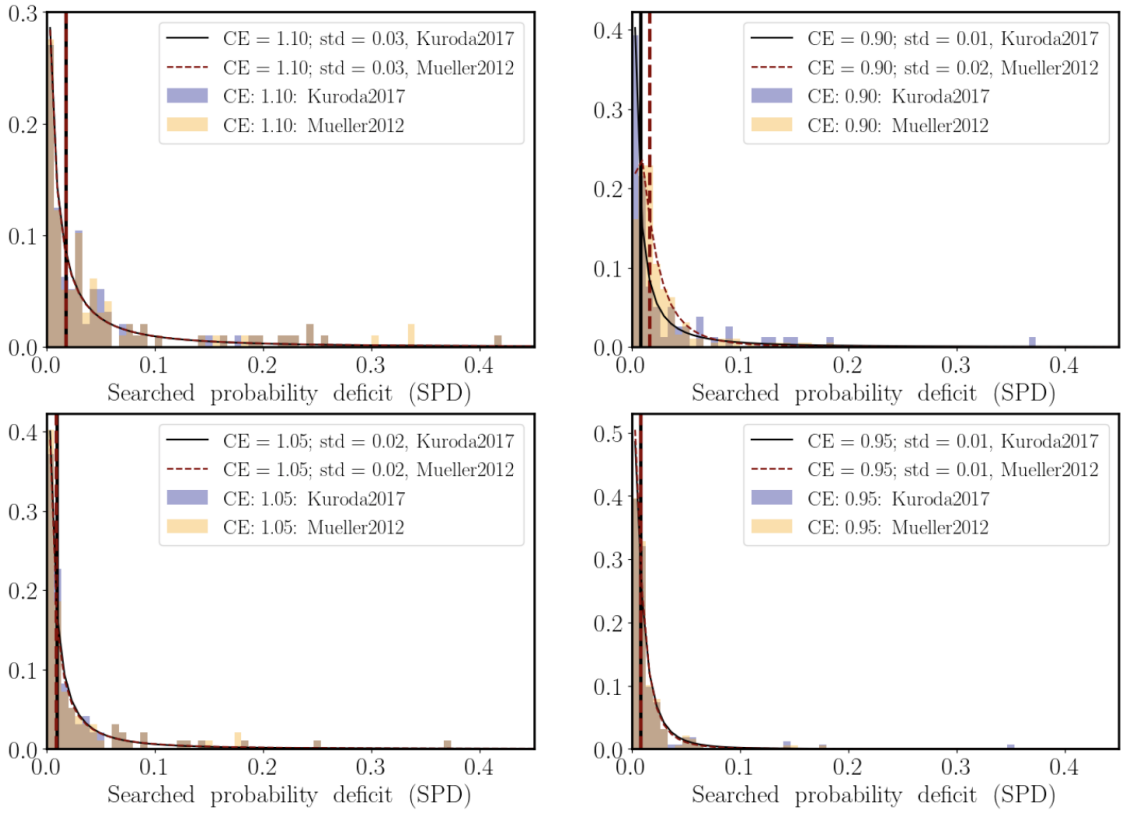

Figure 9.23. Comparison of histograms of the SPD up to 90 % cumulative probability in presence CE for the detected injections with positive SPD between the two sets of injections with different waveforms, Mueller 2012 (orange) and Kuroda 2017 (blue). A Lognormal curve is fitted to the distributions: injections with Kuroda 2017 waveform (black solid curve) and with Mueller 2012 waveform (red dashed curve). The vertical lines indicate the mean value of the fit. The four panels are for the four CE factors.

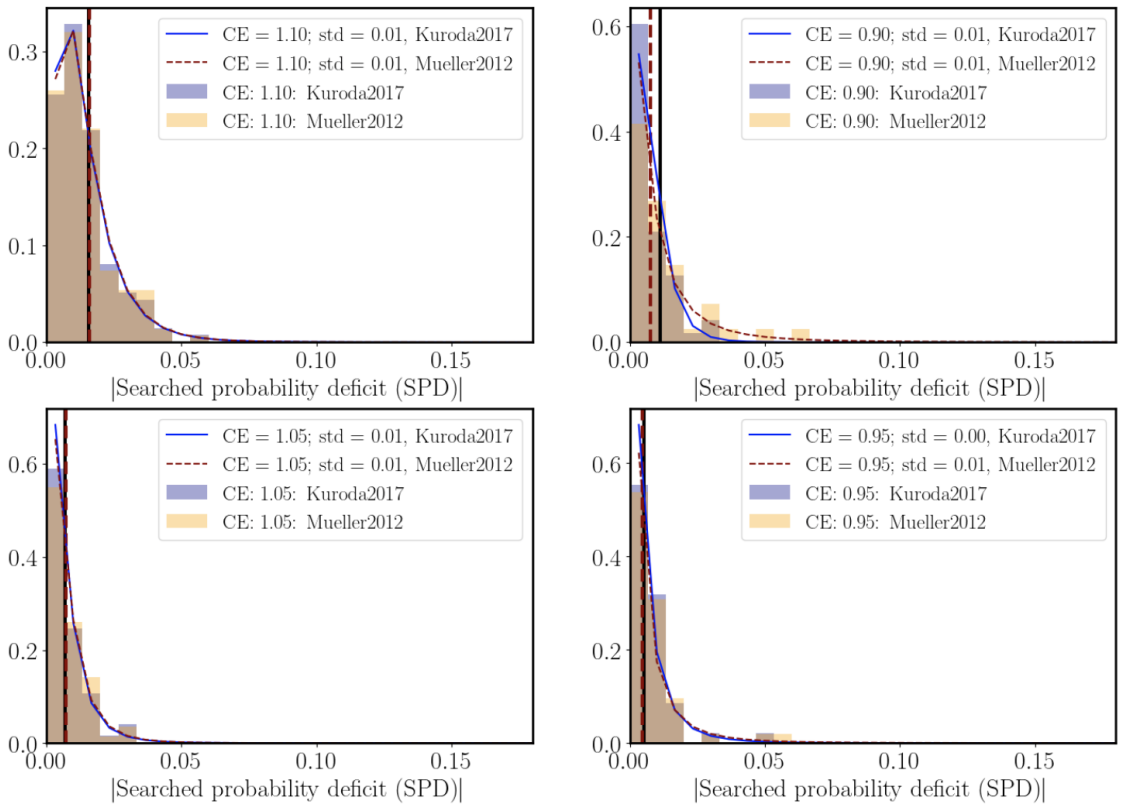

Figure 9.24. Comparison of histograms of the absolute value of the SPD up to 90 % cumulative probability in presence CE for the detected injections with negative SPD between the two sets of injections with different waveforms, Mueller 2012 (orange) and Kuroda 2017 (blue). A Lognormal curve is fitted to the distributions: injections with Kuroda 2017 waveform (black solid curve) and with Mueller 2012 waveform (red dashed curve). The vertical lines indicate the mean value of the fit. The four panels are for the four CE factors.

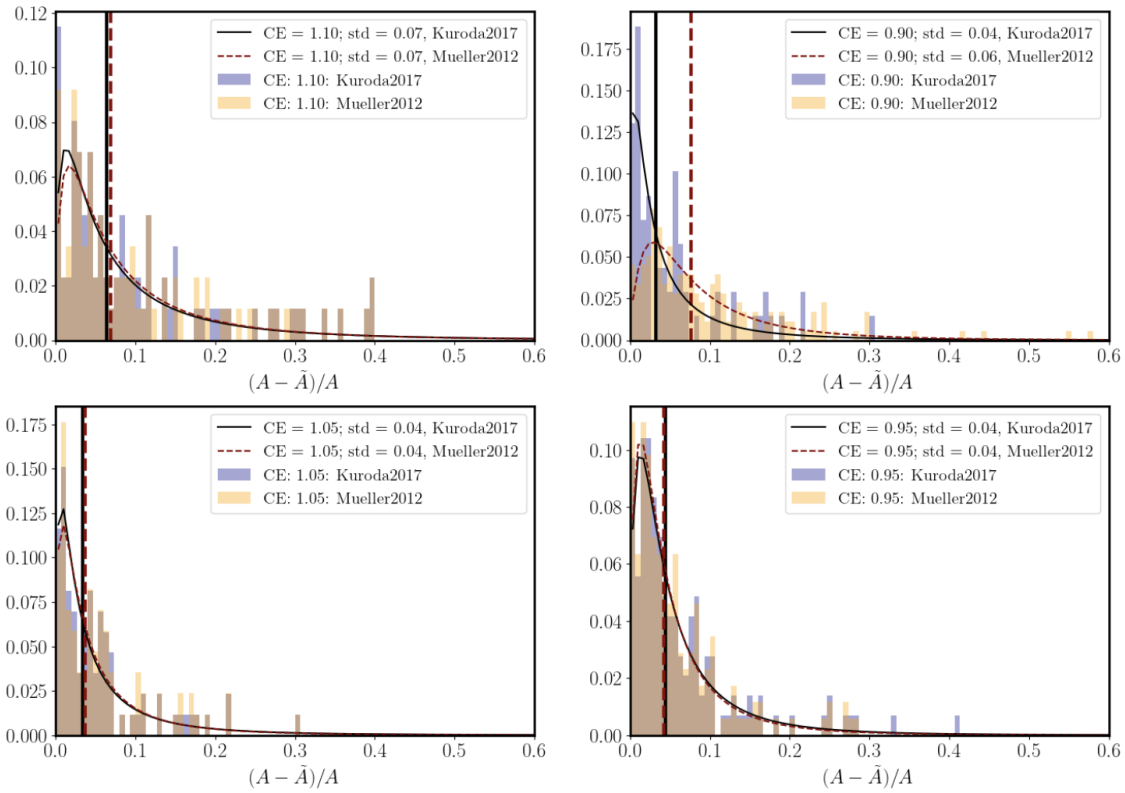

Figure 9.25. Comparison of histograms of relative change in 90 % sky area due to CE only for the detected sky locations that get localized between two sets of injections with different waveforms, Kuroda 2017 (blue) and Mueller 2012 (orange). A Lognormal curve is fitted to the distributions: injections using Kuroda 2017 waveform (black solid curve) and those using Mueller 2012 (red dashed curve). The vertical lines indicate the mean value of the fit. The four panels are for the four CE factors.

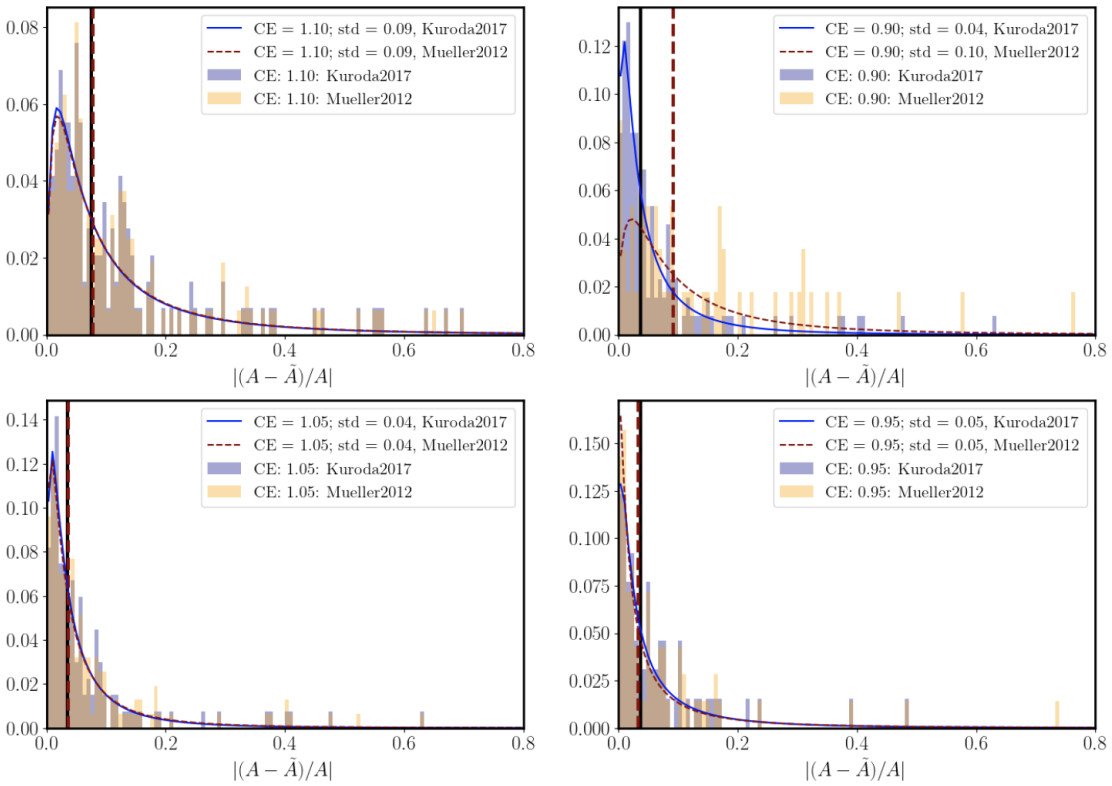

Figure 9.26. Comparison of histograms of the absolute value of the relative change in 90 % sky area due to CE only for the detected sky locations that get more delocalized between two sets of injections with different waveforms, Kuroda 2017 (blue) and Mueller 2012 (orange). A Lognormal curve is fitted to the distributions: injections using Kuroda 2017 waveform (black solid curve) and those using Mueller 2012 (red dashed curve). The vertical lines indicate the mean value of the fit. The four panels are for the four CE factors.

10. CONCLUSIONS

This dissertation describes how the state of the art in generating displacement fiducials using Pcals for ground-based interfermoteric GW detectors was pushed below the 0.5% accuracy level for the O3 run during which 79 GW detections were made by the LVK network (Abbott *et al.* (2021a)). Pcals, relying on power-modulated auxiliary laser beams reflecting from suspended interferometer optics, enable continuous calibration of the detectors by generating displacement fiducials proportional to the modulated laser power. Developments in the propagation of laser power calibration via transfer standards to on-line power sensors monitoring the modulated laser power have enabled generation of length fiducials with sub-0.5 % accuracy for the LIGO detectors (D Bhattacharjee *et al.* (2021)) . These estimated uncertainties are almost a factor of two smaller than the values reported for the previous observing run (Karki *et al.* (2016)). This reduction was due to efforts by NIST to realize improved laser power sensor calibration accuracy and improvements in methodology that have decreased uncertainties.

The two major improvements in the methodology for estimating the Pcal uncertainties involved taking into account the effects of temperature dependence of the responsivity of the Pcal power sensors and combining the calibrations of the Pcal systems installed at the end station of each interferometer arm to reduce uncertainties due to factors that are not common to both Pcal systems. Both methods were implemented during the O3 run for the first time. To calculate the end station power sensor calibration factors, measurements were made in three different laboratories, each maintained at a different temperature. These temperature differences were taken into account using a new formalism that was developed and implemented to include temperature corrections.

Pcal-induced periodic displacements are used to measure the frequency dependent interferometer response from swept sine transfer functions of the DARM control loop on a weekly basis (Sun *et al.* (2020)). They are also used to continually monitor time-varying

interferometer parameters (Tuyenbayev *et al.* (2017)). Thus, generating continuous, on-line displacement fiducials with sub-percent accuracy is a key element of interferometer calibration. Reducing the overall uncertainty and improving the accuracy of these Pcal dispalcements enable more accurate and precise interferometer calibration.

Realizing the important role laser power sensor calibration plays in the scientific impact of GW detections, there is increased effort within the national metrology institute community to improve power sensor calibration accuracy and precision. Scientists at NIST are developing a new generation of primary calibration standards that use bolometers and carbon nanotube absorbers and are expected to significantly lower uncertainties compared with the primary standards currently being used (Vaskuri *et al.* (2020)). These sensors may someday prove suitable for installation inside the vacuum envelope where several sources of uncertainty would be mitigated, providing laser power calibration directly traceable to SI units in-situ (Lehman (2020)). These developments at NIST are expected to reduce the Pcal power sensor calibration uncertainty provided by NIST from 0.32% to $\sim$ 0.1%.

Unknown or unaccounted for systematic errors in calibration of the Pcal systems would affect the overall calibration of the detectors and lead to inaccurate strain data. If that is the case, the source parameter estimates that are extracted from the GW signals, such as distance, masses and spins would be inaccurate. Systematic errors in the relative calibration of detectors in the GW network would affect the sky localization of GW sources, limiting opportunities for multi-messenger astronomy. This dissertation includes a study of the impact of overall calibration errors on sky localization of burst-like GW sources. To quantify the impact of overall CEs on sky localization for sources located all across the sky, a simulated supernova waveform (Mueller 2012) was injected with fixed polarization angle and distance at various sky locations. Artificial CEs of ± 10 % and ± 5 % were applied to data from one of the LIGO detectors, LIGO Hanford. We defined two parameters, the relative change in the 90 % sky localization area and the searched probability deficit at 90 % cumulative probability, to quantify the impact of the overall CEs on sky localization. We

found that on an average the searched probability deficit was at most 5 % indicating that the 2 % calibration accuracy level achieved during the O3 run was sufficient for accurate source localization. However, there were some source locations at which the 90 % source localization area reduced by over 60 % but the SPD was above 85 %. These large values indicate that even for cases where the localization area decreased, the cWB algorithm might reconstruct the source location displaced from the injected location. There were also cases where highly localized sources in the absence of a CE became highly delocalized in the presence of a CE. This also resulted in a high SPD.

The study was repeated for a different polarization angle, different distance, and different injection time (different interferometer noise floor), as well as a different modeled supernova waveform (Kuroda 2017). Sky localization area and searched probability deficit results were similar to the initial case, described above.

In these analyses, CEs were introduced into the data for a single detector. Similar studies could be carried out with CEs (positve or negative) introduced into more than one detector in the network. This work can also be extended to study how systematic calibration errors affect the sky localization of GW signals from CCSN events when detectors in the LVK network are operating at their design sensitivities. It could also be extended for different network configurations, for example subsets of the LVK network, the LVKI network that includes the LIGO India detector and for future third-generation detector networks.

Developing the methods employed in this research could result in the ability to quantify acceptable overall calibration errors in terms of tolerable searched probability deficits.As more detectors join the network of GW observatories, accurate source localization could be achieved using the timing information alone. These methods could also be used to study the impact of timing errors, i.e., errors in the apparent arrival times of GW signals at the detectors.

Accurate source localization is crucial for prompt follow-up searches for electromagnetic and neutrino counterparts, enabling multi-messenger astronomy. Observing an event with multiple cosmic messengers provides information about properties of the source, its emission processes, its environment, etc. Since accurate source localization relies on accurately calibrated strain data, pushing the overall calibration uncertainty to the sub-percent level will be required. In 2009, Lindblom estimated that calibration accuracy of 0.5 % or better would be required to optimally extract information from GW signals (Lindblom (2009)). This implies that calibration of Pcal displacement fiducials with uncertainties well below 0.5 % will also be required. With the improvements in the calibration of Pcal power transfer standards expected for O4, the Pcal calibration uncertainties are expected to be even lower than they were for O3. This should ensure that multi-messenger astronomy opportunities enabled by accurate sky localization of CCSN events detected by the cWB pipeline will not be limited by overall Pcal fiducial displacement uncertainties.

REFERENCES

Aasi, J. *et al.*, 'Directed search for continuous gravitational waves from the galactic center,' Phys. Rev. D, 2013, **88**.

Aasi, J. *et al.*, 'Advanced LIGO,' , 2015a, **32**, p. 074001, doi:https://doi.org/10.1088/0264-9381/32/7/074001.

Aasi, J. *et al.*, 'Searches for continuous gravitational waves from nine young supernova remnants,' Astroph. J., 2015b, **813**.

Abbott *et al.*, 'Gwtc-3: Compact binary coalescences observed by ligo and virgo during the second part of the third observing run,' In preparation, 2021a.

Abbott, B., Abbott, R., Adhikari, R., *et al.*, 'Beating the spin-down limit on gravitational wave emission from the crab pulsar,' Astroph. J, 2008, p. 683:L45.

Abbott, B. *et al.*, 'GW150914: First results from the search for binary black hole coalescence with Advanced LIGO,' Phys. Rev. D, 2016a, **93**(12), p. 122003, doi: https://doi.org/10.1103/PhysRevD.93.122003.

Abbott, B. *et al.*, 'GW150914: The Advanced LIGO Detectors in the Era of First Discoveries,' Phys. Rev. Lett., 2016b, **116**, p. 131103, doi: https://doi.org/10.1103/PhysRevLett.116.131103.

Abbott, B. P., Abbott, R., Abbott, T. D., *et al.*, 'On the progenitor of binary neutron star merger gw170817,' ApJL, 2017a, **850**.

Abbott, B. P. *et al.*, 'Limits on gravitational-wave emission from selected pulsars using ligo data,' Phys. Rev. Lett., 2005, **94**.

Abbott, B. P. *et al.*, 'Ligo: the laser interferometer gravitational-wave observatory,' Rep. Prog. Phys., 2009a.

Abbott, B. P. *et al.*, 'An upper limit on the stochastic gravitational-wave background of cosmological origin,' Nature, 2009b, **460**.

Abbott, B. P. *et al.*, 'Advanced ligo,' arXiv:1411.4547, 2014.

Abbott, B. P. *et al.*, 'Advanced ligo,' Class. Quantum Grav., 2015, **37**.

Abbott, B. P. *et al.*, 'Calibration of the advanced ligo detectors for the discovery of the binary black-hole merger gw150914,' Phys. Rev. D, 2017b, **95**, p. 062003, doi: https://link.aps.org/doi/10.1103/PhysRevD.95.062003.

Abbott, B. P. *et al.*, 'Gravitational waves and gamma-rays from a binary neutron star merger: GW170817 and GRB 170817a,' Astroph. J. Lett., 2017c, **848**, p. L13, doi:https://doi.org/10.3847/2041-8213/aa920c.

Abbott, B. P. *et al.*, 'Gw170814: A three-detector observation of gravitational waves from a binary black hole coalescence,' Phys. Rev. Lett, 2017d, **119**, doi: 10.1103/PhysRevLett.119.141101c.

Abbott, B. P. *et al.*, 'Gw170817: Observation of gravitational waves from a binary neutron star inspiral,' Phys. Rev. Lett., 2017e, **119**, doi: https://doi.org/10.1103/PhysRevLett.119.161101.

Abbott, B. P. *et al.*, 'Search for continuous gravitational waves from neutron stars in globular cluster ngc 6544,' Phys. Rev. D, 2017f, **95**.

Abbott, B. P. *et al.*, 'Advanced ligo, advanced virgo and kagra observing run plans,' LIGO Report, 2019a.

Abbott, B. P. *et al.*, 'All-sky search for short gravitational-wave bursts in the second advanced ligo and advanced virgo run,' Phys. Rev. D, 2019b, **100**.

Abbott, B. P. *et al.*, 'Binary black hole population properties inferred from the first and second observing runs of advanced ligo and advanced virgo,' Astroph. J, 2019c, **882**.

Abbott, B. P. *et al.*, 'A gravitational-wave measurement of the Hubble constant following the second observing run of Advanced LIGO-Virgo,' Astroph. J submitted, 2019d.

Abbott, B. P. *et al.*, 'Search for transient gravitational wave signals associated with magnetar bursts during advanced ligo's second observing run,' Astroph. J., 2019e, **874**.

Abbott, B. P. *et al.*, 'Tests of general relativity with the binary black hole signals from the ligo-virgo catalog gwtc-1,' Phys. Rev. D, 2019f, **100**.

Abbott, B. P. *et al.*, 'A guide to ligo–virgo detector noise and extraction of transient gravitational-wave signals,' Class. Quantum Grav., 2020a, **37**.

Abbott, B. P. *et al.*, 'Gw190521: A binary black hole merger with a total mass of 150 m,' Phys. Rev. Lett., 2020b, **125**, p. 101102.

Abbott, B. P. *et al.*, 'Optically targeted search for gravitational waves emitted by core-collapse supernovae during the first and second observing runs of advanced ligo and advanced virgo,' PHYS. REV. D 101, 2020c.

Abbott, B. P. *et al.*, 'Gwtc-2: Compact binary coalescences observed by ligo and virgo during the first half of the third observing run,' Phys. Rev. X, 2021b, **11**.

Abbott, R., Abbott, T. D., Abraham, S., *et al.*, 'Observation of gravitational waves from two neutron star-black hole coalescences,' Astroph. JL, 2021c, **915:L15**.

Abbott, R. *et al.*, 'All-sky search for continuous gravitational waves from isolated neutron stars in the early o3 ligo data,' arXiv:2107.00600, 2021d.

Abbott, R. *et al.*, 'All-sky search for continuous gravitational waves in the early o3 ligo data,' Phys. Rev. D, 2021e, **103**.

Abbott, R. *et al.*, 'All-sky search for long-duration gravitational-wave bursts in the third advanced ligo and advanced virgo run,' arXiv:2107.13796, 2021f.

Abbott, R. *et al.*, 'Search for anisotropic gravitational-wave backgrounds using data from advanced ligo and advanced virgo's first three observing runs,' Phys. Rev. D, 2021g, **104**.

Abbott, R. *et al.*, 'Search for gravitational waves associated with gamma-ray bursts detected by fermi and swift during the ligo-virgo run o3a,' Astroph. J., 2021h, **915**.

Abbott, R. *et al.*, 'Searches for continuous gravitational waves from young supernova remnants in the early third observing run of advanced ligo and virgo,' arXiv:2105.11641, 2021i.

Accadia, T. *et al.*, 'Observation of gravitational waves from a binary black hole merger,' , 2016, **116**, p. 061102, doi:https://doi.org/10.1103/PhysRevLett.116.061102.

Acernese, F. *et al.*, 'Advanced virgo: a second-generation interferometric gravitational wave detector,' , 2015, **32**, p. 024001, doi:https://doi.org/10.1088/0264-9381/32/2/024001.

Acernese, F. *et al.*, 'Calibration of Advanced Virgo and Reconstruction of the Gravitational Wave Signal $h(t)$ during the Observing Run O2,' , 2018, **35**(20), p. 205004, doi:https://doi.org/10.1088/1361-6382/aadf1a.

Aghanim, N. *et al.*, 'Planck 2018 results. VI. cosmological parameters,' A&A accepted, 2018, doi:https://doi.org/10.1051/0004-6361/201833910.

Akutsu, T. *et al.*, 'KAGRA: 2.5 generation interferometric gravitational wave detector,' Nat. Astron., 2019, **3**, pp. 35–40, doi:https://doi.org/10.1038/s41550-018-0658-y.

Anders, E., Mendell, G., and Savage, R., 'Spectral line monitoring tool,' LIGO Report, 2013.

Backer, D., Kulkarni, R. S., *et al.*, 'A millisecond pulsar,' Nature, 1982, p. 300.

Barsotti, L. *et al.*, 'The updated advanced ligo design curve,' LIGO Technical Report, 2018.

Bendat, J. S. and Piersol, A. G., *Random Data: Analysis and Measurement Procedures, Fourth Edition*, John Wiley and Sons, 2010.

Bethe, H. A. and Wilson, J. R., 'Revival of a stalled supernova shock by neutrino heating.' Astrophys. J., 1985, **295**.

Bork, R., Hanks, J., Barker, D., *et al.*, 'An overview of the LIGO control and data acquisition system,' SoftwareX submitted, 2020.

Brooks, A. *et al.*, 'Direct measurement of absorption-induced wavefront distortion in high optical power systems,' Applied Optics, 2009, **48**.

Brooks, A. F., Yamamoto, H., Vajente, G., *et al.*, 'Point absorbers in Advanced LIGO,' (in preparation), 2020.

Bustamante, M., Baerwald, P., Murase, K., and Winter, W., 'Neutrino and cosmic-ray emission from multiple internal shocks in gamma-ray bursts,' Nature, 2015, **6**.

Cahillane, C. *et al.*, 'Calibration uncertainty for advanced ligo's first and second observing runs,' Phys. Rev. D, 2017, **96**, p. 102001, doi: https://link.aps.org/doi/10.1103/PhysRevD.96.102001.

Canete, L., 'Implementation of an optical follower servo for the aligo pcal,' LIGO Report, 2013.

Chen, H.-Y., Fishbach, M., and Holz, D. E., 'A two percent Hubble constant measurement from standard sirens within five years,' Nature, 2018, **562**(7728), pp. 545–547, doi:10.1038/s41586-018-0606-0.

Chu, Y., 'Development of kagra photon calibrator for hardware injection test,' 2018.

Clubley, D. A., Newton, G. P., Skeldon, K. D., and Hough, J., 'Calibration of the glasgow 10-m prototype laser interferometric gravitational wave detector using photon pressure,' Phys.Lett.A, 2001, **283**, doi:10.1016/S0375-9601(01)00231-6.

Colgate, S. A. and White, R. H., 'The hydrodynamic behavior of supernovae explosions.' Astrophys. J., 1966, **143**.

Corsi, A. and Owen, B. J., 'Maximum gravitational-wave energy emissible in magnetar flares,' Phys. Rev. D, 2011, **83**.

Couch, S. M., 'The mechanism(s) of core-collapse supernovae,' Phil. Trans. R. Soc. A, 2017, **375**.

D Bhattacharjee, S. K., Y Lecoeuche *et al.*, 'Fiducial displacements with improved accuracy for the global network of gravitational wave detectors,' Class. and Quantum Grav., 2021, **38**(1), p. 015009, doi:10.1088/1361-6382/aba9ed.

D. V. Martynov, B. P. A., E. D. Hall *et al.*, 'The sensitivity of the advanced ligo detectors at the beginning of gravitational wave astronomy,' Phys. Rev. D, 2016, **93**, p. 112004, doi:https://doi.org/10.1088/0264-9381/34/1/015002.

De-Witt, C. M. and Rickles, D., *The role of gravitation in physics : report from the 1957 Chapel Hill Conference*, Berlin : Edition Open Access, 2011.

Drago, M., Gayathri, V., Klimenko, S., *et al.*, 'Coherent waveburst, a pipeline for unmodeled gravitational-wave data analysis,' arXiv:2006.12604, 2020.

Drever, R., Hall, J., *et al.*, 'Laser phase and frequency stabilization using an optical resonator,' Applied Physics B, 1983, p. 97.

Einstein, A., 'Zur elektrodynamik bewegter körper,' Annalen der Physik, 1905.

Einstein, A., 'Collected papers of albert einstein volume 8: The berlin years: Correspondence 1914-1918,' 1914-1918.

Einstein, A., 'The field equations of gravitation,' Proceedings of Prussian Academy of Sciences, 1915, p. 844.

Einstein, A., 'Approximative integration of the field equations of gravitation,' Proceedings of Prussian Academy of Sciences, 1916, p. 688.

Einstein, A., 'On gravitational waves,' Sitzungsberichte der Königlich Preußischen Akademie der Wissenschaften, 1918, pp. 154–167.

Estevez, D., Mours, B., and Pradier, T., 'Newtonian calibrator tests during the virgo o3 data taking,' Class. Quantum Grav., 2021, **38**.

Fairhurst, S., 'Triangulation of gravitational wave sources with a network of detectors,' , 2009, **11**, p. 123006, doi:https://doi.org/10.1088/1367-2630/11/12/123006.

Fairhurst, S., 'Localization of transient gravitational wave sources: beyond triangulation,' Class. Quantum Grav., 2018, **35**.

Forbes, N., *Faraday, Maxwell, and the Electromagnetic Field: How Two Men Revolutionized Physics*, Prometheus Press, 2014.

Gehrels, N., Chincarini, G., Giommi, P., *et al.*, 'The swift gamma-ray burst mission,' Astroph. J., 2004, **611**.

Goetz, E., 'Gravitational wave studies: Detector calibration and an all-sky search for spinning neutron stars in binary systems,' 2010.

Goetz, E., Kalmus, P., Erickson, S., *et al.*, 'Precise calibration of LIGO test mass actuators using photon radiation pressure,' , 2009, **26**, p. 245011, doi: https://doi.org/10.1088/0264-9381/26/24/245011.

Goetz, E. and Savage, R. L., 'Calibration of the ligo displacement actuators via laser frequency modulation,' Class. Quantum Grav., 2010, **27**.

Goetz, E., Savage, R. L., *et al.*, 'Accurate calibration of test mass displacement in ligo interferometers,' Class. Quantum Grav., 2010.

Goldstein, A., Veres, P., Burns, E., *et al.*, 'An ordinary short gamma-ray burst with extraordinary implications: Fermi-gbm detection of grb 170817a,' Astroph. JL, 2017, **848**.

Goodman, J. W., *Speckle Phenomena in Optics: Theory and Applications, First Edition*, Roberts and Company Publishers, 2009.

Griffiths, D. J., *Introduction to electrodynamics, Third Edition*, Prentice Hall, 1999.

Guth, A. H., 'Inflationary universe: A possible solution to the horizon and flatness problems,' Phys. Rev. D, 1981, **23**.

Górski, K. M., Hivon, E., Wandelt, B. D., *et al.*, 'Healpix: Data analysis, simulations and visualization on the sphere,' 2019.

Hild, S., Brikmann, M., Danzmann, K., *et al.*, 'Photon pressure induced test mass deformation in gravitational-wave detectors ,' , 2007, **24**(22), pp. 5681–5688, doi: https://doi.org/10.1088/0264-9381/24/22/025.

Huang, Y., Chen, H., Haster, C.-J., *et al.*, 'Impact of calibration uncertainties on hubble constant measurements from gravitational-wave sources,' To be submitted, In preparation.

Hulse, R. A. and Taylor, J. H., 'Discovery of a pulsar in a binary system.' Astroph. J, 1975, p. 195.

Inoue, Y., Haino, S., Kanda, N., *et al.*, 'Improving the absolute accuracy of the gravitational wave detectors by combining the photon pressure and gravity field calibrators,' Phys. Rev. D, 2018, **98**, p. 022005, doi: https://doi.org/10.1103/PhysRevD.98.022005.

Iyer, B. *et al.*, 'LIGO-India, proposal of the consortium for Indian initiative in gravitational-wave observations,' LIGO Report, 2011.

Janka, H.-T., 'Neutrino emission from supernovae,' arXiv:1702.08713, 2017.

Janka, H. T. and Mueller, E., 'Neutrino heating, convection, and the mechanism of type-ii supernova explosions,' Astron. Astrophys, 1996, **306**, p. 167.

Jeannerot, R., Rocher, J., and Sakellariadou, M., 'How generic is cosmic string formation in susy guts,' Phys. Rev. D, 2003, **68**.

Jones, D. I., 'Gravitational wave emission from rotating superfluid neutron stars,' Monthly Notices of the Royal Astronomical Society, 2010, p. 402.

Karki, S., 'Accurate and precise calibration of Advanced LIGO detectors in the era of gravitational wave astronomy,' PhD diss., 2019, p. University of Oregon.

Karki, S., Tuyenbayev, D., Kandhasamy, S., *et al.*, 'The Advanced LIGO photon calibrators,' RSI, 2016, **87**, p. 114503, doi:https://doi.org/10.1063/1.4967303.

Klimenko, S., Mohanty, S., Rakhmanov, M., and Mitselmakher, G., 'Constraint likelihood analysis for a network of gravitational wave detectors,' Phys. Rev. D, 2005, **72**.

Klimenko, S., Vedovato, G., Drago, M., *et al.*, 'Localization of gravitational wave sources with networks of advanced detectors,' Phys. Rev. D, 2001, p. 83.

Klimenko, S., Vedovato, G., Necula, V., *et al.*, 'cwb pipeline library: 6.4.0,' 2021.

Kuroda, T., Kotake, K., Hayama, K., *et al.*, 'Correlated signatures of gravitational-wave and neutrino emission in three-dimensional general-relativistic core-collapse supernova simulations,' Astroph. J, 2017, **851**.

Kück, S., 'Final report on EUROMET comparison EUROMET.PR-S2 (project no. 156): Responsivity of detectors for radiant power of lasers,' Metrologia, 2010, **47**, p. 02003, doi:https://doi.org/10.1088/0026-1394/47/1A/02003.

Lecoeuche, Y., Szczepańczyk, M., Savage, R., *et al.*, 'Pcal gold standard and working standard configuration change proposal,' LIGO Technical Report, 2019.

Lehman, J., 'Private communication,' 2020.

LIGO Pcal Group, 'Photon calibrator gold standard NIST calibration (10 Dec 2018),' LIGO Technical Report, 2018.

LIGO Pcal Group, 'Photon calibrator end station calibration general directory,' LIGO Technical Report, 2020a.

LIGO Pcal Group, 'Photon calibrator lab measurements general directory,' LIGO Technical Report, 2020b.

Lindblom, L., 'Optimal calibration accuracy for gravitational-wave detectors,' Phys. Rev. D, 2009, **80**, p. 042005, doi:https://doi.org/10.1103/PhysRevD.80.042005.

Luck, H., Affeldt, C., Degallaix, J., *et al.*, 'The upgrade of geo600,' Journal of physics: conference series, 2010, **228**.

M Spidell, H. L., M López *et al.*, 'A bilateral comparison of nist and ptb laser power standards for scale realization confidence by gravitational wave observatories,' Metrologia, 2021.

Maggiore, M., *Gravitational Waves Volume 1*, Oxford University Press, 2008.

Martinovic, K., Meyers, P., Sakellariadou, M., *et al.*, 'Simultaneous estimation of astrophysical and cosmological stochastic gravitational-wave backgrounds with terrestrial detectors,' Phys. Rev. D, 2021, **103**.

Matone, L., 'An overview of advanced ligo interferometry,' LIGO Technical Report, 2012, **LIGO- G1200743**.

Maxwell, J. C., 'A dynamical theory of the electromagnetic field,' Phil. Trans. R. Soc., 1865, **155**, p. 459.

Meegan, C., Lichti, G., Bhat, P. N., *et al.*, 'The fermi gamma-ray burst monitor,' Astroph. J., 2009, **702**.

Mercer, R. A. and Klimenko, S., 'The coherent event display,' LIGO Technical Report, 2008.

Michelson, A. and Morley, E., 'On the relative motion of the earth and the luminiferous ether,' American Journal of Science, 1887, **XXXIV**.

Mueller, E., Janka, H. T., and Wongwathanarat, A., 'Parametrized 3d models of neutrino-driven supernova explosions: Neutrino emission asymmetries and gravitational-wave signals,' Astron. Astrophys, 2012, **537**, p. 459.

Newton, I., 'Philosophiae naturalis principia mathematica,' 1686.

O'Connor, E. and Ott, C. D., 'Black hole formation in failing core-collapse supernovae,' Astrophys. J., 2011, **730**, doi:10.1088/0004-637X/730/2/70.

Pirani, F., 'On the physical significance of the riemann tensor,' Acta Phys.Polon., 1956, **15**.

Pitkin, M., Messenger, C., and Wright, L., 'Gravitational wave detection by interferometry (ground and space).' LIGO Technical Report, 2011, **LIGO-P110004**.

Pitkin, M. *et al.*, 'Astrophysical calibration of gravitational-wave detectors,' Phys. Rev. D, 2016, **93**.

Poincare, H., 'Sur la dynamique de l'electron,' Comptes Rendus de l'Academie des Sciences, 1905.

Radice, D., Perego, A., Zappa, F., *et al.*, 'Gw170817: Joint constraint on the neutron star equation of state from multimessenger observations,' Astroph. J. Lett., 2018, **852:L29**.

Rakhmanov, M., Jr., R. S., Reitze, D., *et al.*, 'Dynamic resonance of light in fabry-perot cavities,' Phys. Rev. A, 2002, **305**.

Regimbau, T. and Pacheco, J. A., 'Gravitational wave background from magnetars.' Astron. Astrophys., 2006, **447**.

Riess, A. G., Macri, L. M., Hoffmann, S. L., *et al.*, 'A 2.4 % determination of the local value of the Hubble constant,' Astroph. J, 2016, **826**, p. 56, doi: https://doi.org/10.3847/0004-637X/826/1/56.

Riles, K., 'Gravitational waves: Sources, detectors and searches,' Progress in Particle Nuclear Physics, 2013, **68**.

Riles, K., 'Recent searches for continuous gravitational waves,' arXiv:1712.05897, 2017.

Ross, M. P., Mistry, T., Datrier, L., *et al.*, 'Initial results from the ligo newtonian calibrator,' arXiv:2107.00141, 2021.

Russell, R., 'Catching the wave,' Sci.Am., 1992.

Sathyaprakash, B. S. and Schutz, B. F., 'Physics, astrophysics and cosmology with gravitational waves.' Living Rev. Rel., 2009.

Savchenko, V., Ferrigno, C., Kuulkers, E., *et al.*, 'Integral detection of the first prompt gamma-ray signal coincident with the gravitational-wave event gw170817,' Astroph. JL, 2017, **848**.

Schutz, B., 'Networks of gravitational wave detectors and three figures of merit,' Class. Quantum Grav., 2011, **28**, p. 12, doi:https://doi.org/10.1088/0264-9381/28/12/125023.

Schutz, B. F. and Sathyaprakash, B. S., 'Self-calibration of networks of gravitational wave detectors,' arXiv 2009.10212, 2020.

Smith, N., 'Techniques for improving the readout sensitivity of gravitational wave antennae,' PhD diss., 2012, p. Massachusetts Institue of Technology.

Soares-Santos, M., Holz, D. E., Annis, J., *et al.*, 'The electromagnetic counterpart of the binary neutron star merger ligo/virgo gw170817. i. dark energy camera discovery of the optical counterpart,' Astroph. J. Lett., 2017, **848**, doi:10.3847/2041-8213/aa9059.

Staley, A., 'Locking the advanced ligo gravitational wave detector: with a focus on the arm length stabilization technique,' 2015.

Stephen Hawking, I. W., *Three Hundred Years of Gravitation*, Cambridge University Press, 1987.

Sun, L., Goetz, E., Kissel, J. S., *et al.*, 'Characterization of systematic error in Advanced LIGO calibration,' Class. Quantum Grav., 2020, **37**.

Sun, L., Goetz, E., Kissel, J. S., *et al.*, 'Characterization of systematic error in Advanced LIGO calibration in the second half of O3,' arXiv, 2021.

Szczepanczyk, M., 'Multimessenger astronomy with gravitational waves from core-collapse supernovae,' 2018.

Szczepanczyk, M., Antelis, J. M., Benjamin, M., *et al.*, 'Detecting and reconstructing gravitational waves from the next galactic core-collapse supernova in the advanced detector era,' arXiv, 2021.

Taylor, B. N. and Kuyatt, C. E., 'Guidelines for evaluating and expressing the uncertainty of NIST measurement results,' NIST Technical Note 1297, 1994.

Taylor, J. H. *et al.*, 'Overall measurements of relativistic effects in binary pulsar psr 1913+16,' Nature, 1979, p. 277.

Tuyenbayev, D., Karki, S., Betzwieser, J., *et al.*, 'Improving LIGO calibration accuracy by tracking and compensating for slow temporal variations,' , 2017, **34**, p. 015002, doi:https://doi.org/10.1103/PhysRevD.93.112004.

Ugliano, M., Janka, H. T., Marek, A., *et al.*, 'Progenitor–explosion connection and remnant birth masses for neutrino-driven supernovae of iron-core progenitors.' Astrophys. J., 2012, **757**, doi:10.1088/0004-637X/757/1/69.

Vaskuri, A., Stephens, M. S., Tomlin, N. A., *et al.*, 'Microfabricated bolometer based on a vertically aligned carbon nanotube absorber,' Proc. SPIE, 2020, **11269**, pp. 41–52, doi:https://doi.org/10.1117/12.2545254.

Vitale, S., Del Pozzo, W., Li, T. G. F., *et al.*, 'Effect of calibration errors on bayesian parameter estimation for gravitational wave signals from inspiral binary systems in the advanced detectors era,' Phys. Rev. D, 2012a, **85**, p. 064034, doi: https://doi.org/10.1103/PhysRevD.85.064034.

Vitale, S., Pozzo, W. D., Li, T. G. F., and Broeck, C. V. D., 'Effect of calibration errors on bayesian parameter estimation for gravitational wave signals from inspiral binary systems in the advanced detectors era,' Phys. Rev. D, 2012b, **85**.

Weber, J., 'Detection and generation of gravitational waves,' Phys. Rev., 1960, **117**.

Weber, J., 'Observation of the thermal fluctuations of a gravitational wave detector,' Phys. Rev. Lett., 1966, **17**.

Weber, J., 'Evidence for discovery of gravitational radiation,' Phys. Rev. Lett., 1969, **22**.

WG-KC, C., 'Guidelines for ccpr key comparison report preparation,' BIPM, 2019.

Zhu, X., Howell, E. J., Blairs, D. G., *et al.*, 'On the gravitational wave background from compact binary coalescences in the band of ground- based interferometers,' Mon. Not. Roy. Astron. Soc., 2013, **431**.

VITA

Dripta Bhattacharjee received a Doctor of Philosophy from Missouri University of Science and Technology in December, 2021. She worked under the supervision of Dr. Marco Cavaglia and Dr. Richard Savage on delivering calibration fiducials with sub-percent accuracy for the latest observation run of the Laser Interferometer Gravitational-wave Observatory (LIGO). The second half of her research involved an investigative study on the impact of overall calibration errors on sky localization of burst-like gravitational wave sources.

She received a Master of Arts in Physics from University of Mississippi in May, 2019 with a GPA of 3.87/5. She worked under the supervision of Dr. Marco Cavaglia on a project to apply Machine Language algorithms to find the origin of glitches in the LIGO data, which often mimic gravitational wave signals but are of non-astrophysical origin. She also worked under the guidance of Dr. Kate Dooley to build an optical lever system to measure the amount of tilt experienced by a suspended seismometer.

She received a Master of Science with Honors in Physics from University of Delhi in May, 2015 with a GPA of 68.3/100. She passed with First-Class distinction. She worked on a project studying the evolution of black holes with time and information paradox.

She received a Bachelor of Science with Honors in Physics from Miranda House College in March, 2013 with a GPA of 81.6/100. She passed with First-Class distinction.